

PASSIVE MITIGATION OF COMBUSTION NOISE AND THERMO-ACOUSTIC
INSTABILITY USING POROUS INERT MEDIA AT ELEVATED PRESSURE

by

L. JUSTIN WILLIAMS

AJAY AGRAWAL, COMMITTEE CHAIR

AMY LANG

WILLARD SCHREIBER JR

ROBERT TAYLOR

A THESIS

Submitted in partial fulfillment of the requirements
for the degree of Master of Science
in the Department of Mechanical Engineering
in the Graduate School of
The University of Alabama

TUSCALOOSA, ALABAMA

2012

Copyright L. Justin Williams 2012
ALL RIGHTS RESERVED

ABSTRACT

Combustion instabilities have presented major problems in high-pressure, turbulent combustion systems for nearly a century, beginning with rocket propulsion systems. To enhance combustion efficiencies, other engines, such as gas turbines for power generation, operate at high pressures and reactant flow rates that are only small relative to those of rocket engine operation. The majority of power generation systems today extract energy from such efficient combustion processes. Recently, gas turbine engines, both power generation and propulsion platforms, are operated under very lean conditions to reduce flame temperatures and thus, emissions of the primary smog forming constituent, NO_x. Extinction, flashback, blowoff, and autoignition pose challenges when operating at lean-premixed conditions. Flame stability at such lean conditions is problematic; thus, a swirled flow method is used to anchor and stabilize these flames. Intense turbulence, resulting from the pressure drop across flow swirlers, drives fluctuations in pressure and heat release rate. The feedback between pressure oscillations and heat release fluctuations in the reaction zone often drives resonant instabilities that propagate through the flow and surrounding structures. Such self-excited instabilities influence high rates of heat release in the reaction zone, which is located near the point of injection. Vibrations and high temperatures lead to the fatigue of injection components, instrumentation, and downstream turbine blades.

A novel passive combustion noise control technique is experimentally investigated in the present study. The approach involves the mating of a porous inert material (PIM) with the inlet of a swirl-stabilized, lean-premixed combustor. The foam insert reduces turbulent intensities within the inner and outer recirculation zones of a common swirl-stabilized

burner, thus reducing the amplitude of combustion driven instabilities. Experiments are conducted at high pressures, with high reactant flow rates and equivalence ratios. Results show that the ceramic foam insert is effective at mitigating combustion instabilities, suppressing combustion noise, and potentially, acoustic damping. The total sound pressure level for many of the cases investigated is reduced by 10 dB and greater. Furthermore, the approach can easily be retrofitted to commercial, industrial, and propulsion gas turbine combustion systems.

DEDICATION

This thesis is dedicated to all my family, particularly to my parents, Larry and Debra, and my sisters, Julie and Lisa. My family has always been supportive and never pushy; for this I thank them.

LIST OF ABBREVIATIONS AND SYMBOLS

| | |
|------------------|----------------------------------|
| 2D | Two-dimensional |
| AF | Air to fuel ratio |
| AF _{st} | Stoichiometric air to fuel ratio |
| B | Bias uncertainty |
| CFD | Computational fluid dynamics |
| CFM | Cubic feet per minute |
| LPM | liters per minute |
| CH ₄ | Methane |
| CNG | Compressed natural gas |
| CO | Carbon monoxide |
| CO ₂ | Carbon dioxide |
| dB | Decibel |
| dba | A-weighted Decibel |
| H ₂ O | Water |
| HfC | Hafnium carbide |
| i.d. | Inside Diameter |
| o.d. | Outside Diameter |
| IRZ | Inner recirculation zone |
| ORZ | Outer recirculation zone |
| LPM | Lean pre-mixed |
| N ₂ | Diatomic nitrogen |

| | |
|--------------------|---|
| NO _x | Nitrous oxides |
| NPT | National pipe thread |
| O ₂ | Diatomic oxygen |
| P | Random uncertainty |
| PIM | Porous inert media |
| ppcm | Pores per centimeter |
| ppi | Pores per inch |
| Q | Air flow rate |
| R | Swirler effective radius |
| R _i | Swirler radius |
| R _c | Swirler center body radius |
| RNG | Renormalization group |
| S | Swirl number |
| SiC | Silicon carbide |
| SPL | Sound pressure level |
| T _{inlet} | Air inlet temperature |
| α | Swirler vane angle |
| ΔP | Pressure differential |
| μ | Total uncertainty |
| μ_f | Viscosity of flowing gas |
| μ_{std} | Viscosity of flowing gas at standard conditions |
| ϕ | Equivalence ratio |
| ρ | Density |

ρ_{std}

Density at standard conditions

ACKNOWLEDGMENTS

It is a wonderful opportunity to display my appreciation to everyone that directly and indirectly contributed to the completion of this thesis.

First, I owe my most sincere appreciation to academic advisor and friend, Dr. Ajay K. Agrawal, whom has guided me throughout my studies, my research, and my professional growth. His patient dedication to progress, unconditional professionalism, and fundamental philosophy have each influenced my overall maturity. The opportunities that he offered were often seemingly demanding but always resulted in valuable experiences, success, and pride. I promise to always strive to represent the type of hardworking, companionate character that composes Dr. Agrawal.

I greatly thank all members of my committee, Dr. Taylor, Dr. Schreiber, and Dr. Lang, each of which are excellent engineers that I am very privileged to have been instructed by.

Next, I owe special gratitude to my peers. I was fortunate to share studies and research with many outstanding classmates and research team members. Daniel, Zach, Joseph, Pankaj, Ben, Troy, Tanisha, Lulin, Yonas, and Dan were always helpful, supportive, and a joy to converse with. I also want to express a particular gratitude to Zach and Joseph, whom I worked most closely with in various stages of my studies. I also owe great thanks to all the staff members in the Mechanical Engineering Department, whose dedication and professionalism have made so many successful academic careers possible at UA. Lynn, Betsy, Lisa, Ken, James, Jim, and Sam; thank you all very much. Furthermore, I thank my good friends Matt, Josh, and Erica for

making my experience in Tuscaloosa remarkable. They were each supportive, encouraging, and a lot of fun.

Lastly, It is needless to say that I will be forever grateful to my parents for all the support and unconditional love that I received during my academic career at UA.

CONTENTS

| | |
|--|------|
| ABSTRACT..... | ii |
| DEDICATION..... | iv |
| LIST OF ABBREVIATIONS AND SYMBOLS..... | v |
| ACKNOWLEDGMENTS..... | viii |
| LIST OF TABLES..... | xiii |
| LIST OF FIGURES..... | xiv |
| CHAPTER 1 INTRODUCTION..... | 1 |
| 1.1 BACKGROUND..... | 1 |
| 1.2 PREVIOUS RESEARCH..... | 5 |
| CHAPTER 2 EXPERIMENTAL APPROACH..... | 16 |
| 2.1 OVERVIEW..... | 16 |
| 2.2 AIR SUPPLY SYSTEM..... | 18 |
| 2.2.1 System Overview..... | 18 |
| 2.2.2 Airline Sonic Nozzle Modification..... | 19 |
| 2.3 FUEL SUPPLY SYSTEM..... | 21 |
| 2.4 EXHAUST SYSTEM..... | 22 |
| 2.5 EXPERIMENTAL APPARATUS..... | 22 |
| 2.5.1 Inlet Pipe Section..... | 23 |
| 2.5.2 Combustion Chamber..... | 23 |
| 2.5.3 Inlet Swirler..... | 24 |
| 2.5.4 Pressure Throttle Valve..... | 26 |
| 2.5.5 Ignition System..... | 27 |

| | |
|---|-----|
| 2.5.6 Optical Access Panel..... | 28 |
| 2.6 INSTRUMENTATION AND DATA ACQUISITION..... | 29 |
| 2.6.1 Flow Measurement..... | 29 |
| 2.6.2 Pressure and Temperature Measurement..... | 30 |
| 2.6.3 Acoustics Measurements | 31 |
| 2.6.4 Data Acquisition System..... | 32 |
| 2.7 OPERATING PROCEDURE | 34 |
| 2.7.1 Preliminary Tasks | 34 |
| 2.7.2 Air Flow..... | 35 |
| 2.7.3 Fuel Flow and Ignition..... | 35 |
| 2.7.4 Pressure Elevation..... | 36 |
| 2.7.5 System Shutdown | 36 |
| | |
| CHAPTER 3 SUPPRESSION OF COMBUSTION DRIVEN THERMO-ACOUSTIC INSTABILITIES USING POROUS INERT MEDIA..... | 61 |
| 3.1 OVERVIEW | 61 |
| 3.2 EXPERIMENTAL SETUP | 63 |
| 3.3 RESULTS AND DISCUSSION..... | 66 |
| 3.3.1 Suppression of Thermo-acoustic Instabilities when using a Steel Combustor | 66 |
| 3.3.2 Suppression of Thermo-acoustic Instabilities when using a Quartz Combustor | 75 |
| 3.4 CONCLUSIONS | 91 |
| | |
| CHAPTER 4 CONCLUSIONS AND RECOMMENDATIONS..... | 118 |
| 4.1 CONCLUSIONS | 118 |
| 4.2 RECOMMENDATIONS | 120 |

| | |
|--|-----|
| REFERENCES | 121 |
| APPENDIX A – DETAILED DRAWINGS OF FACILITY AND EXPERIMENTAL APPARATUS..... | 124 |
| APPENDIX B – CALCULATION OF SWIRL NUMBER..... | 144 |
| APPENDIX C – CALCULATION OF AIR FLOW RATE AND EQUIVALENCE RATIO..... | 146 |
| APPENDIX D – SOUND PRESSURE LEVEL CALCULATION..... | 148 |
| APPENDIX E – UNCERTAINTY ANALYSIS..... | 162 |
| APPENDIX F – PLOTS OF JET NOISE..... | 165 |

LIST OF TABLES

| | |
|--|----|
| Table 1-1 Common Sources of Noise..... | 2 |
| Table 1-2 Simulation Inflow and Equivalence Ratio Conditions and Resulting RMS Pressure and Sound Level | 8 |
| Table 2-1 Instrumentation used for Flow Measurement..... | 30 |
| Table 3-1 Overall Sound Pressure Levels for Steel Combustor Tests with Q = 400 LPM and T = 20 C..... | 67 |
| Table 3-2 Overall Sound Pressure Levels for Steel Combustor Tests with Q = 300 LPM and T = 20 C..... | 72 |
| Table 3-3 Overall Sound Pressure Levels for Quartz Combustor Tests with Q = 400 LPM and T = 20 C..... | 77 |
| Table 3-4 Overall Sound Pressure Levels for Quartz Combustor Tests with Q = 600 LPM and T = 20 C..... | 85 |

LIST OF FIGURES

| | | |
|---------------------|---|----|
| <i>Figure 1.1.</i> | Swirl-stabilized combustion featuring central toroidal and corner recirculation zones | 11 |
| <i>Figure 1.2.</i> | Mean temperature fields and streamlines for two different swirl numbers (Y. Huang & V. Yang, 2005)..... | 12 |
| <i>Figure 1.3.</i> | Time tracks of the normalized fluctuating axial velocity $u'u$ at the channel outlet recorded under forced flow experiments with flames and DPC injection (Noiray, 2009)..... | 13 |
| <i>Figure 1.4.</i> | Photographs of diffusing PIM..... | 14 |
| <i>Figure 1.5.</i> | Combustion noise SPL in one third octave, $Q = 2040$ slpm, $\Phi = 0.65$, $P = 2$ atm (a) $T_{inlet} = 20$ °C, (b) $T_{inlet} = 130$ °C..... | 15 |
| <i>Figure 1.6.</i> | Combustion noise SPL in one third octave, $Q = 2040$ slpm, $\Phi = 0.75$, $P = 2$ atm (a) $T_{inlet} = 20$ °C, (b) $T_{inlet} = 130$ °C | 15 |
| <i>Figure 2.1.</i> | Schematic of fuel/air supplies and instrumentation | 37 |
| <i>Figure 2.2.</i> | Electric air heater (a) Photographic image (b) Schematic diagram | 38 |
| <i>Figure 2.3.</i> | Photographs of sonic nozzles for (a) Combustion air (b) Cooling air | 39 |
| <i>Figure 2.4.</i> | Outdoor fueling station | 40 |
| <i>Figure 2.5.</i> | Schematic of assembled experimental apparatus..... | 41 |
| <i>Figure 2.6.</i> | Exploded view of experimental apparatus | 42 |
| <i>Figure 2.7.</i> | Photograph of experimental apparatus premix section and cooling air hoses | 43 |
| <i>Figure 2.8.</i> | Photograph of experimental setup with high-pressure enclosure/vessel | 44 |
| <i>Figure 2.9.</i> | Photograph of high-pressure vessel/enclosure..... | 45 |
| <i>Figure 2.10.</i> | Combustor and PIM orientation with dump plane..... | 46 |
| <i>Figure 2.11.</i> | Photographic image of swirler | 47 |

| | |
|---|----|
| <i>Figure 2.12.</i> Detailed drawing of swirler..... | 48 |
| <i>Figure 2.13.</i> Exploded drawing of variable swirler mechanism..... | 49 |
| <i>Figure 2.14.</i> Schematic drawing of pressure throttle mechanism mounted to enclosure | 50 |
| <i>Figure 2.15.</i> Photograph of orifice plate and throttle needle..... | 51 |
| <i>Figure 2.16.</i> Photograph of throttle mechanism mounted to reducer via steel plate | 52 |
| <i>Figure 2.17.</i> Photograph of ignition probe | 53 |
| <i>Figure 2.18.</i> Top view of enclosure, pointing out previous window clamp..... | 54 |
| <i>Figure 2.19.</i> Top view of preferred enclosure modifications for new window assembly | 55 |
| <i>Figure 2.20.</i> Rayotek sight glass that threads into a 0.50 inch NPT port on the enclosure | 56 |
| <i>Figure 2.21.</i> Photograph of new window assembly mounting to enclosure..... | 57 |
| <i>Figure 2.22.</i> Layout of NI CompactRIO data acquisition system | 58 |
| <i>Figure 2.23.</i> Schematic layout of flow control system..... | 59 |
| <i>Figure 2.24.</i> LabVIEW flow measurement front panel as displayed on operator PC monitor | 60 |
| <i>Figure 3.1.</i> Experimental apparatus..... | 93 |
| <i>Figure 3.2.</i> Porous insert within a swirl-stabilized combustor | 94 |
| <i>Figure 3.3.</i> Photographs of custom quartz combustor with and without PIM..... | 95 |
| <i>Figure 3.4.</i> Photograph (left) and drawing (right) of porous insert..... | 96 |
| <i>Figure 3.5.</i> Acoustic power spectra and SPL in 1/3 rd octave band for P = 0.405 MPa, Q = 400 LPM, (a) $\phi = 0.55$ (case P4-55), (b) $\phi = 0.65$ (case P4-65), and (c) ϕ = 0.75 (case P4-75) | 97 |
| <i>Figure 3.6.</i> Acoustic power spectra and SPL in 1/3 rd octave band for P = 0.304 MPa, Q = 400 LPM, (a) $\phi = 0.55$ (case P3-55), (b) $\phi = 0.65$ (case P3-65), and (c) $\phi = 0.75$ (case P3-75) | 98 |

| | | |
|---------------------|--|-----|
| <i>Figure 3.7.</i> | Acoustic power spectra and SPL in 1/3 rd octave band for P = 0.203 MPa, Q = 400 LPM, (a) $\phi = 0.55$ (case P2-55), (b) $\phi = 0.65$ (case P2-65), and (c) $\phi = 0.75$ (case P2-75) | 99 |
| <i>Figure 3.8.</i> | Acoustic power spectra and SPL in 1/3 rd octave band for P = 0.101 MPa, Q = 400 LPM, (a) $\phi = 0.55$ (case P1-55), (b) $\phi = 0.65$ (case P1-65), and (c) $\phi = 0.75$ (case P1-75) | 100 |
| <i>Figure 3.9.</i> | Photographs of atmospheric flames for (a) $\phi = 0.65$ and (b) $\phi = 0.75$, both with and without porous insert..... | 101 |
| <i>Figure 3.10.</i> | Plot of total sound pressure levels, gathered during steel combustor experiments, for cases with baseline flow rate, Q = 400 LPM | 102 |
| <i>Figure 3.11.</i> | Acoustic power spectra and SPL in 1/3 rd octave band for P = 0.304 MPa, Q = 300 LPM, (a) $\phi = 0.65$ (case P3-65), and (b) $\phi = 0.75$ (case P3-75) . | 103 |
| <i>Figure 3.12.</i> | Acoustic power spectra and SPL in 1/3 rd octave band for P = 0.101 MPa, Q = 300 LPM, (a) $\phi = 0.65$ (case P1-65), and (b) $\phi = 0.75$ (case P1-75) | 104 |
| <i>Figure 3.13.</i> | Plot of total sound pressure levels, gathered during steel combustor experiments, for cases with flow rate, Q = 300 LPM | 105 |
| <i>Figure 3.14.</i> | Signs of critical surface temperatures when operating with a steel combustor at elevated pressures, this one Q = 300 LPM, P \leq 0.304 MPa (3 atm) and $\phi \leq 0.75$ | 106 |
| <i>Figure 3.15.</i> | Upstream surface of PIM damaged and seized by heat in test case Q = 400 LPM, P = 0.405 MPa (4 atm), and $\phi \leq 0.75$ | 107 |
| <i>Figure 3.16.</i> | PIM damaged and seized by heat in test case Q = 400 LPM, P = 0.405 MPa (4 atm), and $\phi \leq 0.75$ | 108 |
| <i>Figure 3.17.</i> | Acoustic power spectra and SPL in 1/3 rd octave band for P = 0.405 MPa, Q = 400 LPM, (a) $\phi = 0.55$ (case P4-55), (b) $\phi = 0.65$ (case P4-65), and (c) $\phi = 0.75$ (case P4-75) | 109 |
| <i>Figure 3.18.</i> | Acoustic power spectra and SPL in 1/3 rd octave band for P = 0.304 MPa, Q = 400 LPM, (a) $\phi = 0.55$ (case P3-55), (b) $\phi = 0.65$ (case P3-65), and (c) $\phi = 0.75$ (case P3-75) | 110 |
| <i>Figure 3.19.</i> | Acoustic power spectra and SPL in 1/3 rd octave band for P = 0.203 MPa, Q = 400 LPM, (a) $\phi = 0.55$ (case P2-55), (b) $\phi = 0.65$ (case P2-65), and (c) $\phi = 0.75$ (case P2-75) | 111 |

| | |
|--|-----|
| <i>Figure 3.20.</i> Acoustic power spectra and SPL in $1/3^{\text{rd}}$ octave band for $P = 0.101$ MPa, $Q = 400$ LPM, (a) $\phi = 0.55$ (case P1-55), (b) $\phi = 0.65$ (case P1-65), and (c) $\phi = 0.75$ (case P1-75) | 112 |
| <i>Figure 3.21.</i> Plot of total sound pressure levels, gathered during quartz combustor experiments, for cases with baseline flow rate, $Q = 400$ LPM | 113 |
| <i>Figure 3.22.</i> Acoustic power spectra and SPL in $1/3^{\text{rd}}$ octave band for $P = 0.304$ MPa, $Q = 600$ LPM, (a) $\phi = 0.55$ (case P3-55), (b) $\phi = 0.65$ (case P3-65), and (c) $\phi = 0.75$ (case P3-75) | 114 |
| <i>Figure 3.23.</i> Acoustic power spectra and SPL in $1/3^{\text{rd}}$ octave band for $P = 0.203$ MPa, $Q = 600$ LPM, (a) $\phi = 0.55$ (case P2-55), (b) $\phi = 0.65$ (case P2-65), and (c) $\phi = 0.75$ (case P2-75) | 115 |
| <i>Figure 3.24.</i> Plot of total sound pressure levels, gathered during quartz combustor experiments, for cases with baseline flow rate, $Q = 400$ LPM | 116 |
| <i>Figure 3.25.</i> PIM fractured along its full circumference after completing experiments for cases with $Q = 400$ LPM and 600 LPM; $P = 0.203$ MPa (2 atm); and $\phi = 0.55, 0.65$ and 0.75 | 117 |

CHAPTER 1

INTRODUCTION

1.1 Background

The combination of combustion noise and resulting instabilities is one challenge common to industrial power generation systems, commercial aircraft propulsion systems, and various military applications. Noise is as common of an environmental hazard as an occupational one. Aside from age related hearing loss, noise-induced hearing loss is the second most common form of sensorineural hearing deficit. Many employees and pedestrians are unaware of both the noise levels around them and the danger of long-term exposure to seemingly comfortable noise levels. Some common sources of noise and associated noise levels are summarized in Table 1.1 (*M. Rabinowitz, 2000*).

Full-scale gas turbine engines, including commercial aircraft engines, generate overall acoustic power levels, or sound pressure levels (SPL), exceeding 140 dB, and combustion noise makes a substantial contribution. Exposure to levels near 90 dB can gradually damage hair cells; where, exposure to levels near 140 dB can be instantaneously damaging. In fact, as many as 10 million Americans have hearing loss as a result of excessive exposure in the workplace or during recreational activities. The condition was once commonly known as “boilermakers’ disease,” because so many workers who fabricated and maintained steam boilers suffered from hearing loss (*M. Rabinowitz, 2000*).

Much of the high amplitude sound power emitted from gas turbine engines is produced by multiple acoustic instabilities that are likely combustion driven. Gas turbine engine noise emission is not only harmful to operator, personnel, and passenger; but it

aids in the fatigue of engine components. Instabilities intensify the turbulence and heat transfer within high-pressure gas turbine combustion systems. The combination of these highly transient thermal stresses and high mechanical loading produces stresses that lead to the thermal mechanical fatigue (TMF) and failure of downstream turbine components, including those near the point of injection. Possibly, the most important downstream components are the turbine blades. The lives of high-pressure turbine blades are dictated by a combination of cyclic thermal, centrifugal, and gas bending loads, or thermal mechanical fatigue (TMF) – with transient thermal stresses dominating (*M. Naeem et al.*, 1999). For so many obvious reasons, combustion instability has become a popular topic of interest in the science and engineering community.

Table 1-1

Common sources of noise

| <i>Sound</i> | <i>Loudness (dB)</i> |
|---|----------------------|
| Gunshot (peak level) | 140 to 170 |
| Jet takeoff | 140 |
| Rock concert, chain saw | 110 to 120 |
| Diesel locomotive, stereo headphones | 100 |
| Motorcycle, lawnmower | 90 |
| OSHA level for hearing conservation program | 85 * |
| Conversation | 60 |
| Quiet room | 50 |
| Whisper | 30 to 40 |

OSHA = Occupational Safety and Health Administration; dB = decibels

** Measurement expressed as dB(A), a scale weighted toward sounds at higher frequencies. 8-hour time-weighted average.*

Successful efforts to meet highly cumulative emissions regulations, particularly those of nitrogen oxides (NO_x), have complicated the task greatly. The most common method used to achieve low-emission (NO_x) in terrestrial gas turbine engines involves the lean mixing of fuel and oxidizer upstream of combustion to avoid stoichiometric reactions - known as lean-premixed (LPM) combustion (*Wicksall & Agrawal, 2006; Sequera, 2011; Smith, 2011*). By reducing flame temperature, LPM systems have proven to reduce emissions of the smog forming constituent (NO_x) without strictly compromising emissions of carbon monoxide (CO). In such systems, lean blow off (LBO) must be avoided to prevent excessive emissions of (CO) (*Wicksall & Agrawal, 2006*). Under turbulent gas turbine conditions, there is much inherent instability associated with the combustion of practical fuels, such as natural gas and syngas, near the lean limit (*Stone & Menon, 2002; Smith, 2011*). Common instabilities encountered with LPM systems include low frequency flow oscillations, presenting initial challenges with flame blow-off and extinction, and high frequency roar, resulting from the resonant coupling of heat driven pressure fluctuations with the natural acoustic modes of the surroundings (*Choi et al., 2005; Wishall & Agrawal, 2006; Stone & Menon, 2002*).

Later in the 19th century, Lord Barron Rayleigh formulated a relationship that perhaps explains the basics regarding thermo-acoustic interactions, with what is known as Rayleigh's criterion. Lord Rayleigh suggested that combustion instabilities occur when heat-release perturbations q' of a reacting mixture adds energy to the acoustic field faster than it can be dissipated (i.e. via viscous dissipation and heat transfer), and he expressed this relationship mathematically with the Rayleigh integral (*Sequera, 2011; Rayleigh, 1945*), given as:

$$\int_V \int_T p'(x, t) q'(x, t) dt dV \geq \int_V \int_T \sum_i L_i(x, t) dt dV \quad (1.1)$$

Where:

$p'(x, t)$ = combustor pressure oscillations

$q'(x, t)$ = heat addition oscillations

V = combustor volume

T = period of oscillation

L_i = i th acoustic energy loss process

Although Rayleigh formulated the relationship between acoustic pressure p' and heat-release q' , he did not generate solutions for the hundreds of combustor designs and various fuels that have risen over the 20th century, and due to the complex nature of turbulent flow and chemical kinetics, neither has anyone else. Nevertheless, a variety of experimental and numerical studies have recently been conducted in an attempt to gain a more complete understanding of combustion driven thermo-acoustics (*Choi et al.*, 2005; *Duchaine et al.*, 2009; *Flemming et al.*, 2005; *Hirsch et al.*, 2007; *Rajaram et al.*, 2006; *Richards et al.*, 2003; *Schwarz & Janicka*, 2009; *Tiribuzi*, 2008).

1.2 Previous Research

Considerable effort has been extended to control the resulting instabilities of combustion noise, either actively or passively. Active control systems are highly dependent on the synchronous operation of sensors, actuators, and control schemes. Advances have been made using active techniques, yet reliability is still a major concern. Perhaps, active control methods are more useful for driving instabilities during a system response investigation. For example, *Johnson et al. (2000)* used active drivers - both fuel and exhaust actuators - to generate desired oscillations within a swirl injection combustor as a technique for determining the stability margin. The active control of combustion dynamics shows promise of expanding the window of stable operating conditions, that is often narrowed by passive control techniques; however, there is substantial progress to be made before such dynamic controls meet commercial standards (*Sequera & Agrawal, 2011*).

Passive control methods have the advantages of being both independent of an external energy source, resulting in fewer problems when compared to active methods; they are also easier to implement. Passive methods are generally divided into two classes. In the first class, acoustic modes of a combustion chamber are altered in such a way that acoustic energy is dissipated (i.e. damping)(*Smith, 2011*). The second class of techniques is directed toward reducing the efficiency of driving processes by altering flame dynamics (i.e. by changing injector geometry)(*Noiray et al., 2009*).

Swirl stabilized combustion is one passive technique commonly used in LPM combustion systems to achieve flame stability (*Stone & Menon, 2002; Sequera, 2011; Huang & Yang, 2005*). One flame stabilizing mechanism associated with swirl injection

involves the formation of a central toroidal recirculation zone (CTRZ), resulting from vortex breakdown. Recirculation zones and flow paths of a typical swirl-stabilized LPM combustor are illustrated in Figure 1.1. The large-scale motion in the CTRZ may be used to alter the coupling of resonant acoustic waves in a combustor. Also, flow swirl in the vortex core may modify the flame structure and combustion intensity, thus influencing the heat release behavior within a combustion chamber (*Huang & Yang, 2005*).

Swirl-stabilized combustion is most practically used for anchoring the flame in a LPM combustor, preventing flashback, lean blowoff, extinction, autoignition, etc. The dynamics of partially premixed swirl flames near LBO have been studied using such technology as chemiluminescence imaging, simultaneous stereo-PIV and OH-PLIF measurements, simultaneous measurements of CH/OH, and large-eddy simulations (LES). Such studies have observed recirculation zones to stabilize a flame in well-defined regions by trapping and recirculating hot product gases. In summary, the modification of mixture fraction in the vortex core region has the potential to enhance stability and shift the LBO to leaner limits (*Smith, 2011; Stöhr et al., 2011*).

A variety of swirler designs have been considered; however, the most popular design is a standard annular one. All swirler configurations may be related using the swirl-number - defined as the ratio of the axial flux of the tangential momentum to the product of the axial momentum flux and a characteristic radius. The swirl-number, S , may also be represented mathematically as (*Stone & Menon, 2002*),

$$S = \frac{\int_0^{D_i/2} \rho u_x u_\theta r^2 dr}{D_i/2 \int_0^{D_i/2} \rho u_x^2 r dr} \quad (1.2)$$

Where u_x and u_θ are the axial and azimuthal velocities, respectively,

ρ is the gas density,

r is the radial location,

and D_i is the injector diameter

Quantitative investigations, such as that of *Huang & Yang* (2005), have determined the dynamic effects of swirl-number on swirl-stabilized combustion. *Huang & Yang* used an LES technique and a level-set flamelet approach. Figure 1.2 exemplifies the flow and temperature distribution within a reacting swirl-stabilized, lean-premixed annular combustor. Two extreme swirl-numbers are visually compared for the following flow properties: an equivalence ratio of 0.573, a chamber pressure of 0.463 MPa (~4.5 atm), inlet temperature of 660 K (~200 °F), and natural gas and air mass flow rates of 1.17 g/s and 50.70 g/s. When increasing the inlet swirl-number, the CTRZ moves upstream and overrides the CRZ, and a higher swirl-number tends to increase the turbulent intensity and flame speed, shortening the flame length. The inlet swirl-number has been observed to employ minute influence on the frequencies of the acoustic oscillations; however, it fulfills a dominant role in determining the amplitude of wave motions (*Huang & Yang*, 2005).

Few in the academic community have experimentally investigated the swirl effects at elevated pressure. *Cabot et al.* (2004) discovered from high-pressure experiments of swirl-stabilized, lean-premixed combustion of methane fuel that the

increased pressure also leads to a reduction in flame length. *Huang and Yang (2005)* concluded that of seven main frequencies indicated by the power spectrum, only the four lower frequencies (32, 133, 350, and 530 Hz) existed in the CH emissions spectrum and were coupled with combustion phenomenon. *Stone & Menon (2002)* also conducted a detailed numerical study on the swirl control of combustion instabilities in a lean-premixed gas turbine combustor using large-eddy simulations methodology. Summarized in Table 1-2 are simulation results covering a variety of swirl-numbers and fuel equivalence ratios (ϕ) (*Stone & Menon, 2002*). Each SPL featured in Table 1-2 represents the change in SPL relative to the base line case (Case 1) (i.e. -5.5 dB indicates a 5.5 dB reduction in noise and 5.5, an extension of 5.5). The numerical work of *Stone & Menon* agrees with that of *Huang & Yang*. The coherence and strength of large-scale coherent vortices driven axial pulsations are decreased with increasing swirl (*Stone & Menon, 2002; Huang & Yang, 2005*).

Table 1-2

Simulation inflow and equivalence ratio conditions and resulting RMS pressure and sound pressure level (relative to Case 1)

| Case | Inlet swirl (S_i) | Equiv. ratio (Φ) | S_L (cm/s) | T_P (K) | p' (% \bar{P}) | SPL (dB) |
|------|--------------------------|----------------------------|-----------------|--------------|------------------------|-------------|
| 1 | 0.56 | 0.52 | 28 | 1811 | 1.95 | — |
| 2 | 0.84 | 0.52 | 28 | 1811 | 1.06 | -5.5 |
| 3 | 1.12 | 0.52 | 28 | 1811 | 0.96 | -6.6 |
| 4 | 0.56 | 0.72 | 52 | 2137 | 1.09 | -5.1 |
| 5 | 0.56 | 1.00 | 85 | 2485 | 1.00 | -6.0 |

To determine the acoustic effects and dominant noise generating factors associated with secondary fuel injection into swirl-stabilized, LPM combustion, *Choi et al.* (2005) investigated the relationship between pressure fluctuations and local flame structure using simultaneous measurements of CH/OH planar laser induced fluorescence (PLIF) and pressure fluctuations. The “beating” of pressure fluctuations may possibly be controlled by secondary fuel injection, and this control is also effective at suppressing low-frequency flow related combustion oscillations, preventing lean blow-off and reducing the emission index. However, secondary premixed injection is not effective for such control (*Choi et al.*, 2005).

The studies of *Noiray et al.* (2009) introduced an interesting passive strategy for controlling thermo-acoustic combustion instabilities that involves the use of a dynamic phase converter (DPC). Theoretically, a DPC system imposes an out-of-phase motion of individually unstable flames that yields opposing heat release fluctuations; which in turn, yields a steady global response to incoming perturbations. The general idea is that when acoustic disturbances try to propagate through the injection diaphragms, the flamelets will absorb the energy and adjust in length, and in a scenario with two flamelets, as one of the flames is stretched the other is contracted (*Noiray et al.*, 2009).

A DPC system has been tested experimentally by driving upstream instabilities with a loudspeaker at both 500 and 650 Hz. Figure 1.3 shows a time trace of the normalized fluctuating axial velocity at the channel outlet, measured by means of Laser Doppler Velocimetry (LDV). In each couple of traces shown in Figure 1.3, the gray triangles and black circles tracks respectively correspond to axial flow velocity at type 1

and type 2 injection channels outlet. It is apparent that when dynamic compensation was provided by the DPC system, flame motions were out of phase. Noiray et al. assimilated a burner, in a first approximation, to a quarter wave resonator with theoretical eigenfrequencies $f_k = (2k + 1)c/4L$. A DPC system may effectively reduce the amplitude of oscillations over a broad range of frequencies, resulting in SPL reductions of 10 – 20 dB; however, undesirable high frequency instabilities may result (Noiray et al., 2009). Furthermore, a DPC could be used to practically suppress azimuthal thermo-acoustic couplings like those observed in gas turbine applications.

The present study investigates a novel technique for mitigating thermal-acoustic instabilities common to gas turbine combustion systems. The process involves coupling porous ceramic foam in an annular fashion with a swirl combustor dump plane, coaxial and diverging with flow. The method encircles both classes of passive control – altering both natural acoustic modes as well as flame dynamics. The practical use of porous inert media (PIM) to suppress combustion instability and the resulting noise in a swirl-stabilized, lean-premixed, methane fueled scale gas turbine combustor has been investigated for operating pressures up to 2 atm (Sequera, 2011). PIM configurations have been parametrically studied by axially adding porous rings of various inside diameters (ID) until an optimum combination was discovered. Of four configurations, including downstream converging and diverging, a flow diverging configuration is found to be the most beneficial for broadband control (Sequera, 2011; Smith, 2011). A custom designed 26 ppcm diverging ceramic foam is featured in Figure 1.4. Sequera (2011) compared sound power spectra using a dynamic pressure transducer to measure internal pressure fluctuations and a condenser microphone to measure acoustic intensities emitted

from a pressurized rig. In such studies, flow properties are selected such that instability is consistently present; thus, thermo-acoustic effects of PIM have been explored for a variety of flow rates, inlet temperatures, and mixture ratios. Figures 1.5 and Figure 1.6 show comparisons of acoustic power levels with and without PIM present, for critical flow conditions (Sequera, 2011).

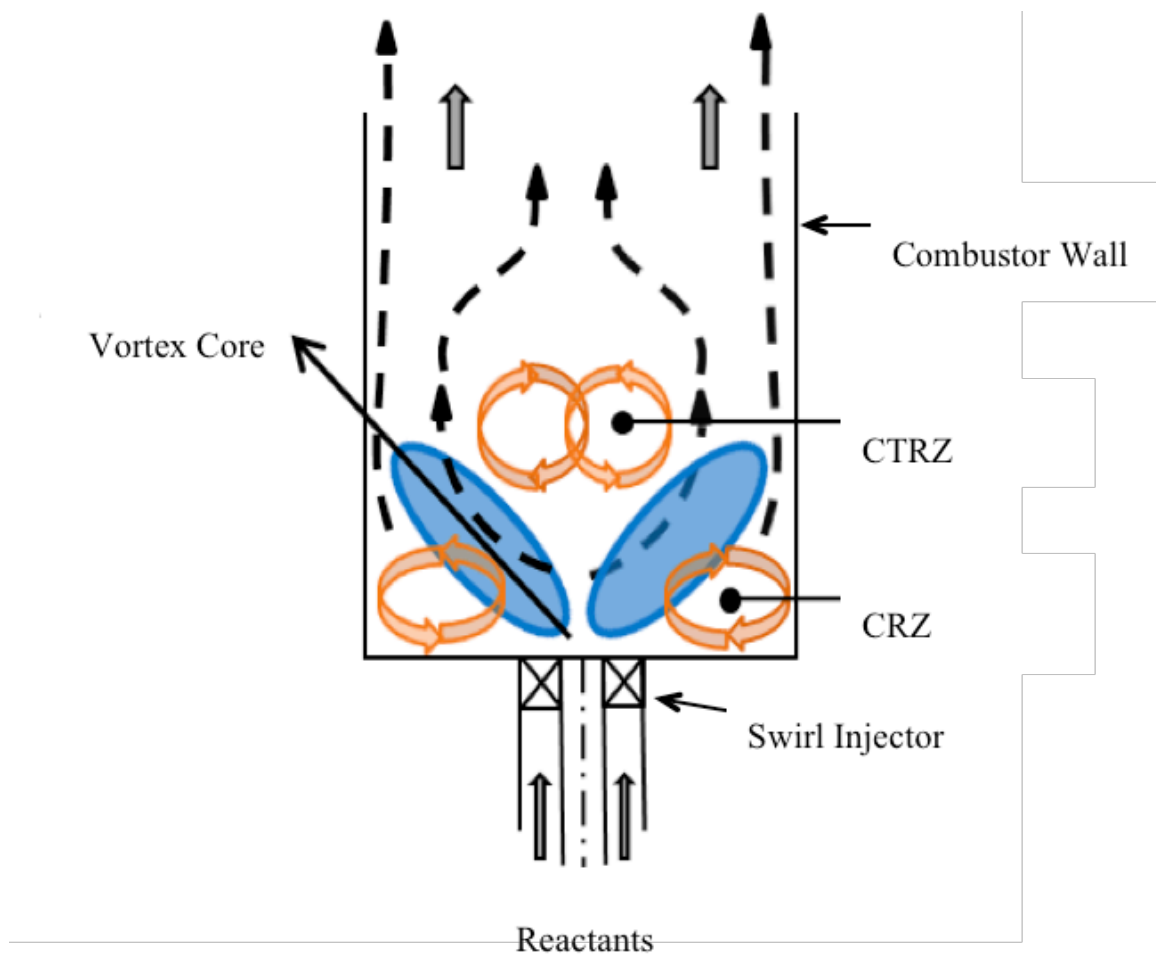


Figure 1.1. Swirl-stabilized combustion featuring central toroidal and corner recirculation zones

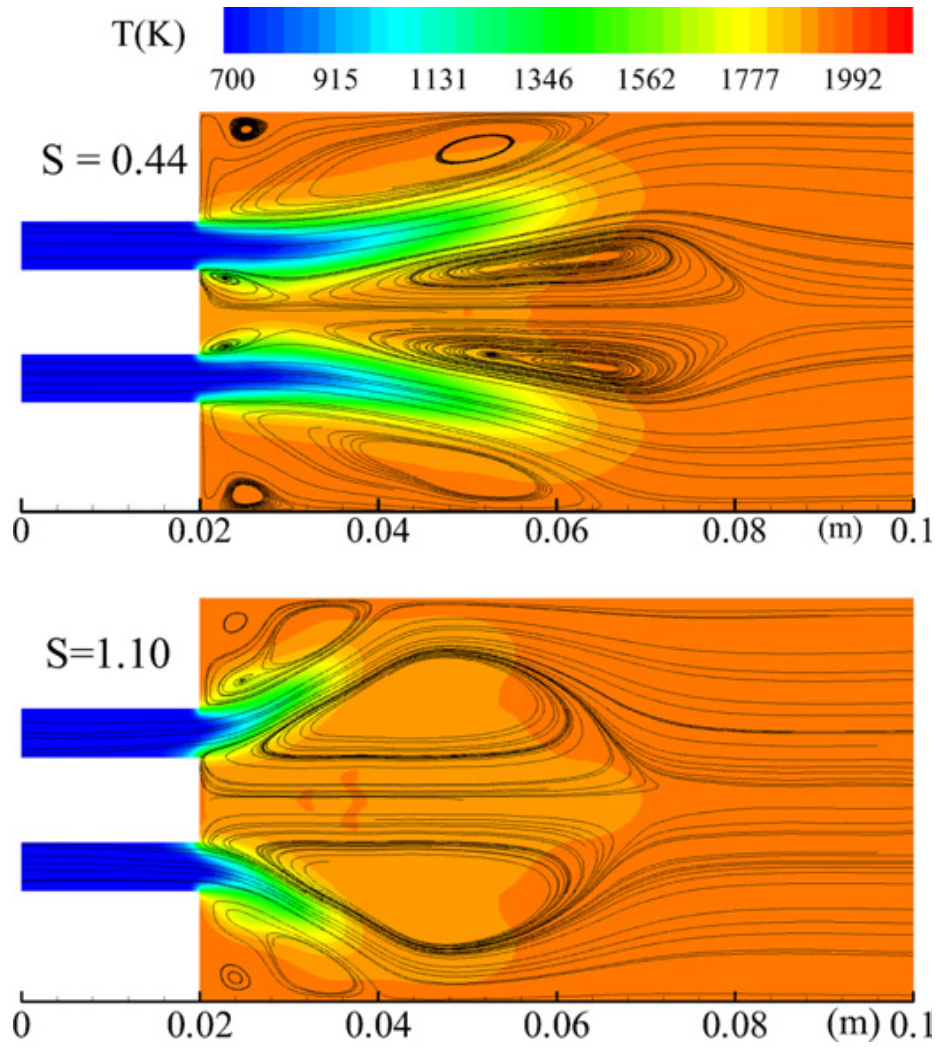


Figure 1.2. Mean temperature fields and streamlines for two different swirl numbers (Y.

Huang & V. Yang, 2005)

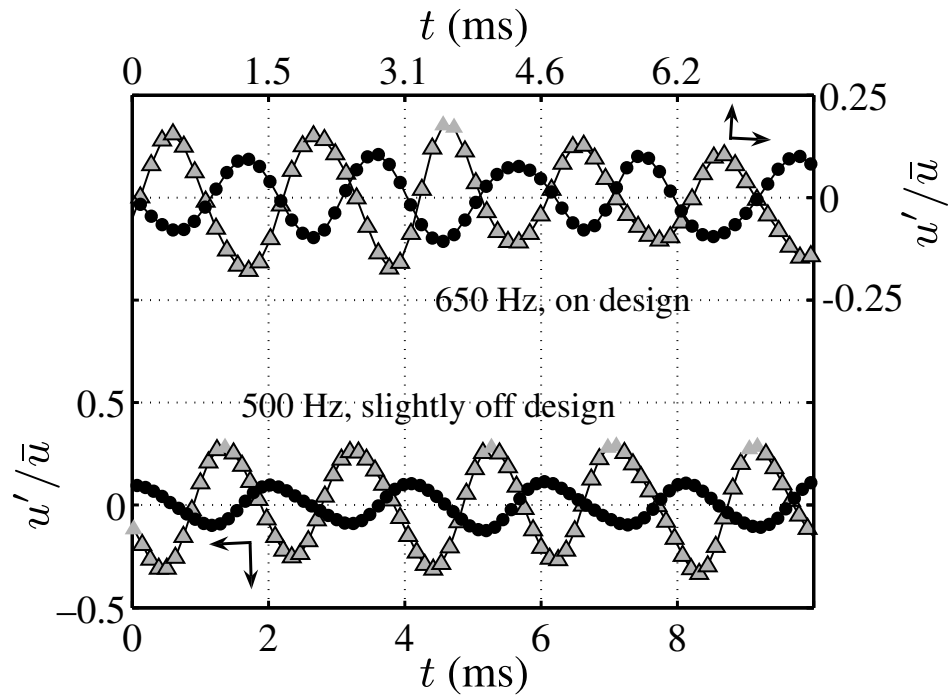


Figure 1.3. Time tracks of the normalized fluctuating axial velocity u'/\bar{u} at the channel outlet recorded under forced flow experiments with flames and DPC injection (Noiray, 2009)

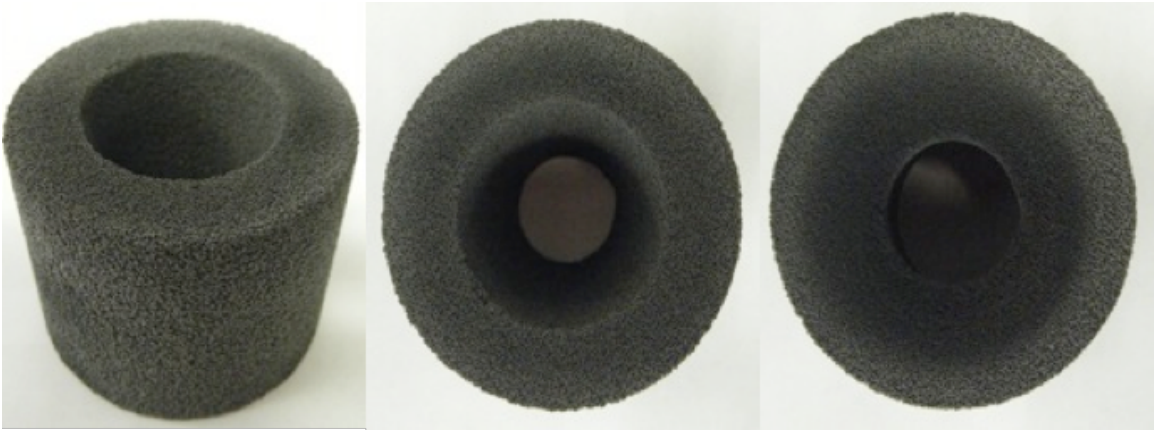


Figure 1.4. Photographs of diffusing PIM

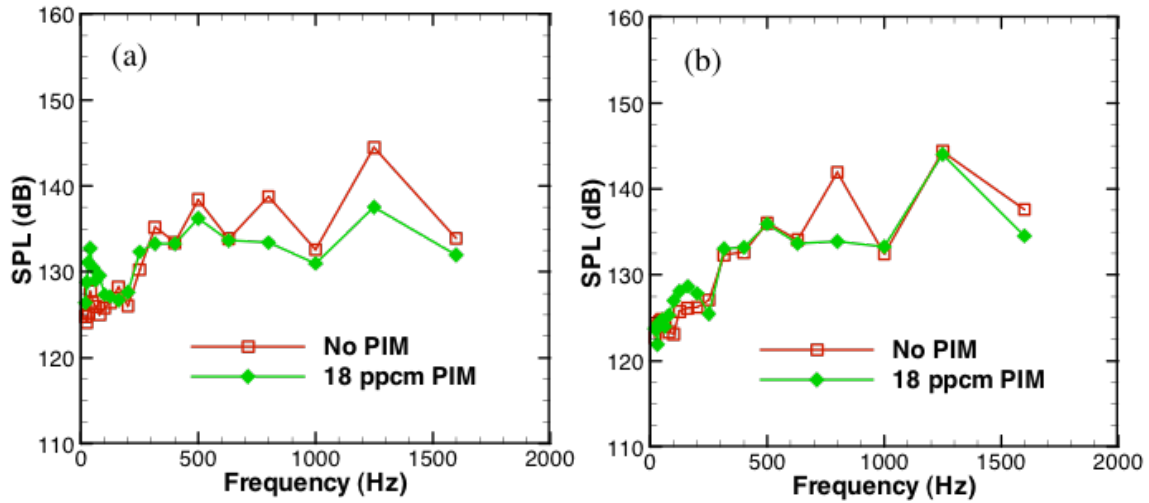


Figure 1.5. Combustion noise SPL in one third octave, $Q = 2040$ slpm, $\Phi = 0.65$,
 $P = 2$ atm (a) $T_{inlet} = 20$ °C, (b) $T_{inlet} = 130$ °C

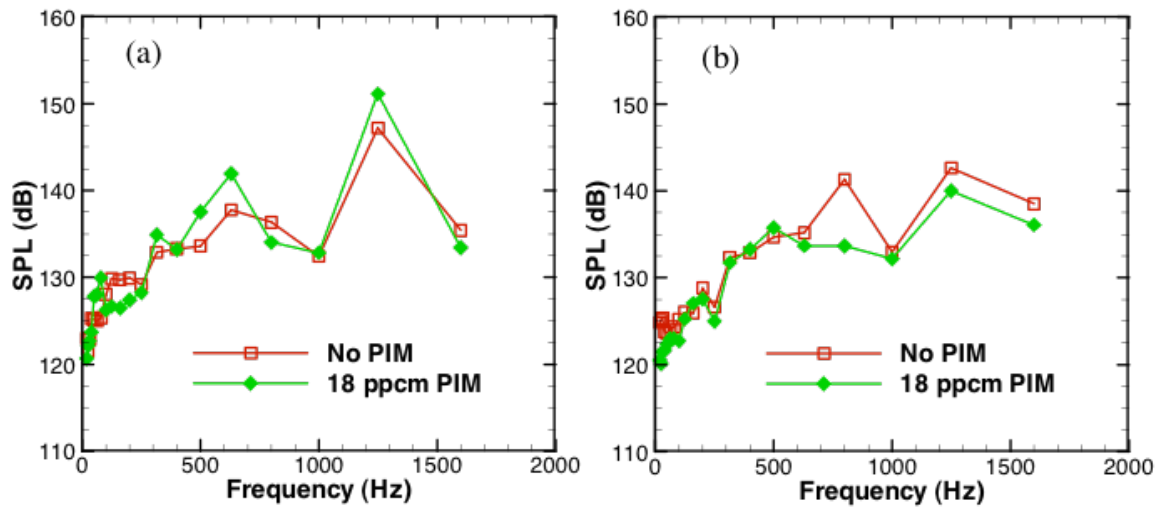


Figure 1.6. Combustion noise SPL in one third octave, $Q = 2040$ slpm, $\Phi = 0.75$, $P = 2$
atm (a) $T_{inlet} = 20$ °C, (b) $T_{inlet} = 130$ °C

CHAPTER 2

EXPERIMENTAL APPROACH

2.1 Overview

The recent drive to develop clean sustainable energy resources has taken research into several distant paths: solar, wind, biomass, etc. Meanwhile, government regulations continue to demand that combustion powered generation processes become cleaner, more efficient, fuel flexible, and even, acoustically softer. For this reason, combustion research has recently gained considerable attention from the scientific community. Engineers have been motivated to produce relatively clean, efficient, commercial scale combustion systems.

Gas turbines for large-scale power generation and aircraft propulsion react heated mixtures at very high flow rates and under tremendous pressure. Current experimental work is generally conducted in simplified environments. In such simplified experiments, reactant mixtures are typically delivered at relatively low flow, room temperature, and atmospheric pressure. Simplified studies have greatly contributed to the further understanding of fundamental concepts that are associated with combustion processes; however, a high-pressure combustion test environment is necessary to further investigate and renovate gas turbine combustion processes.

The University of Alabama demonstrates leadership in the current field of experimental combustion research, by integrating cutting edge techniques, equipment, and facilities. In recent years, UA combustion research laboratories have developed and tested, with innovation and ingenuity, highly efficient low-emission combustion systems;

however, the laboratories have previously only been able to facilitate such experiments at room temperature and atmospheric pressure. In 2009, UA began the development of a combustion laboratory that can facilitate a high-pressure combustion apparatus. The current state of the facility integrates air and fuel supply systems with an experimental test chamber that is capable of withstanding simulated gas turbine temperatures and pressures. The facility consists of three major components: supply and exhaust systems, instruments and data acquisition, and an experimental combustion apparatus. Also, the laboratory is equipped with both an inline electric heater, capable of heating combustion air flow up to 760 °C, and a twin screw air compressor that is capable of delivering air at approximately 5 kg/min. The facility allows experiments to be performed at pressures ranging from 1 to 5 atm. However, in order for combustion instability measurements to be practically gathered for a variety of operating pressures, further development of the apparatus is necessary.

The experimental apparatus needs to be equipped with a remotely operated device that modulates the operating pressure. A proper dynamic pressure sensor and related data acquisition hardware need to be installed. Sonic nozzles should be designed and installed in the airlines, such to separate flow instrumentation from downstream disturbances. With the proper modifications listed above, the test facility will offer the ability to easily conduct a variety of high-pressure combustion experiments, while simultaneously collecting combustion noise measurements.

2.2 Air Supply System

2.2.1 System Overview

Compressed air serves both fuel oxidation and vessel cooling purposes within the high-pressure combustion laboratory. Compressed air is piped directly from a designated compressor into the laboratory space. Once entering the laboratory, air is directed through a pressure regulator. The pressure regulator used to adjust and regulate total air mass flow. Air exiting the pressure regulator is directed upwards along a building column and passed overhead to the combustor space through 5.1 cm [2 in] carbon steel pipe. The air supply is then split into both combustion and cooling air supplies. A general layout of the laboratory piping system is shown schematically in Figure 2.1.

Each airline branch, combustion and cooling, is equipped with a Nibco Class 150 manual globe valve and a laminar flow element (LFE). Operational details of an LFE are further outlined in the flow measurement section. Combustion air is directed through an electric air heater prior to delivery into the combustion chamber. Air is transported from the heater exit to the combustor dump plane via one-inch nominal schedule 80 stainless steel piping, where inline a sonic nozzle was placed. Similarly, through a sonic nozzle, cooling air enters a 4-way manifold where it is distributed to the combustion chamber via four flexible hoses.

An Osram Sylvania 72 kilowatt, 480 volt, flanged in-line heater, as shown in Figure 2.2, preheats combustion airflow to simulate operational gas turbine conditions within the combustion chamber. The heater is capable of heating air to a temperature of 760 °C [1400 °F] and operating over a pressure range of 0 to 1.03 MPa [0 – 150 psi]. Four Type K thermocouples mounted inside the heater couple with an E5CN digital

controller to provide temperature control. An Avatar A3P power controller supplies electrical power, and for safe operation, the control station is mounted away from the combustion chamber. The heater is equipped with a 15.2 cm [6 in] flange on both the entrance and exit port. A 5.1 cm x 15.2 cm [2 in x 6 in] stainless steel diffuser connects upstream piping to the heater entrance, and a 15.2 cm x 2.5 cm [6 in x 1 in] stainless steel reducer connects the heater exit to the downstream piping. A rigid stand that is anchored to the laboratory floor orients the heater vertically. A gasket is installed between the stand and the heater to reduce any vibrations that may arise. Downstream of the heater, heat loss is minimized by wrapping the piping with 7.6 cm [3 in] thick high temperature insulation, and air temperature is measured again just upstream of the dump plane to account for the heat loss.

2.2.2 Airline Sonic Nozzle Modification

Fixed inline sonic nozzles were considered as a solution to prevent airline upstream noise propagation. The sonic nozzles act as a rigid barrier to upstream propagating acoustic perturbations. Both the combustion and cooling airlines were equipped with sonic nozzles, and each nozzle was installed downstream of flow measurement devices. Locations were chosen as close to the experimental apparatus as safely possible. To prevent upstream reactant mixture recirculation, thus nozzle flame attachment, the combustion airline sonic nozzle was located 15 cm upstream of the fuel inlet.

Before either nozzle was sized, several parameters were considered. First, the compressor is capable of constantly delivering a mass flow rate of 5 kg/min, and it charges a large air storage vessel to 1.38 MPa [200 psi]. After line losses, an

approximate 1.03 MPa [150 psi] supply pressure is achievable; and with variable flow choking downstream of the combustor, this supply pressure dictates the maximum achievable chamber pressure. The maximum achievable chamber pressure was determined using the critical pressure ratio for a given operating gas; in this case, air.

The critical pressure ratio is mathematically represented as (J. John, 1969)

$$\frac{P_r}{P_b} = \left(1 + \frac{\gamma - 1}{2}\right)^{\gamma/(\gamma-1)} \quad (2.1)$$

where

P_r is the reservoir, or supply, pressure,

P_b is the back, or chamber, pressure,

and γ is the ratio of specific heats for a given gas

In this case, with $\gamma = 1.4$, a chamber pressure of 0.507 MPa [~ 5 atm] corresponds to the maximum attainable supply pressure of 1.03 MPa [~ 10 atm]. Next, five chamber pressures (1, 2, 3, 4, & 5 atm) are desired for high-pressure experimentation. Based on a range of volumetric flow rates and the five desired chamber pressures, a range of mass flow rates was calculated. With compressor limitations, a fixed sonic nozzle will not enable the full range of mass flow rates required to repeat a large range of volumetric flow rates for each desired chamber pressure; therefore, sacrifices were made.

Consequentially, the combustion airline sonic nozzle throat size is selected to deliver a maximum mass flow rate of 2 kg/min when the maximum pressure of 1.03 MPa is supplied, and with this supply pressure, the chamber pressure may be elevated approximately to a maximum of 0.507 MPa. Ultimately, the peak mass flow limitation

allows the attainment of lower volumetric flow rates for chamber pressure within the lower half of the desired range.

The cooling airline sonic nozzle was sized similarly. A maximum mass flow rate of 1 kg/min – consistent with maximum supply pressure – was chosen as the sizing criteria. So, with desired combustion and cooling air mass flow rates of 2 kg/min and 1kg/min, respectively, the air supply system is capable of delivering air to the experimental apparatus at a total rate of 3 kg/min; thus, when operating at full capacity, the charged air supply tank pressure is maintained at approximately 1.38 MPa [200 psi].

Nozzle sizes were calculated based on the previously mentioned mass flow criteria and compared with readily available sizes. Flow Systems Inc. provides various nozzles for such applications – many, custom. As displayed in Figure 2.3, a standard 4.50 mm [0.177 in] sonic nozzle was selected for the combustion airline and a standard 3.18 mm [0.125 in] sonic nozzle, for the cooling airline.

2.3 Fuel Supply System

An outdoor fuel station, as shown in Figure 2.4, is used to store large amounts of compressed natural gas, which is used for both the low and high pressure combustion experiments. Natural gas is obtained from city supply lines, compressed to a pressure of 20.7 MPa [3,000 psi], and stored in a rack of ten 50-liter tanks enclosed by a safety fence. Compressed natural gas is piped to the interior of the building where the pressure is controlled with a Mecor Type P-1-D pressure regulator. Leaving the regulator, the fuel line is split to supply both the low pressure and high-pressure combustors. A manually operated Swagelok ball valve, installed in each line, provides the option of quick fuel shutoff. As an added safety measure, the high-pressure fuel line is equipped with a

solenoid valve activated by an electrical cutoff switch. The 1.3 cm [0.5 in] high pressure line is routed overhead, alongside the airline, to the high-pressure combustor. A Bronkhorst model F-203AV-M50 mass flow controller, which is capable of delivering flow up to 465 normal liters per minute (NLPM), measures and controls fuel flow. The controller is wired to the NI CompactRIO data acquisition and control system via RS-232 serial connections. A flexible metal hose delivers fuel from the solenoid valve and injects it into the combustion air at a location 61 cm [2 ft] upstream of the dump plane. Fuel is injected against flow to ensure adequate fuel/air mixing prior to the combustion zone.

2.4 Exhaust System

A 30.5 cm [12 in] stainless steel pipe guides hot combustion products to the exterior of the building. The exhaust system serves both the low pressure and high-pressure combustion chambers. The duct is supported with steel rods fastened to horizontal beams above the combustion laboratory. A rooftop fan drives flow in the exhaust duct.

2.5 Experimental Apparatus

The experimental apparatus, seen in Figure 2.5, is composed of preheated combustion air and fuel supplies, a premixing region, a pressure vessel in which combustion takes place, and an exit throttle valve to control operating pressure. Figure 2.6 shows an exploded view of the high-pressure combustion apparatus.

2.5.1 Inlet Pipe Section

The inlet pipe section of the combustor, shown in Figure 2.7, allows air/fuel mixing and delivers the mixture to the combustor. Combustion air enters via sonic nozzle, and gaseous fuel is injected inches downstream at a relatively high pressure. The reactant mixture crosses the length of the inlet pipe before reaching a flow swirler fixed near the exit of the pipe. The exit of the inlet pipe is welded to a 7.6 cm [3 in] stainless steel flange, which serves as the dump plane for the combustion chamber. A spiral wound gasket and a bolted connection respectively seals and secures the flange to the combustion chamber. The inlet pipe flange also serves as a platform for mounting hardware such as the flame enclosure and porous media. Temperature and absolute pressure measurements are taken along the inlet pipe section to closely monitor air/fuel mixture conditions upstream of the combustion zone. A burst disk, rated at 1,034 kPa [150 psi], is placed in the inlet pipe section; thus, if system pressure reaches 1,034 kPa, the disk will burst and relieve the system pressure.

2.5.2 Combustion Chamber

The combustion chamber is enclosed by a stainless steel pressure vessel, which is sealed and bolted to a stainless steel plate hereon referred to as the plenum base. The pressure vessel is a custom cast cylinder with 22.9 cm [9 in] inner diameter (ID) and 38.1 cm [15 in] outer diameter (OD). The vessel is outfitted with twelve 1.3 cm [1/2 in] national pipe thread (NPT) access ports for instrumentation, ignition, and sampling probes access. Photographic images of the pressure vessel are provided in Figures 2.8 and 2.9. Two window ports are machined into opposing sides of the pressure vessel for optical access. Quartz blocks or steel blocks are clamped in place using a stainless steel

rectangular window frame. In preliminary experiments, the window clamping method showed to be problematic with quartz blocks; multiple blocks cracked with only cold flow. In section 2.5.6, a redesign of the optical access panel is discussed in detail. A concentric reducer is mounted on the downstream side of the vessel and connects a pressure throttle valve. The dump plane (as seen in Figure 2.6) is located inside the vessel and mounted horizontally at a location flush with bottom of the windows, providing optical access to the flame region. Either a quartz glass or steel cylinder is placed on top of the dump plane to serve as the combustion chamber. Each combustion chamber, 29 cm [11.5 in] long by 7 cm [2.75 in] i.d., mounts directly to the dump plane, as seen in Figure 2.10. The PIM insert is supported by each combustion chamber. Each chamber has a slightly larger bore on the upstream end where PIM inserts; this creates an edge at the downstream end of the insert, which axially secures the insert. High-pressure rubber hoses deliver cooling air into the bottom of the vessel. The cooling air inlet locations are chosen to provide maximum cooling to the dump plane. In summary, the combustion vessel is designed to safely provide a high-pressure gas turbine combustion environment that is equipped with precision instrumentation and optical access.

2.5.3 Inlet Swirler

An annular inlet swirler, capable of being traversed upstream of the dump plane, is often flush mounted with the dump plane to induce an optimum radial swirling motion to the incoming fuel and air mixture. The swirler vane angle used for this study is 28° from horizontal. A photographic image of the flow swirler is provided in Figure 2.11. Also, a detailed sketch of the swirler is illustrated in Figure 2.12. To allow variability, a mechanism is developed to passively traverse the swirler in the axial direction within the

inlet pipe. The mechanism is designed to allow the swirler to be mounted flush with the dump plane or recessed up to 3.8 cm [1.5 in] inside the inlet pipe.

Illustrated in Figure 2.13, the swirler apparatus consists of six components: a supporting cylinder with threaded extension, three modular slip-on spacers, a threaded swirler, and an endcap. The swirler assembly is supported within the inlet pipe by a set screw that passes through the inlet pipe and base cylinder. The upstream end of the supporting cylinder is milled into a sharp wedge to reduce flow disturbance in the mixing pipe. The spacers and swirler are stacked and secured to a 0.64 cm [1/4 in] threaded stud that extends from the top of the support. The spacers are stainless steel annular rings designed to slide on the threaded stud with minimal clearance. The spacers may be reconfigured and stacked to provide the desired swirler depth.

The swirler is made of carbon steel and has a 0.64 cm [1/4 in] tapped hole through the center that allows it to be tightened against upstream spacers. If the swirler is flush-mounted with the dump plane, the end cap is neglected; however, when recessing the swirler, appropriate spacers are stacked on top and the threaded end cap is used to secure the upper spacers. The downstream surface of the end cap is designed to remain flush with the dump plane to prevent recirculation zones (and accompanying flame anchoring) from forming inside the pipe when the swirler is recessed. The swirler location may be simply adjusted from the dump plane. The spacer and swirler are directed into position using a magnet in conjunction with a thin rod. Disassembly of the combustion vessel requires significant time and effort; thus, the custom-built mechanism is designed to serve as a functional and convenient method for changing axial position of the swirler.

2.5.4 Pressure Throttle Valve

Steps were taken towards developing a pressure throttle mechanism that allows the remote modulation of pressure during cold and hot operation. A variable sonic throat was achieved by designing and fabricating a mechanism that fundamentally features a nozzle and a plunger/needle. The pressure throttle mechanism is schematically illustrated in Figure 2.14. The needle tip, as shown in Figure 2.15, is configured to be interchangeable in the case that a more precise throat area needs to be attained. As seen in Figure 2.16, the mechanism was designed to mount to the most downstream flange of the pressure vessel reducer via steel plate. The needle was attached to a U-shaped bar that is traversed by a 5” Velmex motorized Bislid, which was mounted from beneath the steel plate - out to the side of the pressure vessel. Finally, the motorized slide was simply hard-wire controlled from the operator PC desk, using a Velmex stepper motor controller.

The in-house throttle mechanism acts as a variable sonic throat that elevates pressure within the pressure vessel. By lowering the needle, thus decreasing the exit area of the nozzle, flow becomes choked and pressure is built upstream in the pressure vessel. The mechanism, relatively simple in design, builds pressure in the vessel over a wide range of flow rates. The traversing slide is equipped with a clamp that secures the U-shaped stainless steel arm that extends the needle over to the exit nozzle. As the slide is traversed in the upstream direction, the needle plunges down into the nozzle, thereby reducing the effective area of the throat. The traversing system is supported using a steel plate, which is bolted between the reducer and the exit nozzle of the pressure vessel. High temperature graphite foil gaskets are used to provide an airtight seal around all flanged connections on the pressure vessel. The traversing needle provides a precise

method for varying the throat area of the nozzle, allowing high chamber pressure to be built independently of fuel/air flow rates; this capability is critical.

2.5.5 Ignition System

Ignition energy must be provided at the exit of the combustor; therefore, the ignition source was passed through the pressure vessel. Access through the pressure vessel was limited; hence, a probe igniter was developed and installed through one of the 1.3 cm [0.500 in] access located just above the top edge of the combustor. The ignition probe is a diode similar to a common auto engine spark plug. The probe is coaxially composed of a 3 mm [\sim 0.125 in] diameter (grade 5) titanium rod, a ceramic isolative sleeve, and a stainless steel outer casing. The ceramic sleeve provides an insulated gap for the 400,000 V driven charge to pass across at the tip of the probe. The power source from a commercial stun gun was used to supply an instantaneous voltage difference to the system. One leg of the circuit is connected to the outer casing and the other leg to the interior rod. The power supply is enclosed within a plastic casing and mounted on the side of the combustion chamber support stand. The charge is sent from the power source, and an electrical arc is created in the gap at the tip of the probe. Photographic images of the probe are provided in Figure 2.17. A Swagelok compression fitting was used to connect the ignition probe to the threaded access port. A trigger switch, safely located near the operator computer, was used to activate the igniter. In practice, the probe is manually removed and replaced by a pipe plug once the reactant mixture is ignited. The ignition probe provides a consistent technique for initiating reactions even at high flow velocities.

2.5.6 Optical Access Panel

The optical access panel, as previously stated, is a poor design in that it clamps a block of quartz to steel. The frame contacts the block, then the block contacts a surface milled into the pressure vessel. Furthermore, inherent to the clamping method, loads are applied to the frame 1.27 cm (0.50 in) out away from the outer edges of the block, as pointed out in Figure 2.18, creating some bending stress on the frame; thus, loads become uneven and concentrated at the outer edges of the block, cracking those of quartz.

An optical access panel should be one with the frame which supports it, and the frame surface should mate directly to a plane surface on the outside of the pressure vessel. Maintaining the stud pattern, the pocket in which the block rests would need to be milled out to a length and width equal or greater than those of the frame, and the new window assembly would mate with the vessel as illustrated in Figure 2.19.

Rayotek Scientific Inc. was able to supply a custom manufactured sight window that matched the original 22.86 cm x 8.89 cm desired view port and the original stud pattern. While preparing for window modifications, Rayotek also supplied a 0.50 inch sight glass that simply threads into one of the ports on the outside of the enclosure, as seen in Figure 2.20. The entire window assembly, as displayed in Figure 2.21, is 33.02 cm [13 in] in length and 20.32 cm [8 in] in width. The frame is manufactured from stainless steel 316 and the transparent panel, high temperature quartz. Rayotek rates the sight windows for a maximum pressure and temperature of 150 psi and 1000 °C, respectively.

2.6 Instrumentation and Data Acquisition

2.6.1 Flow Measurement

As previously mentioned, LFEs are utilized for determining both cooling and combustion air mass flow rates. MERIAM, model 50MW20 LFEs are calibrated for a volumetric airflow rate of 0 to 1400 liters per minute. A differential pressure transducer connects to upstream and downstream ports of the LFE and measures the pressure drop. Temperature is measured upstream of the LFE, and absolute pressure is measured downstream of the LFE. Output current signals from pressure transducers and output voltage signals from thermocouples are networked to the NI CompactRIO system for signal conditioning and data acquisition. The data is acquired, and the total air mass flow rate through the LFE is calculated - using NI LabVIEW software. An example calculation is included in Appendix C. A Bonkhorst EL-FLOW, model F-203AV-M50 mass flow controller is used to measure and control the fuel flow rate. Manufacturer provided software is used in conjunction with the NI CompactRIO system current output module to control the set point of the mass flow controller. To insure proper operation, fuel flow rate is calculated and displayed prior to activation of the controller. A complete list of instrumentation used for air and fuel flow measurement is given in Table 2-3.

Table 2-1

Instrumentation used for flow measurement

| Description | Model | Range | Output Type | Accuracy* |
|------------------------------|---------------------------|-----------------------------|-------------|-----------------------------------|
| Laminar flow element | MERIAM 50MW20 | 1400 LPM | N/A | 0.72% reading |
| K-type thermocouple | Omega KQSS-14G-10 | 1250 °C | Voltage | 0.75% reading |
| Absolute pressure sensor | Omega MMA150 | 150 psi | Current | 0.20% reading |
| Differential pressure sensor | Omega MMDDU10WC | 10 in H ₂ O | Current | 0.03% reading |
| Mass flow controller | Bronkhorst F-203AV-M50 | 465 LNPM of CH ₄ | Voltage | 0.5% reading + 0.1% full scale |

2.6.2 Pressure and Temperature Measurement

Combustion chamber pressure is measured with an absolute pressure transducer connected through an access port in the wall of the pressure vessel. The transducer output is wired to the NI CompactRIO data acquisition system and displayed in LabVIEW software. Temperature is measured at several locations within the system. As previously mentioned, Type K thermocouples are used to measure air temperature inside the heater, at locations prior to LFEs, and at a location 30.5 cm [12 in] upstream of the combustor dump plane. In addition, combustor outer surface temperatures and exit plane

temperature are monitored using three Type K thermocouples, mounted through access ports in the pressure vessel. Thermocouple signals are networked to the NI CompactRIO chassis and displayed using LabVIEW software.

2.6.3 Acoustics Measurements

SPL is measure at two locations. A flush mounted dynamic pressure transducer measures combustion noise at a location level with the top of the combustor, and a condenser microphone measures jet noise from a safe distance (~ 1 m) at 30° above the horizontal plane of from the pressure vessel exhaust nozzle. Measurements are made at these locations to observe any correlation between direct and indirect combustion noise. Combustion noise is measured with a PCB Piezotronics, model 113B28, water-cooled dynamic pressure transducer. Sensor output is sent to a PCB, model 482A17 signal conditioner, where the voltage signal is amplified. Finally, a NI PCI-6254 multifunction data acquisition card, embedded in a laboratory computer equipped with LabVIEW software, digitizes the voltage signals. LabVIEW software is then used to scale the voltage signal to a pressure one, using the sensitivity of the transducer (15.06 mV/kPa).

Similarly, a Bruel & Kjaer (model 8149) condenser microphone measures jet noise. The NI PCI-6254 data acquisition card digitizes the microphone signal, and the voltage signal is converted to a pressure one using the microphone sensitivity (45.8 mV/Pa). The condenser microphone is calibrated by the manufacturer and periodically verified with a 114 dB, 251.2 Hz piston-phone. Sound pressure measurements of both instruments are sampled at 4000 Hertz (Hz). Scaled voltage signals are processed using a LabVIEW embedded fast Fourier transform (FFT) function to obtain root mean squared (RMS) pressure fluctuations vs. frequency. A unique Matlab script calculates SPL from

RMS pressure fluctuations using Equation 3.1 (Bussman, 2001). See Appendix D for further details regarding Matlab code.

$$SPL = 10 * \log_{10} \frac{P_{rms}^2}{P_{ref}^2} \quad (2.2)$$

where $P_{ref} = 20 \mu\text{Pa}$. Total SPL is calculated by:

$$SPL_{total} = 10 * \log_{10} \left(\sum_{i=1}^n 10^{0.1 * SPL_i} \right) \quad (2.3)$$

2.6.4 Data Acquisition System

Sound pressure signals are acquired by the aforementioned data acquisition card and processed in LabVIEW. An NI CompactRIO system acquires data from all other measurement devices. The NI CompactRIO system, featuring 4 NI C series input modules, is displayed in Figure 2.22. NI CompactRIO is a robust data acquisition and control system capable of sending and receiving current and voltage signals at high data rates. The system includes a reconfigurable chassis, which can accommodate up to eight I/O modules, and contains a field-programmable gate array (FPGA) chip. The current CompactRIO chassis houses four I/O modules: one 32-channel 10 V voltage input, one 16-channel preconfigured thermocouple input, one 8-channel 20 mA current input, and one 4-channel 20 mA current output. Figure 2.23 shows the layout of the flow measurement sensors along with their respective I/O connections to the individual C series modules.

To avoid task priority conflicts associated with a Windows based operating system, the FPGA chip performs all of the signal conditioning. The real-time controller

embedded in the NI CompactRIO acts as a standalone PC and makes use of a 533 MHz processor, 2 GB of storage, and 256 MB of RAM. The real-time controller links directly to the operator PC using an Ethernet cable. The devoted operator PC is equipped with LabVIEW software that post-processes data from the CompactRIO. A virtual control panel (shown in Figure 2.24) is created in LabVIEW and serves as the user interface for calculation display and output control. Furthermore, the operator PC features software supplied by Bronkhorst that couples with the NI CompactRIO current output module to provide user control of the fuel mass flow controller. As a safety measure, the fuel flow rate is controlled via separate software. The fuel flow rate is manually entered into LabVIEW, and the equivalence ratio is calculated. The user is able to predict a resulting equivalence ratio for any given fuel flow rate. In other words, a desired value for fuel flow rate is established before delivering any fuel to the combustion chamber.

The present LabVIEW program is a graphically based three-step process involving the FPGA chip, the real-time controller, and the operator PC. First, the embedded FPGA chip is programmed to read signals at a desired sampling rate and provide initial signal conditioning. The FPGA chip is only reconfigured when the FPGA file, featuring the real time target, is modified. For this reason, the compactRIO is a highly reliable device capable of standing alone. Next, the real-time controller is programmed to receive and temporarily store data from the FPGA chip, reducing risk of hardware failure. For these reasons, the real-time controller is also used to perform a majority of the signal scaling and mathematical calculations. Finally, the PC itself is programmed to read data from the real-time controller. Information from the controller is sent to the operator PC where it is conveniently displayed in the LabVIEW graphical

interface, which allows the user to monitor system parameters and send instructions to the controlled devices.

2.7 Operating Procedure

2.7.1 Preliminary Tasks

The high-pressure combustion facility is a powerful system capable of harnessing large heat release rates, temperatures, and pressures when operated properly. As a result, a strict operating procedure is developed and precisely adhered to for all experimental operation of the system.

First, the windows and/or the reducer are removed to allow access to the inside of the combustor. Next, the pressure vessel is visually inspected for any signs of component malfunction or excessive wear and tear. Swirler location is adjusted if needed. Porous media is placed on the dump plane, followed by the combustor and mounting ring. The combustor apparatus is fastened in place with four ¼” nuts. Next, the ignition probe is mounted through a designated access port. After all interior components are in place; the reducer is mounted along with the exit nozzle and pressure throttle mechanism. The variable sonic throat is verified fully open to prevent pressure buildup prior to ignition. At this point, all bolted connections are checked for proper tightness and fit. Next, the operator PC is turned on and appropriate LabVIEW software is initiated to display various measurements and calculations. Next, the pressure throttle mechanism is tested. A remote toggle stick is wired from the high-pressure vessel to the operator PC desk. Satisfaction is achieved when the needle traverses between its two maximums flawlessly, then it is returned to the fully open position.

Finally, a three-panel blast-proof safety enclosure is placed between the high-pressure vessel and the operator to prevent injury during any potentially catastrophic malfunction. Once preliminary tasks are completed; airflow is initiated through the system.

2.7.2 Air Flow

First, the manual air supply valve is opened - regulator setting the desired supply pressure. Then, the LabVIEW interface may be used to finely adjust the automated control valve to achieve the desired airflow rate. Next, the globe valves in the cooling and combustion airlines are manually adjusted to produce a specified split between cooling and combustion airflow rates. Cooling air is adjusted such that 1/3 of the total airflow is delivered through the cooling line when operating at critical pressures. At this time, the electrical heater may be turned on to preheat the combustion airflow. If the heater is used, the combustor inlet temperature is monitored until the desired temperature is achieved. Once the desired airflow rate and inlet temperature are achieved, system diagnostics are examined via the LabVIEW control panel. Any issues are addressed systematically. Once the system is functioning properly, fuel flow is safely initiated.

2.7.3 Fuel Flow and Ignition

First, the electrical shutoff valve is verified closed. Then, the manual gate valves (both valves are located on the building column) are opened. Fuel pressure is adjusted with the fuel pressure regulator, located downstream of the manual gate valve. Percentage fuel values (0 - 100%) are next entered into the LabVIEW interface to determine the required value to supply via the Bronkhusrt software for a desired equivalence ratio. The percentage fuel value represents the percentage that fuel flow

controller is open - zero corresponding to fully closed and one hundred, fully open. The resulting equivalence ratio is calculated and displayed in LabVIEW. The fuel control process is slightly convoluted, but added safety is provided for the operator. Once the desired equivalence ratio is established, the ignition probe is triggered from the operator PC. After successful ignition, the probe is removed from the access port and replaced with a plug.

2.7.4 Pressure Elevation

Vital temperature and pressure measurements are monitored throughout the remaining process. When ignition is successful, and a stable flame rests just above the dump plane of the combustor. Now, the supply pressure is adjusted such that it corresponds to a maximum desired chamber pressure, which will be ultimately achieved by reducing the most downstream variable throat area via the pressure throttle mechanism. Once a stable form of the desired equivalence ratio is achieved, the throttle mechanism is activated. Jogging the traversing slide from the operator PC desk lowers the needle. Once choking begins, the needle is lowered in increments so that the fuel supply can be adjusted to maintain a stable form of the desired equivalence ratio. Shortly, the desired chamber pressure is reached.

2.7.5 System Shutdown

A shutdown procedure is firmly followed to prevent temperature or pressure driven component failure. For low-pressure operation, fuel supply is disabled by manually closing the most upstream (primary) fuel gate valve, and all residual fuel burnt out. Then, all fuel supply valves are closed from upstream to downstream. Next, the electric heater is shut off. Air is continuously supplied to the system until all components

are sufficiently cooled. Finally, once all components have cooled, the air supply is shut off by manually closing the airline most upstream gate valve. For high-pressure operation, the fuel and air shutoff procedure is the same as that of low-pressure operation; however, chamber pressure is relieved before the procedure begins. Opening the pressure throttle mechanism gradually reduces the chamber pressure, and the fuel/air mixture is gradually adjusted accordingly. Once the chamber pressure has equalized with atmospheric pressure, the previous shutdown procedure is implemented. Lastly, the system is inspected for fatigue and component damage.

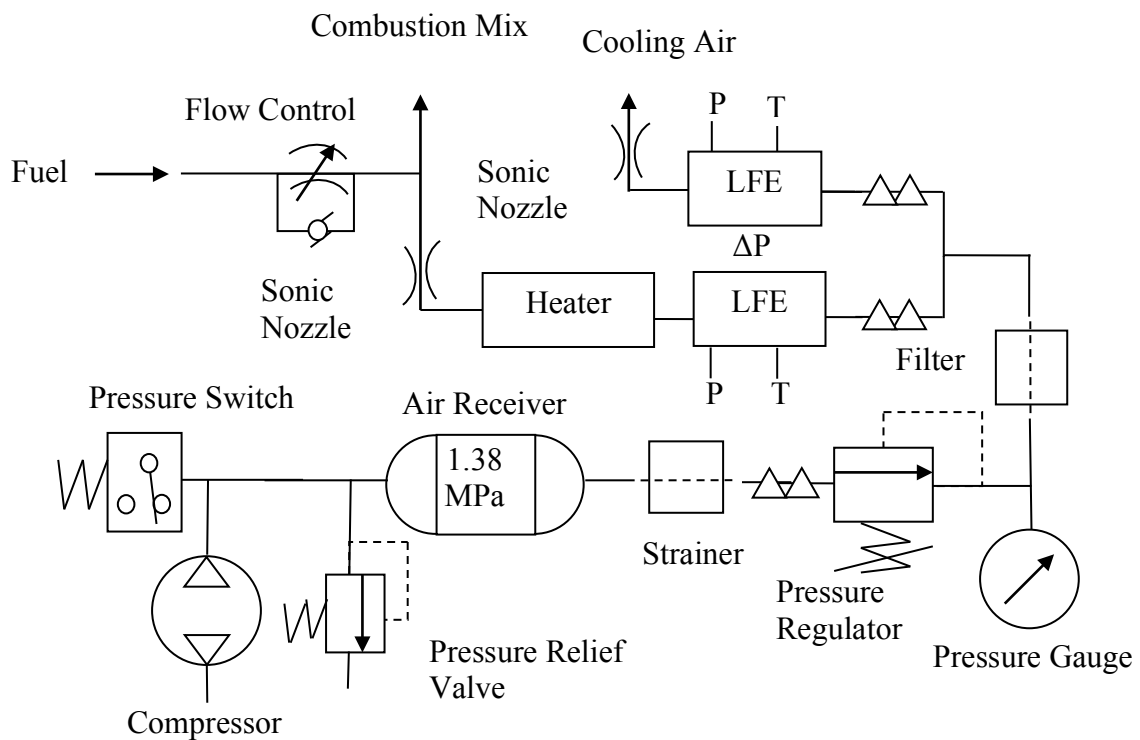


Figure 2.1. Schematic of fuel/air supplies and instrumentation

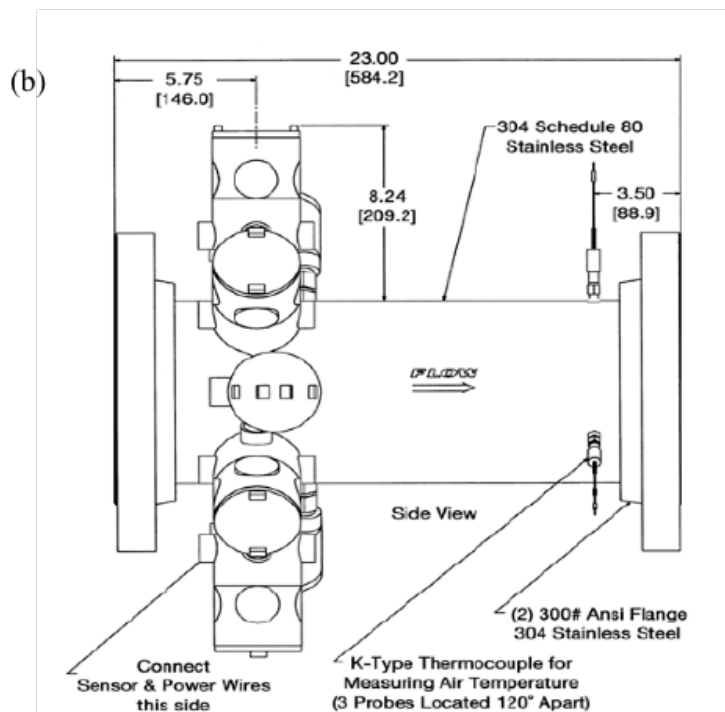
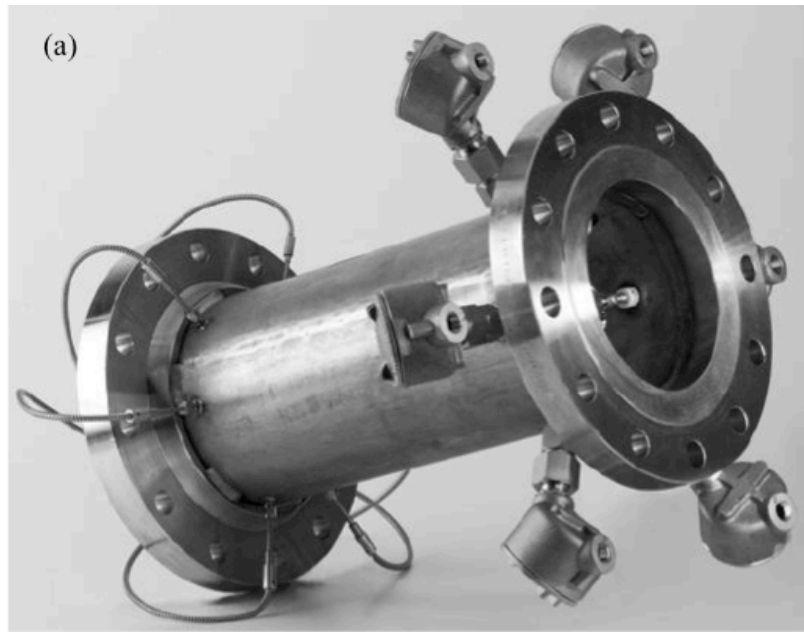


Figure 2.2. Electric air heater (a) Photographic image (b) Schematic diagram

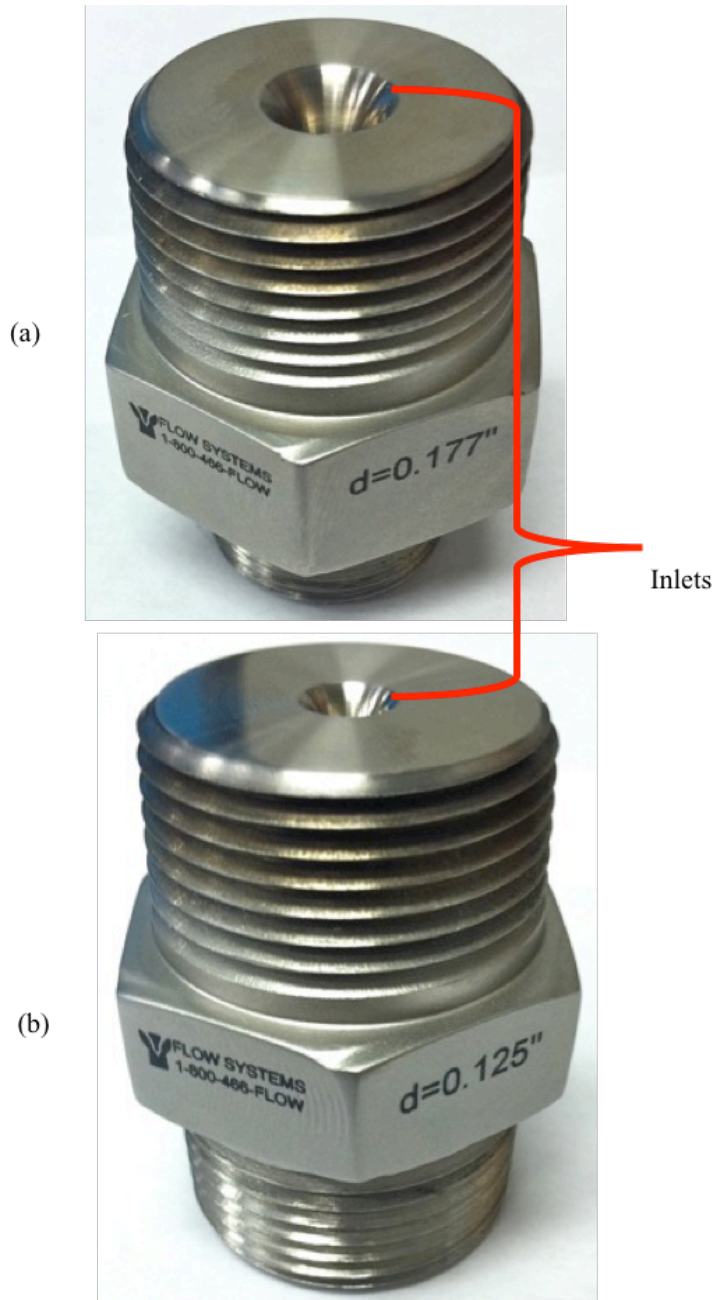


Figure 2.3. Photographs of sonic nozzles for (a) Combustion air (b) Cooling air

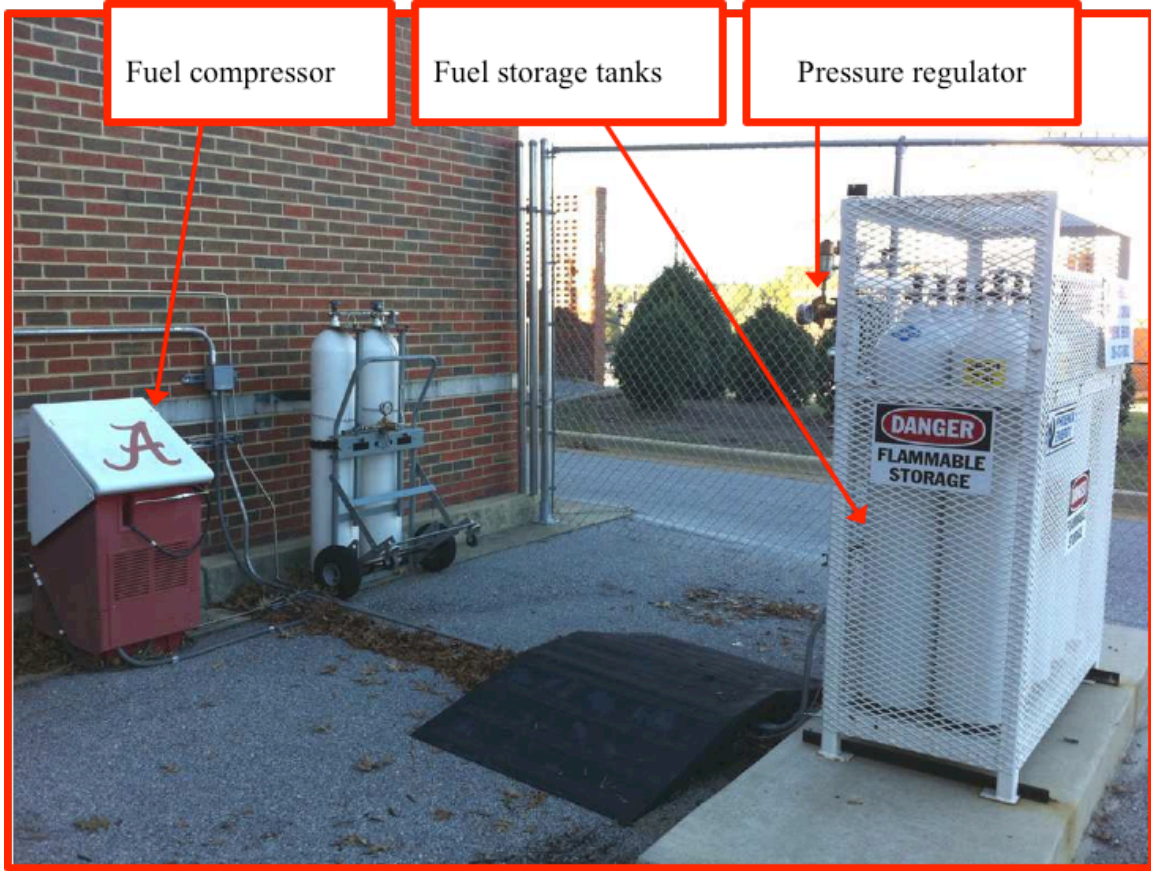


Figure 2.4. Outdoor fueling station

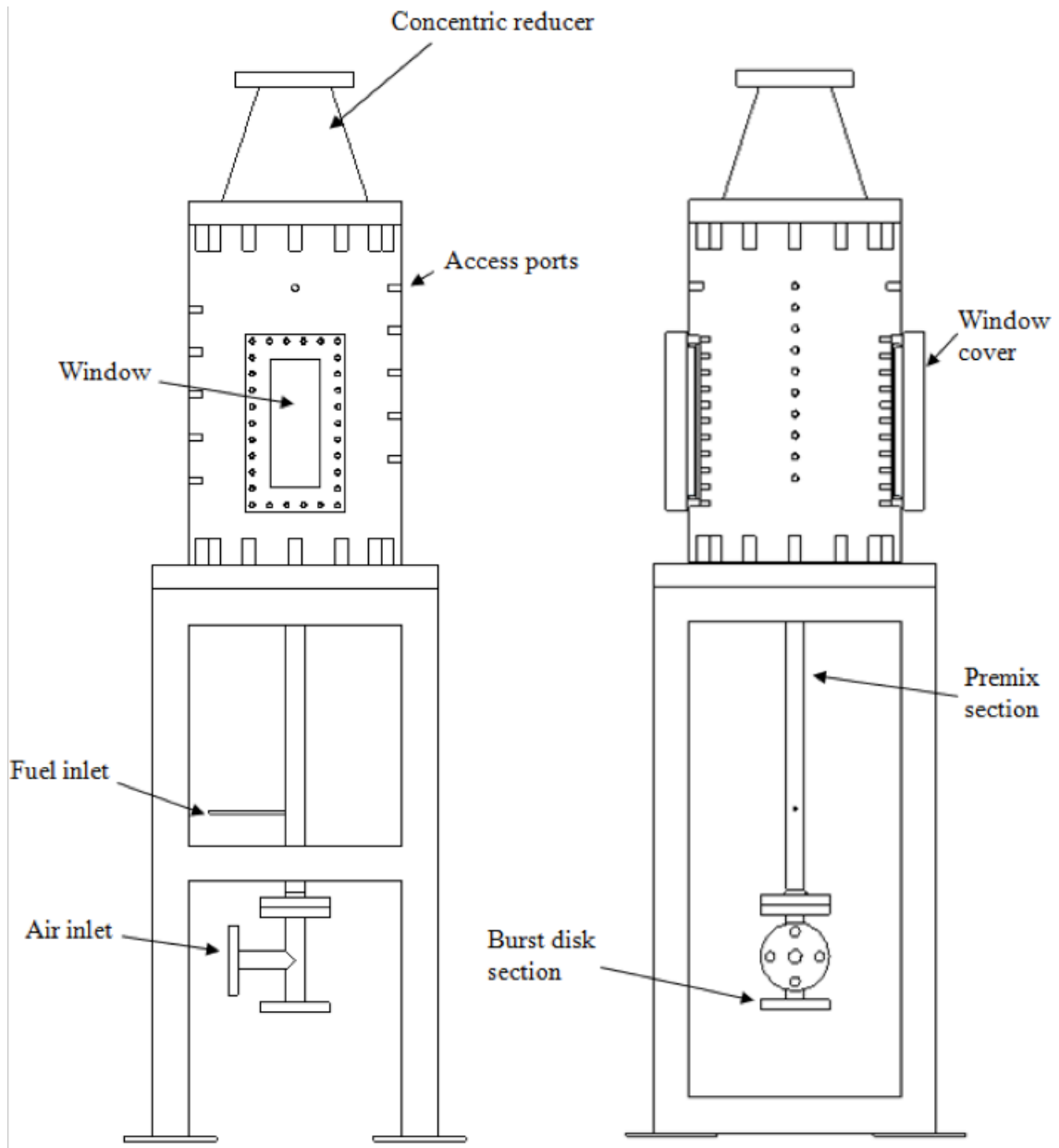


Figure 2.5. Schematic of assembled experimental apparatus

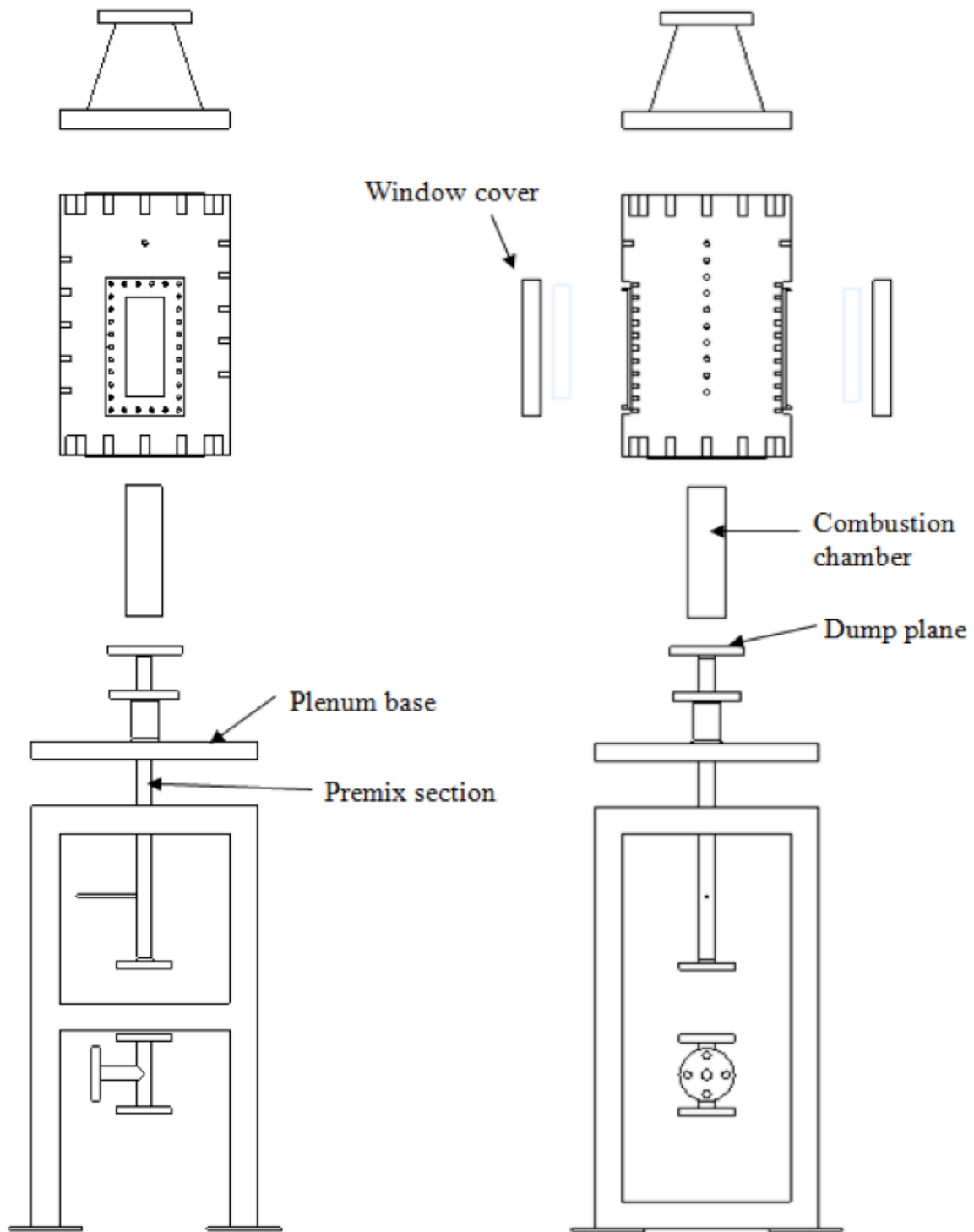


Figure 2.6. Exploded view of experimental apparatus

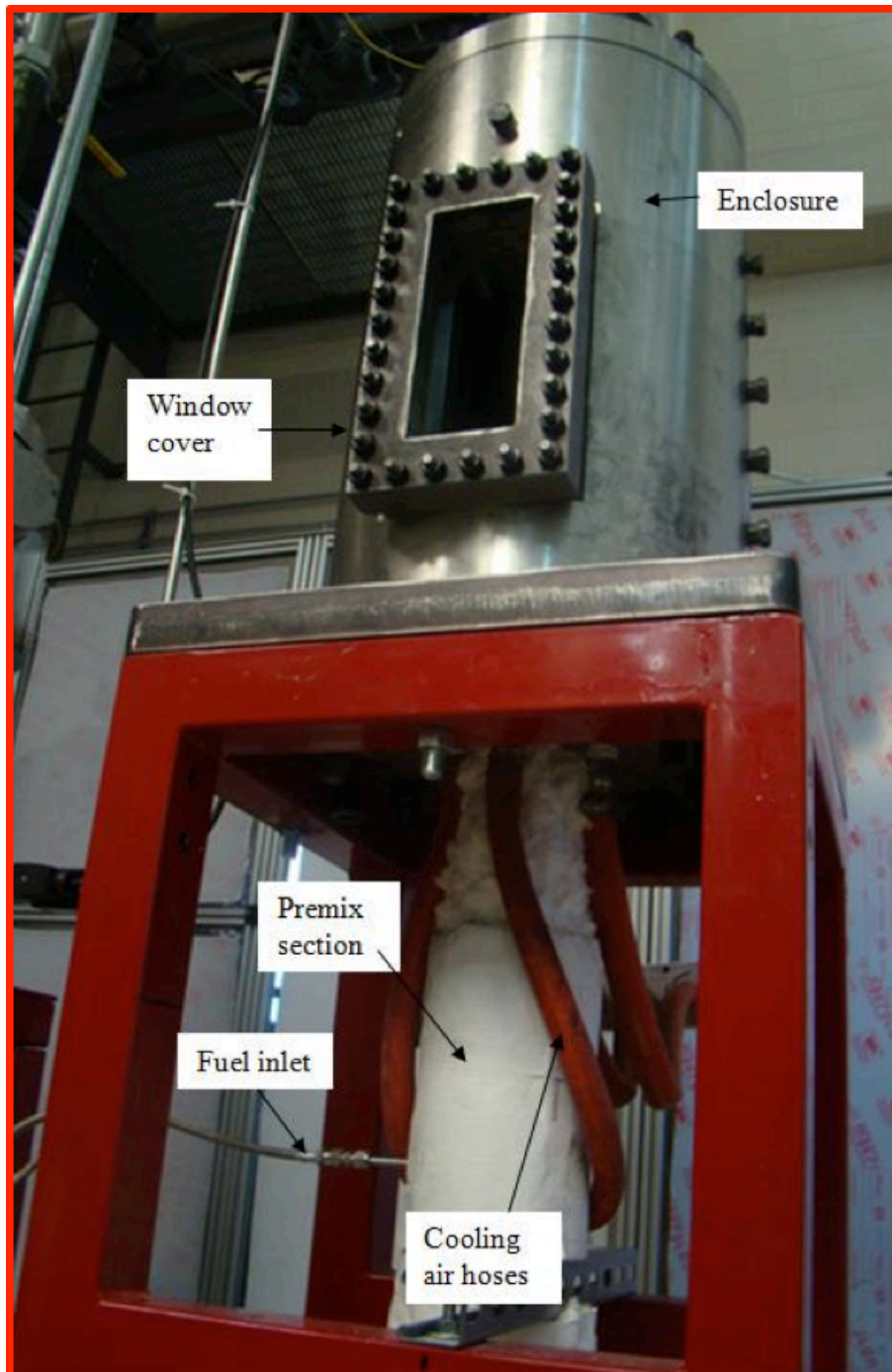


Figure 2.7. Photograph of experimental apparatus premix section and cooling air hoses

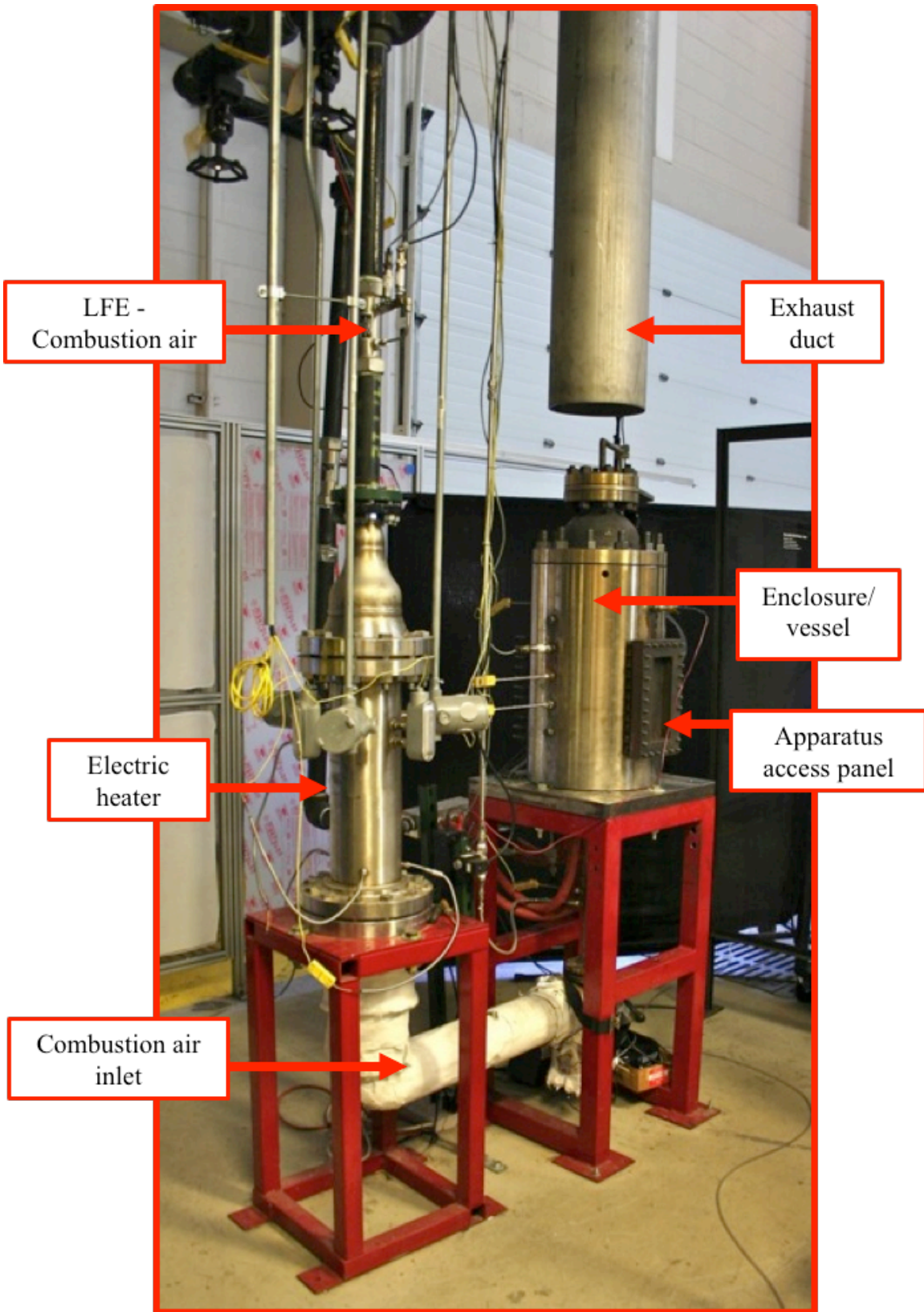


Figure 2.8. Photograph of experimental setup with high-pressure enclosure/vessel

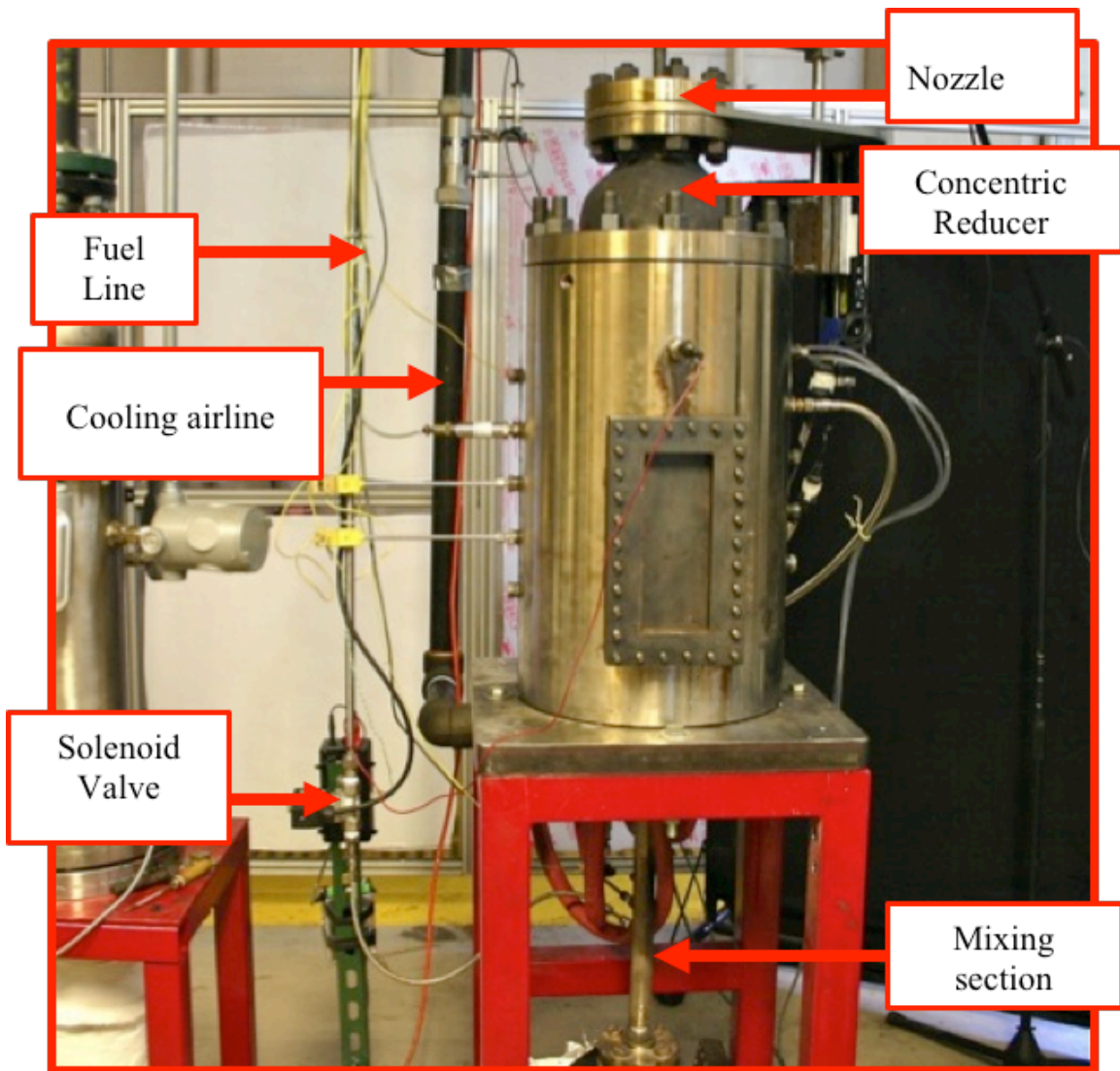


Figure 2.9. Photograph of high-pressure vessel/enclosure

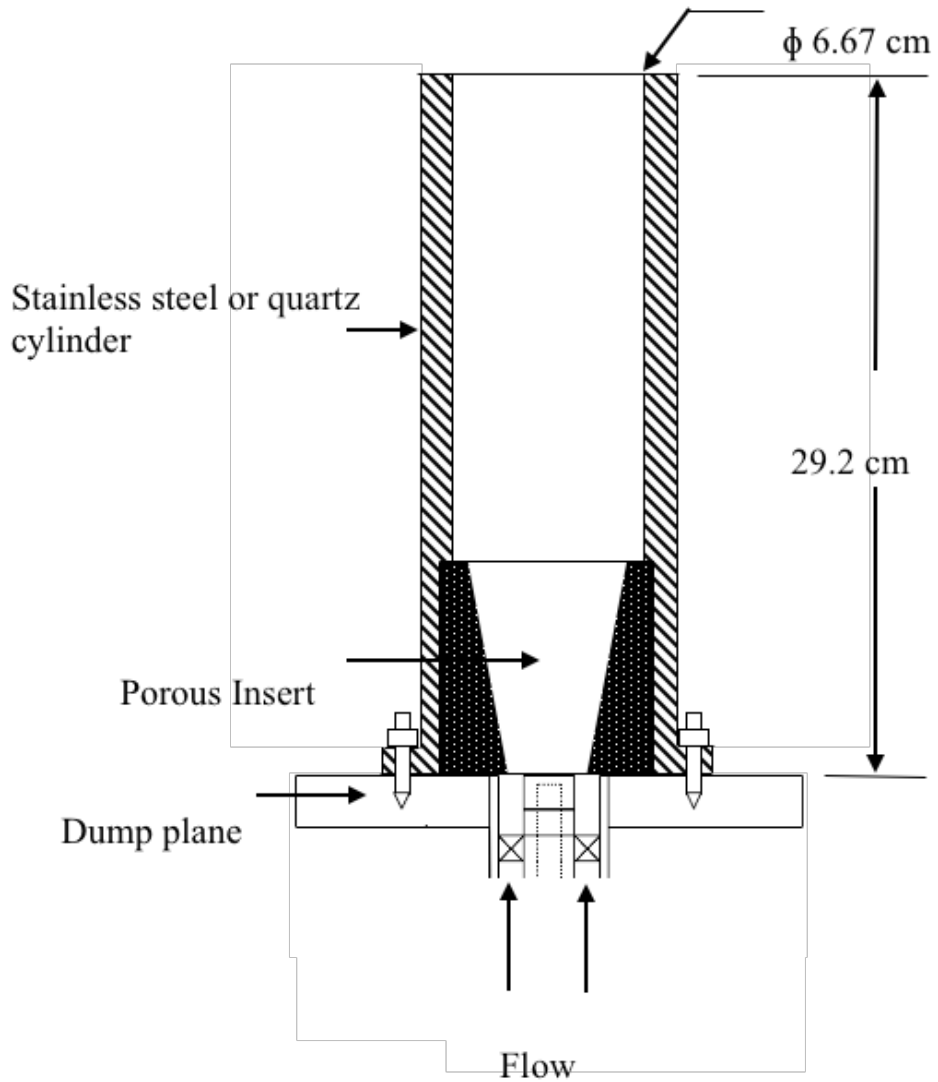


Figure 2.10. Combustor and PIM orientation with dump plane



Figure 2.11. Photographic image of swirler

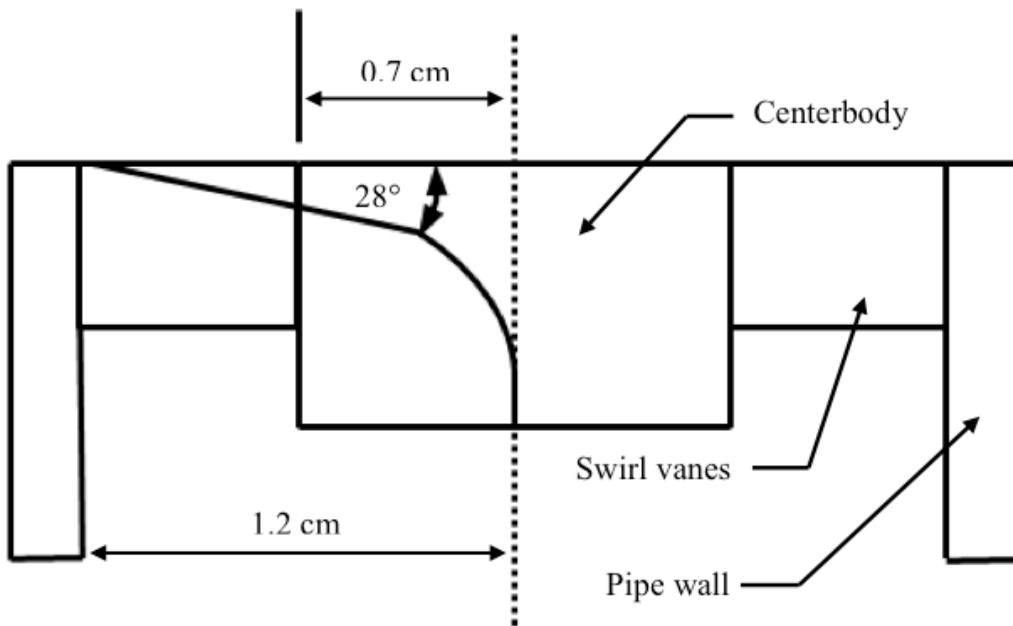


Figure 2.12. Detailed drawing of swirler

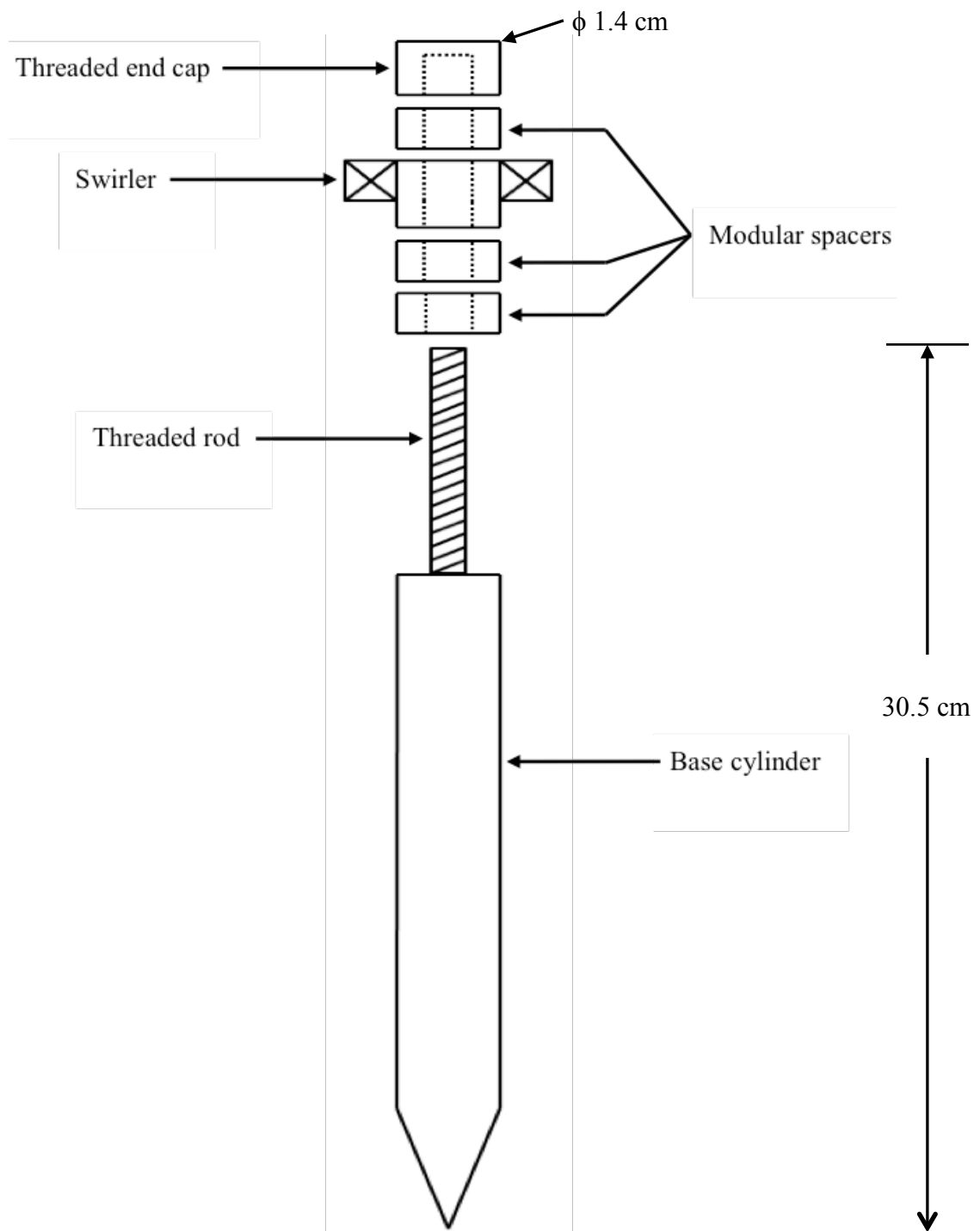


Figure 2.13. Exploded drawing of variable swirler mechanism

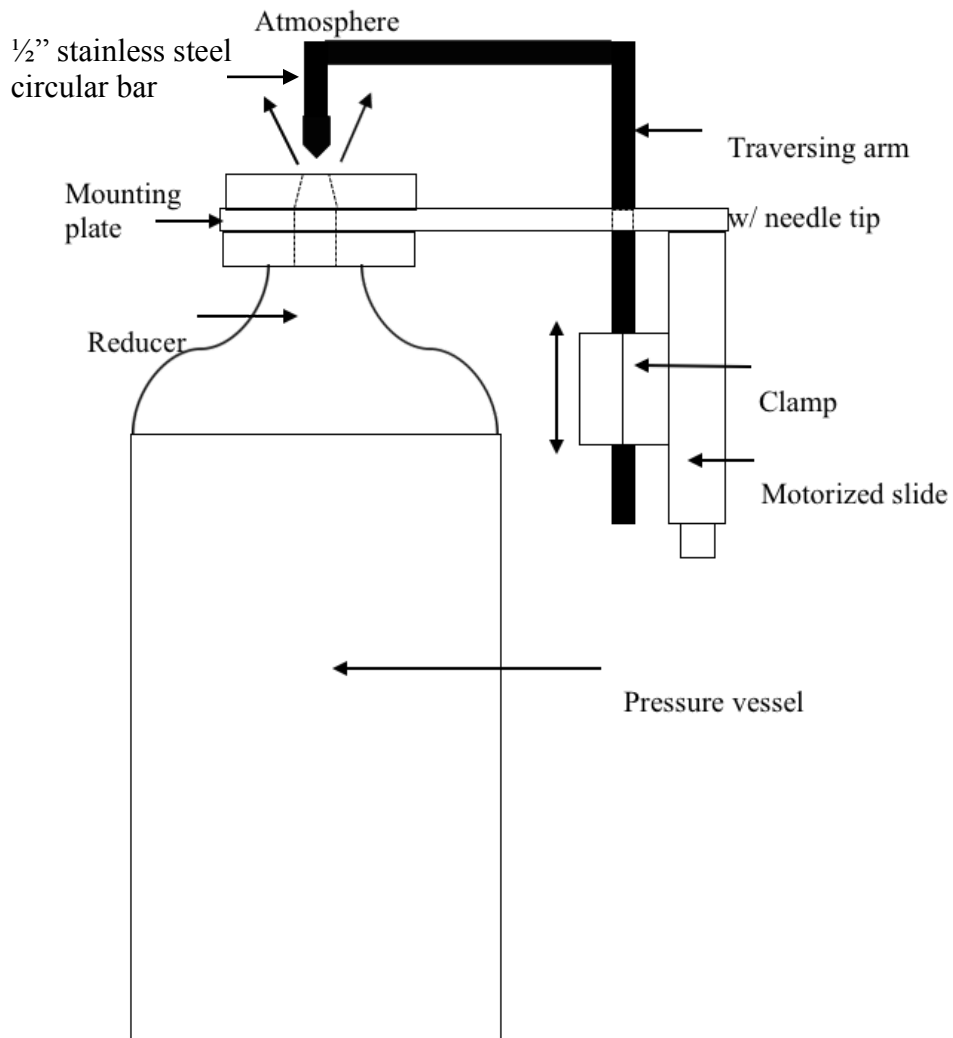


Figure 2.14. Schematic drawing of pressure throttle mechanism mounted to enclosure

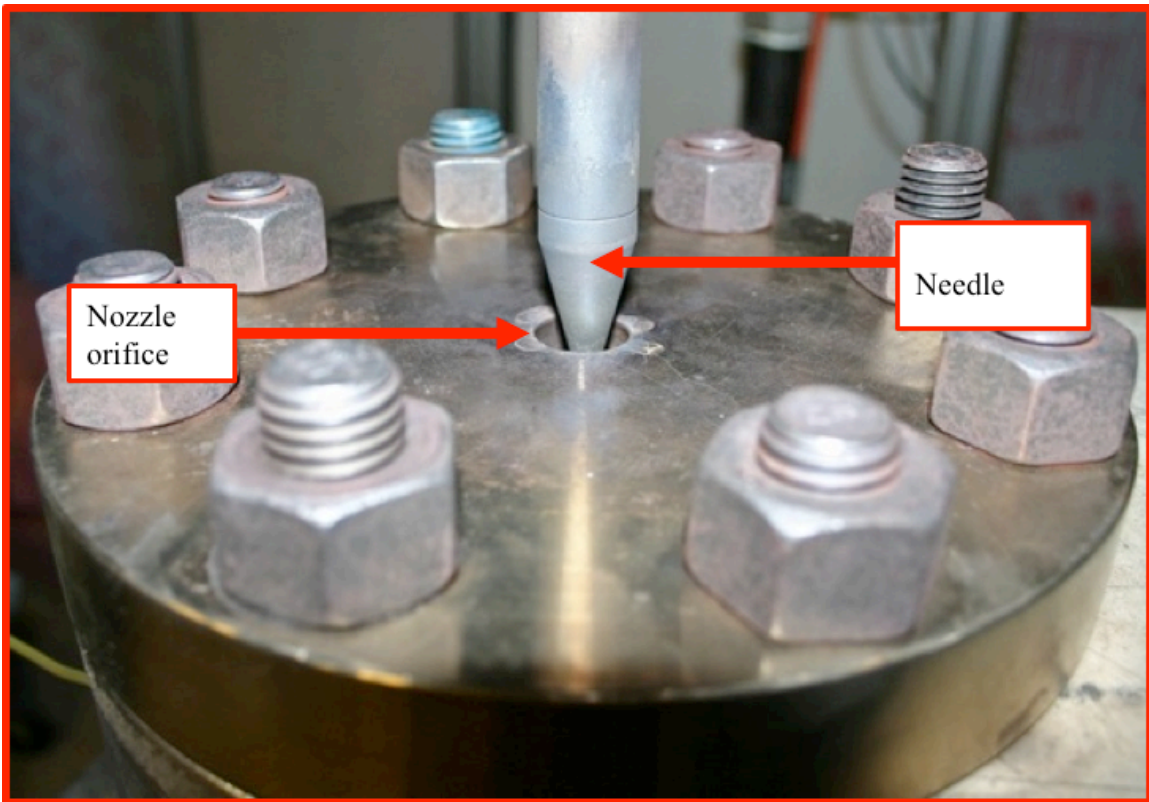


Figure 2.15. Photograph of orifice plate and throttle needle

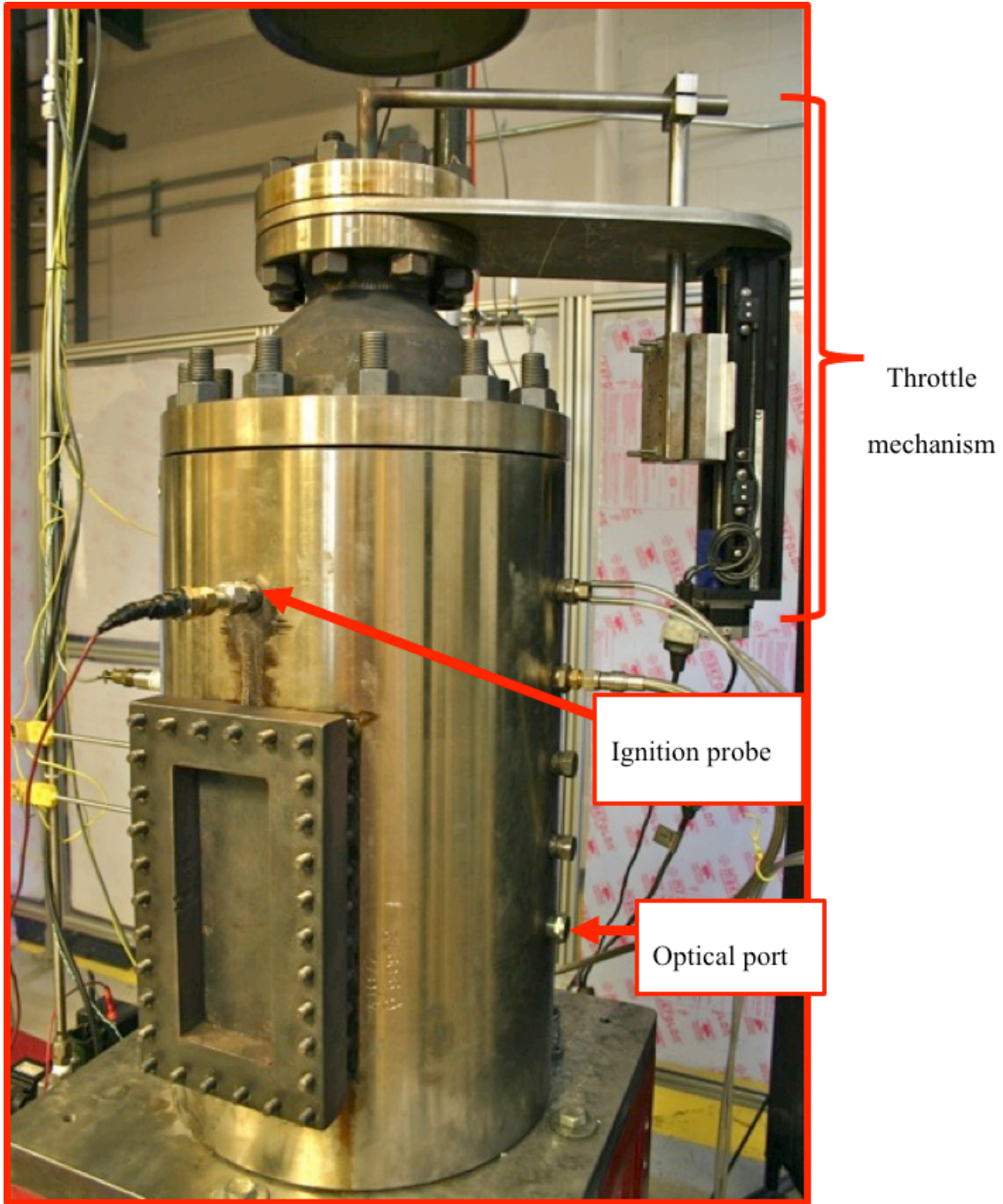


Figure 2.16. Photograph of throttle mechanism mounted to reducer via steel plate

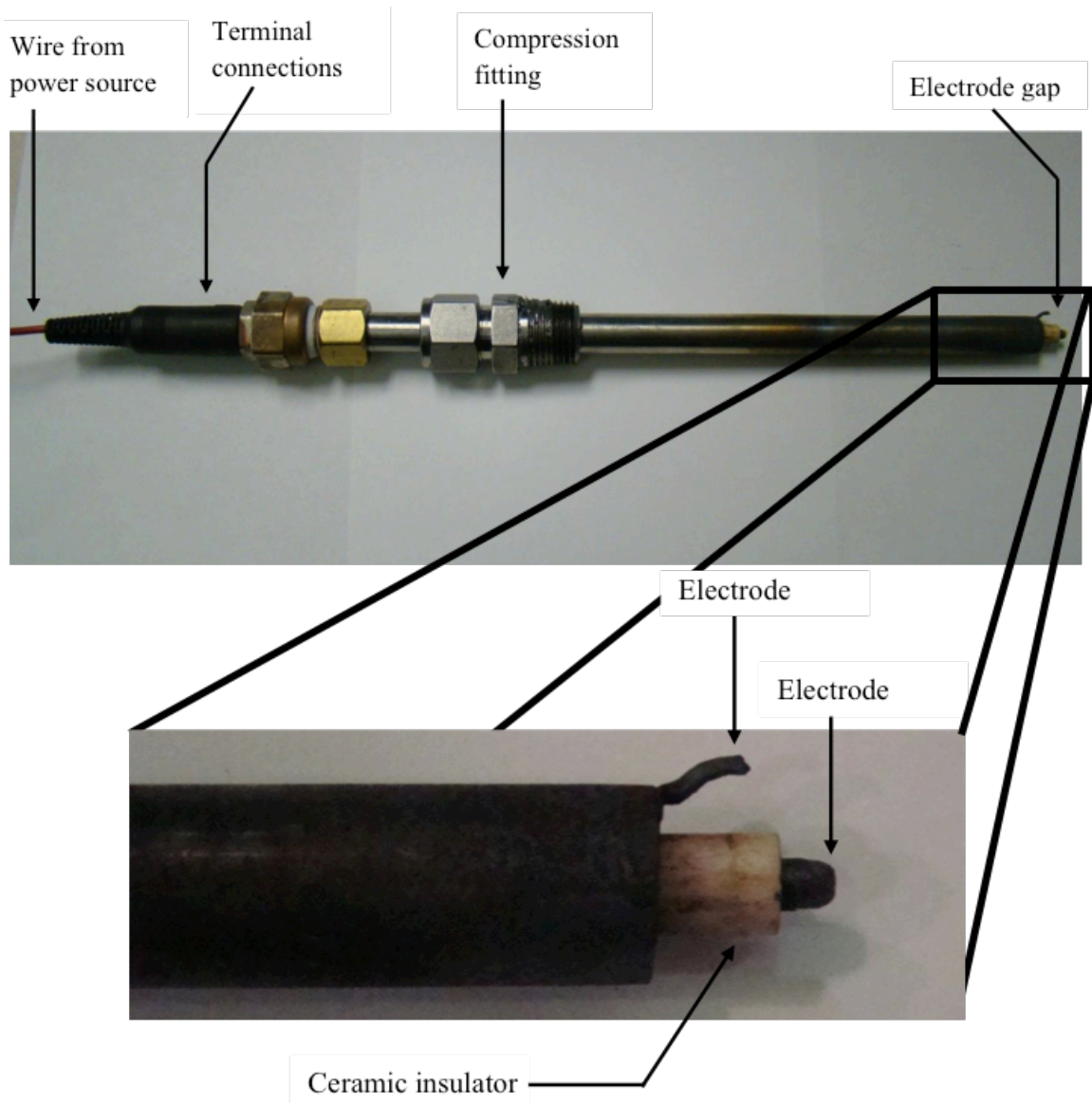


Figure 2.17. Photograph of ignition probe

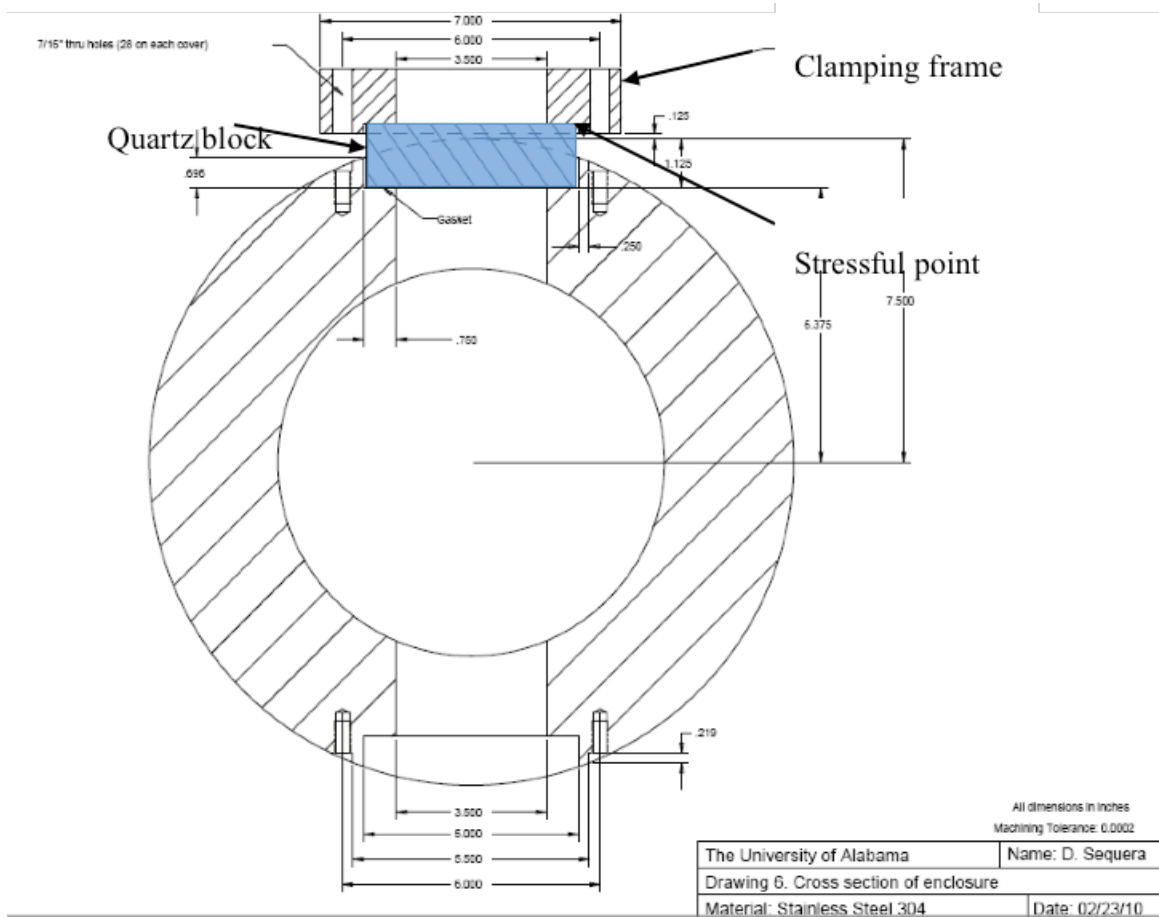


Figure 2.18. Top view of enclosure, pointing out previous window clamp

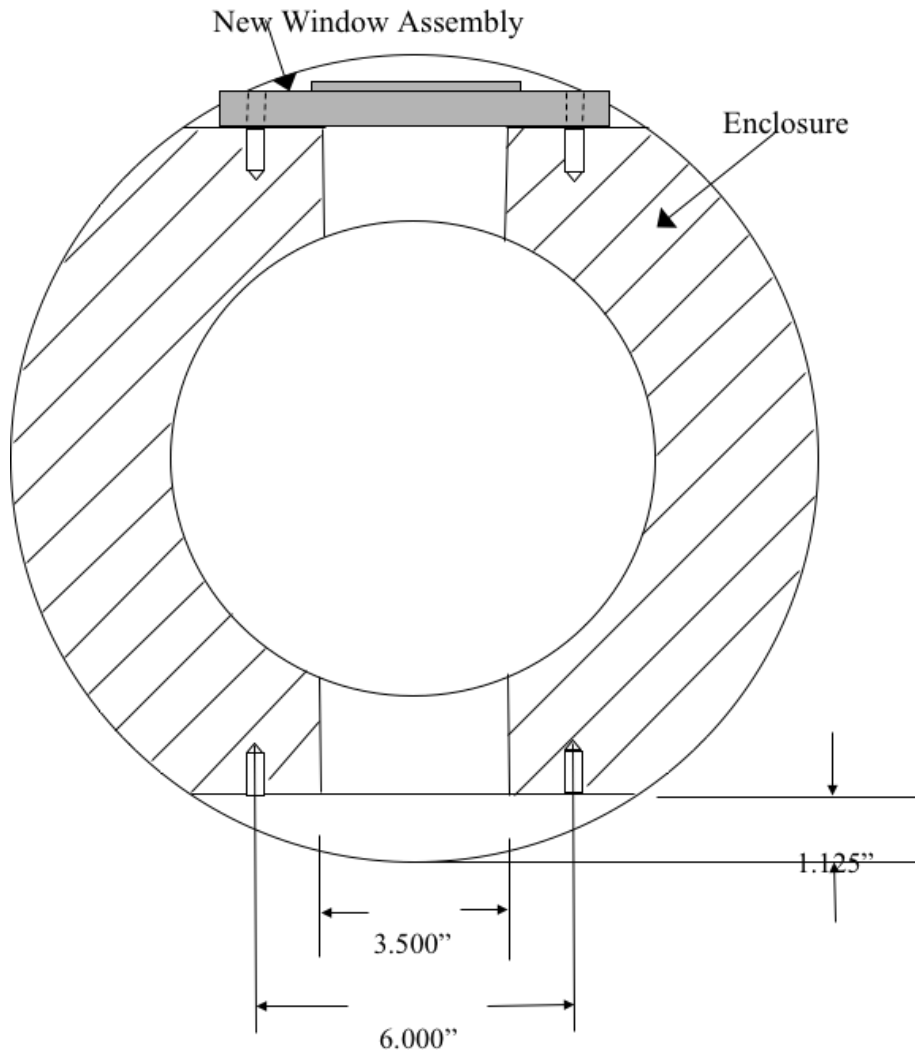


Figure 2.19. Top view of preferred enclosure modifications for new window assembly



Figure 2.20. Rayotek sight glass that threads into a 0.50 inch NPT port on the enclosure

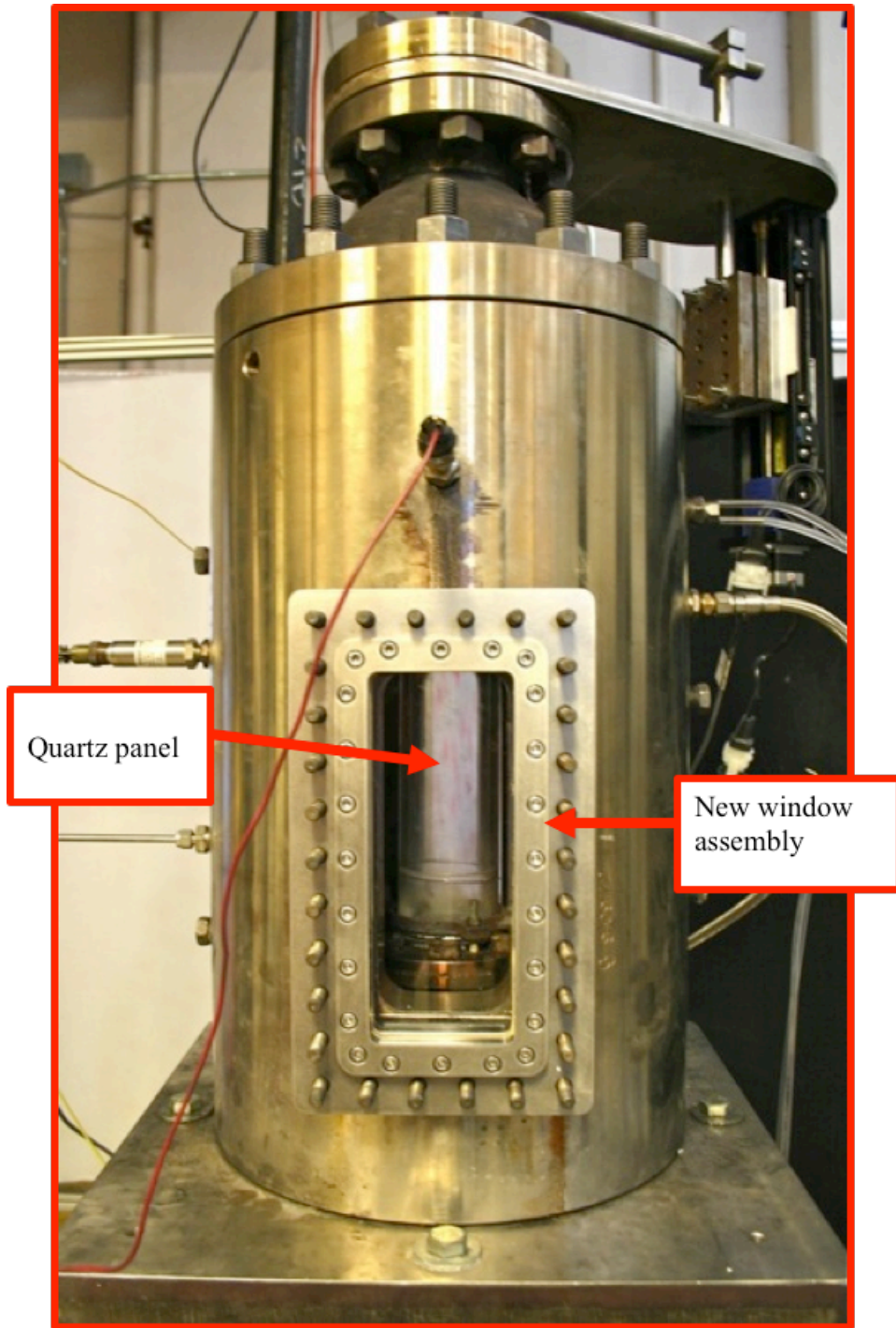


Figure 2.21. Photograph of new window assembly mounting to enclosure

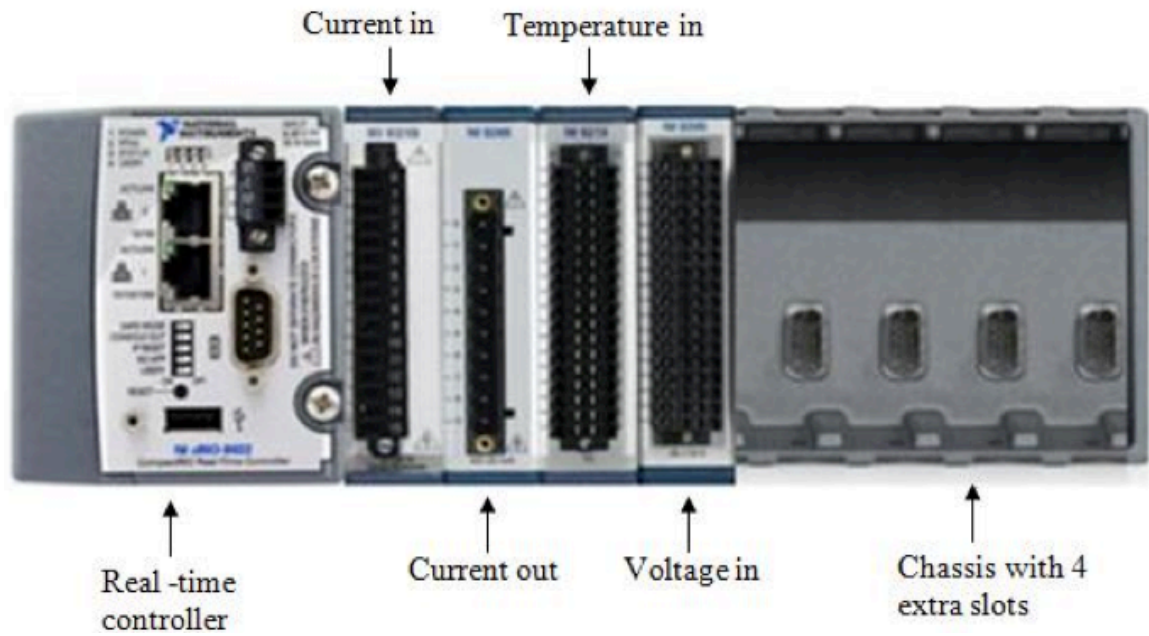


Figure 2.22. Layout of NI CompactRIO data acquisition system

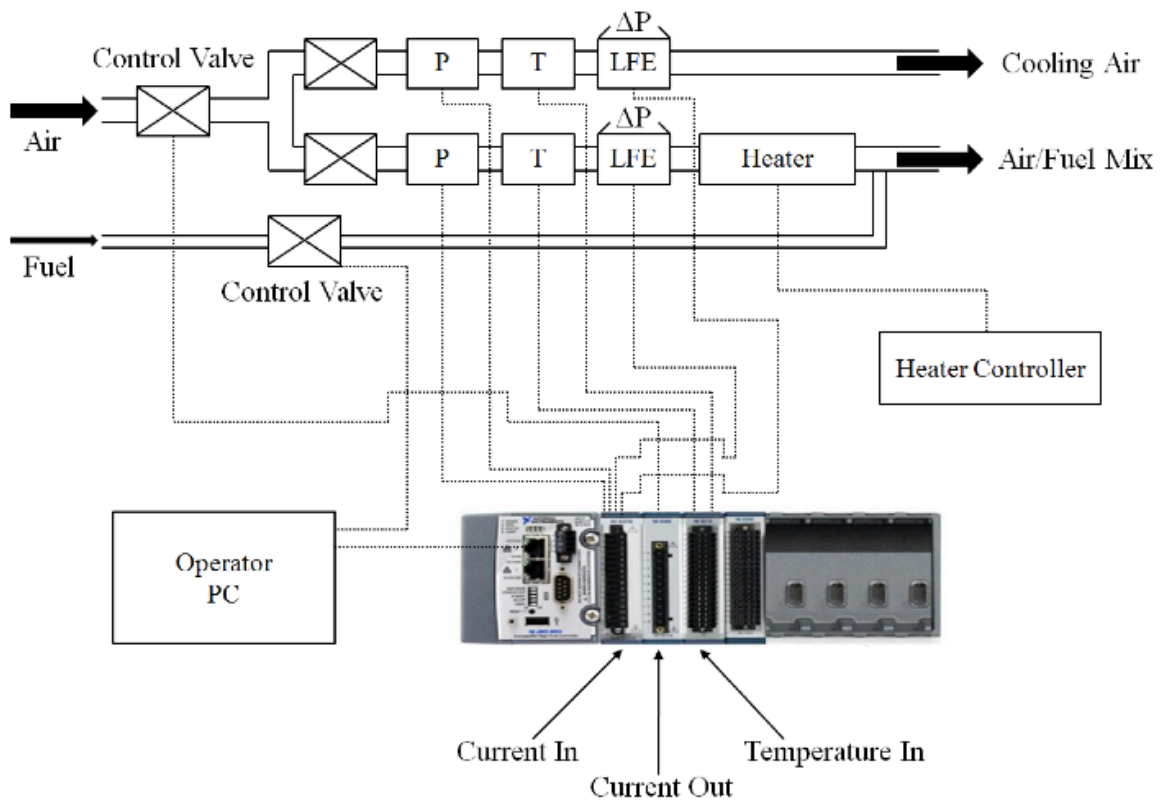


Figure 2.23. Schematic layout of flow control system

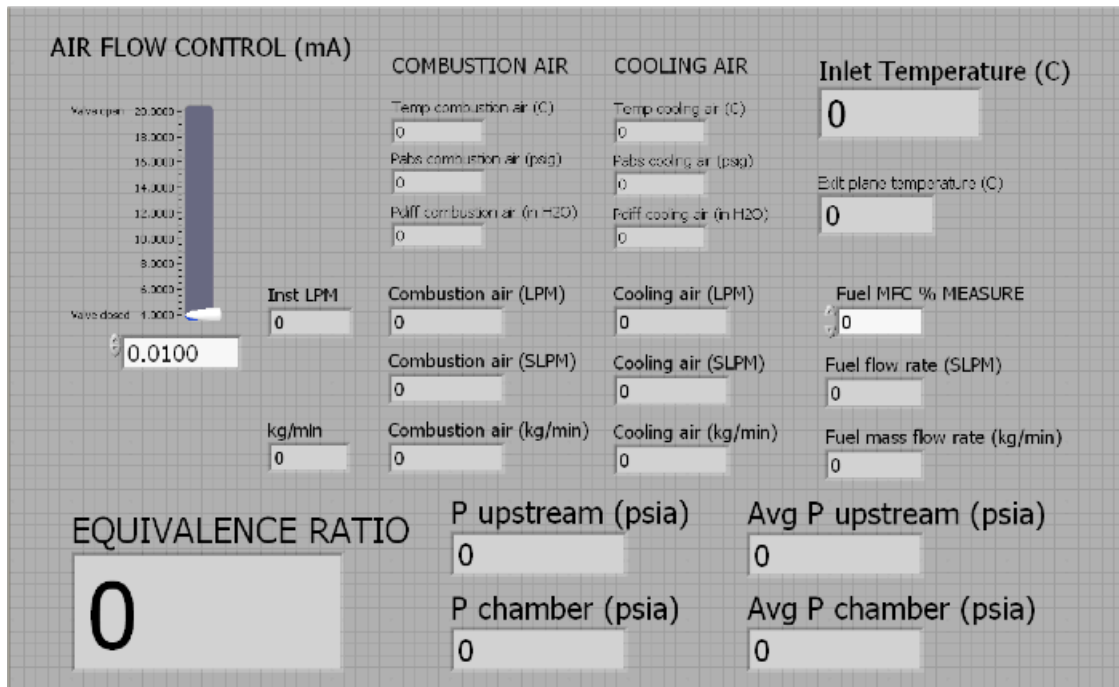


Figure 2.24. LabVIEW flow measurement front panel as displayed on operator PC monitor

CHAPTER 3
SUPPRESSION OF COMBUSTION DRIVEN THERMO-ACOUSTIC
INSTABILITIES USING POROUS INERT MEDIA

3.1 Overview

Emissions regulations in the United States are becoming increasingly stringent. Gas turbine operators must continue to develop cleaner low-emission combustion systems. Nitrogen oxides (NO_x), the major smog constituents, are the most alarming of combustion byproducts. Combustion systems capable of producing low double-digit NO_x emissions are becoming common; however, across all states, single-digit NO_x emissions may soon be required. Among successful techniques for achieving very low NO_x emissions, is lean-premixed (LPM) combustion, a process in which fuel is sufficiently mixed with excess oxidizer prior to combustion.

Special issues arise when burning mixtures near the lean limit. LPM systems are vulnerable to flow and mixture fluctuations that can lead to extinction, blow-off, or flashback. Such issues are commonly eliminated by inducing a tangential or swirl velocity to reactants upstream of the combustion chamber. Swirl-stabilized LPM systems features a sudden expansion downstream of the swirler, and the sudden expansion of swirling flow creates central and corner recirculation zones within the combustor that maintain combustion by mixing hot product gases with incoming reactants. Turbulent recirculation zones are speculated to be the dominant source of direct combustion noise and instability in swirl-stabilized LPM gas turbine combustion systems (*Huang and Yang, 2005; Stone & Menon, 2002; Sequera & Agrawal, 2011*)

Combustion instabilities arise when heat driven pressure fluctuations, or combustion noise, couple with the natural acoustic field of the system to produce acoustic resonance. Although gas turbine combustion instability is a relatively new field driven by regulation, combustion instability is a classic topic of concern in the area of rocket propulsion. Countless investigations have been conducted to either actively or passively mitigate combustion noise and instability in rocket engines since the mid 20th century (*Huang & Yang, 2009*). Active techniques are still very costly and unreliable. Passive methods, involving the use of various forms of fuel and oxidizer injection, alteration of combustion chamber geometry, and addition of dampers, have been successfully tested, demonstrated, and implemented into practice (*Noiray et al., 2009; Stone & Menon, 2002;*). The present study investigates an innovative passive stability control technique that is hypothesized to mitigate combustion noise and instability for a variety of gas turbine operating conditions.

The present approach involves the addition of a ceramic foam ring at the downstream surface of a swirl-stabilized LPM combustor dump plane. Previous investigations into porous inert media (PIM) combustion and the technique's ability to control combustion noise have successfully qualified this approach at ambient pressure. Fundamentally, PIM reduces turbulence in the flow field at the inlet of the combustor. During steady operation, reactants enter a combustor through a swirler; radial momentum resulting from the swirl motion partially penetrates the porous ring; this reactant flow is preheated and released from the PIM at its downstream surface; ignition energy is supplied by the thermal radiation and conduction from the vortical jet of reactants that did not penetrate the PIM; the reaction zone in the core region is slightly shifted downstream;

and finally, combustion is sustained without the turbulent structures that excite enclosing structures and induce instabilities.

The present study experimentally investigates the acoustic effects of PIM combustion for a variety of reactant flow rates, equivalence ratios, and most importantly, chamber pressures. A state of the art high-pressure combustion laboratory is utilized for conducting the experiments. A high-pressure combustion apparatus allows experiments to be conducted with high volumetric flow rates ($Q \geq 300$ LPM) and high chamber pressures ($P \leq 4$ atm). The experimental setup allows noise measurements to be collected safely and remotely from behind a bulletproof glass shield.

3.2 Experimental Setup

The experimental apparatus described in chapter 2 is shown schematically in Figure 3.1. A compressor and dryer supplied dry air at 200 psi at discharge- ~ 140 psi after losses within the piping network. A pressure regulator was used to adjust the supply pressure, thus maximum air mass flow rate. The air supply was split into two lines: a combustion airline and a cooling airline. In each test case, combustion air was mixed with fuel, and then the mixture was combusted. The cooling air did not participate in reactions but flowed around the combustor to maintain the apparatus at safe temperatures. Combustion and cooling air flow rates were dictated by the supply pressure and the downstream sonic nozzles. Sonic nozzles were designed such that combustion and cooling air flow rates are $2/3$ and $1/3$ of the total air mass flow rate, respectively; globe valves on each air line offered the ability to adjust this ratio. Downstream of each globe valve and through identical laminar flow elements (LFEs) calibrated for 0 to 1400 lpm, pressure drop and static pressure were measured using differential and absolute pressure

transducers, respectively. K-type thermocouples were used to measure the temperature of air passing across LFEs. Volumetric flow rates calculated from the LFE differential pressure measurements are corrected for temperature and pressure as specified by the manufacturer (see APPENDIX C).

Cooling air was routed directly to the experimental apparatus where it is injected at four points surrounding and parallel to the combustion chamber located within a pressurized vessel. Combustion air was first routed through a 72 KW electrical heater (Osram Sylvania model number 073377). The preheater was used to preheat the air prior to mixing with fuel and entering the combustion chamber. Pipe downstream of the electrical heater was well insulated to minimize the heat loss. Fuel was injected at a location 61 cm (24 inches) upstream of the combustor dump plane, within a 60 cm (24 inches) long, 2.5 cm (1 inch) schedule 80 stainless steel premixer pipe with ID = 2.44 cm (0.96 inches) and OD = 3.35 cm (1.32 inches). Finally, the mixture of reactants was axially injected into a cylindrical quartz combustion chamber.

An external fueling station located outside of the combustion laboratory supplied natural gas fuel. City natural gas (NG) was compressed to 3000 psi and stored in a rack of ten 50-liter tanks. Next, NG was supplied to the experimental apparatus from the ten interconnected pressurized tanks. A pressure regulator, typically set to 100 psi, was used to control fuel supply pressure. The fuel flow rate was controlled using a Bronkhorst mass flow controller calibrated for 0 to 465 normal liters per minute (nlpm). A solenoid valve with an electrical cutoff switch was placed inline near the injection point as a necessary safety feature. Finally, the fuel was injected into the premixer section.

The dump plane was positioned at the downstream end of the premixer section. As shown in Figure 5.2, a helical swirler, of which the location may be axially varied, is located just upstream of the dump plane. The porous insert was supported on the downstream surface of the dump plane by the combustion chamber sidewalls. A slight step in the combustor I.D., located at the downstream end of the PIM insert, acted in preventing the insert from being displaced downstream. Once the reactant mixture entered the combustion chamber through the swirl injector, a 400 kV electrical discharge was used to ignite the mixture.

The quartz combustion chamber, as seen in Figure 3.3, was mounted, with or without PIM, inside of a pressurized barrier. The chamber pressure was elevated by modulating the pressure within the high-pressure vessel that enclosed the chamber. A stationary nozzle and a traversing needle were used in conjunction as a pressure throttling mechanism at the downstream end of the high-pressure vessel, by fundamentally acting as a variable sonic throat. The pressure throttle mechanism was electronically controlled from a dedicated laboratory workstation, allowing the combustion chamber pressure to be remotely modulated during system operation.

A dynamic pressure transducer, described in detail in Chapter 2, measures the combustion noise within the high-pressure enclosure. Also describe in Chapter 2, a condenser microphone was used to measure jet noise near the exit of the exhaust nozzle and throttle. The jet noise results were found to be inconclusive; therefore, they are not included in the proceeding discussion. However, jet noise figures, corresponding to the proceeding cases at high pressure, are displayed in APPENDIX F.

3.3 Results and Discussion

Previous atmospheric investigations, mentioned in Chapter 1, have revealed the ability to reduce combustion noise and suppress instabilities with the use of porous inserts in the reaction zone of swirl-stabilized, LPM combustors by eliminating highly turbulent regions and sustaining flamelets at the downstream surface of PIM. In the present study, the technique of PIM noise mitigation is tested for more realistic gas turbine operating conditions. The experimental parameters include operating pressure, reactant flow rate, and reactant mixture equivalence ratio. Experiments were conducted with combustion air flow rates (Q) of 300 LPM, 400 LPM, and 600 LPM; operating pressures (P) of 0.101 MPa, 0.203 MPa, 0.304 MPa, and 0.405 MPa; equivalence ratios (ϕ) of 0.55, 0.65, and 0.75; and reactant inlet temperature (T_{inlet}) of 20 °C. The PIM insert, as seen in Figure 3.4, is characterized by length, i.d., o.d., and pore density. Based on the results of previous studies targeting the effect of PIM properties on combustion noise, a porous ring with a diffusing cross-section and a pore density of 26 ppcm was chosen for all cases.

3.3.1 Suppression of Thermo-acoustic Instabilities when using a Steel Combustor

Sound pressure measurements reveal the ability of PIM to suppress combustion instabilities at different operating conditions, specifically with elevated pressure, by capturing the near field acoustic responses within the high-pressure enclosure that was described in Chapter 2. First, sound pressure measurements are compared for experiments conducted with a steel combustion chamber enclosing and supporting the porous insert. Table 3.1 summarizes overall sound pressure levels recorded for operating conditions with $Q = 400$ LPM. A nomenclature, characterizing the operating pressure

and mixture equivalence ratio, is used to easily refer to each comparison with a given flow rate. For example, a case with $P = 0.203$ MPa and $\phi = 0.65$ is described, within discussion on a given flow rate, as case P2-65. Likewise, case P4-55 refers to a experiments with operating pressure, $P = 0.405$ MPa, and equivalence ratio, $\phi = 0.55$.

Table 3-1

Overall Sound Pressure Levels for Steel Combustor Tests with $Q = 400$ LPM and $T_i = 20^\circ\text{C}$

| Case | HRR (kW) | Without PIM, dB (dBA) | With PIM, dB (dBA) |
|-------|----------|-----------------------|--------------------|
| P1-55 | 12.5 | 129.6 (127.5) | 125.6 (125.1) |
| P1-65 | 14.7 | 130.8 (129.2) | 130.2 (127.5) |
| P1-75 | 17.0 | 132.5 (132.3) | 132.1 (130.4) |
| P2-55 | 24.9 | 136.0 (135.1) | 132.8 (127.3) |
| P2-65 | 29.4 | 146.9 (138.6) | 144.6 (126.2) |
| P2-75 | 34.0 | 159.3 (138.6) | 152.7 (125.5) |
| P3-55 | 37.4 | 142.2 (138.6) | 136.0 (125.1) |
| P3-65 | 44.2 | 153.8 (144.7) | 153.6 (132.5) |
| P3-75 | 51.0 | 153.0 (144.6) | 151.8 (132.3) |
| P4-55 | 49.8 | 134.2 (128.9) | 130.0 (119.0) |
| P4-65 | 58.9 | 147.8 (144.6) | 144.3 (131.7) |
| P4-75 | 67.9 | 153.4 (144.8) | 152.2 (131.9) |

Based on the data presented in table 3-1 alone, PIM is capable of reducing overall sound pressure levels, particularly as perceived by humans. The A-weighted sound pressure levels, displayed in units of dBA, reveal reductions as large as 13 dBA. Over the full range of conditions for cases with $Q = 400$ LPM, the use of PIM reduces A-weighted sound pressure by an average of 9.4 dBA; however, the data are skewed toward

the cases of elevated pressure. Neglecting the cases of atmospheric pressure, the use of PIM reduces human perceived noise levels by an average of 12 dBA. To determine the detailed acoustic effects of PIM combustion with $Q = 400$ LPM, acoustic power is analyzed across a broad frequency range ($100 \text{ Hz} \leq f \leq 1600 \text{ Hz}$).

(a) Effect of Equivalence Ratio on PIM Performance

Pressure, $P = 4 \text{ atm}$

Spectral SPL data are first discussed for high-pressure experiments in which instabilities are certainly large in magnitude and consistent in behavior. Figure 3.5 presents both full and $1/3^{\text{rd}}$ octave acoustic power spectra, without and with PIM insert, for cases with $P = 0.405 \text{ MPa}$ and $Q = 400 \text{ LPM}$. For case P4-55 ($\phi = 0.55$), the full power spectra without foam insert, as seen in Figure 3.5 (a), reveal noise across most of the frequency range and a potentially harmonic excitation of peak value, 107 dB, at 988 Hz. With the PIM inserted, the broadband noise is reduced by 5 dB – 15 dB and the peak SPL at 988 Hz, reduced by 11 dB. No resonance was audible by the operator while running case P4-55; however, this case is still useful for demonstrating the ability to mitigate direct combustion noise across a broad range of frequencies.

The acoustic power spectra for a higher equivalence ratio (case P4-65), seen in Figure 3.5 (b), reveal harmonic excitations of 124 dB and 120 dB at frequencies, 643 Hz and 1287 Hz, respectively. With the PIM inserted, the 643 Hz instability is reduced to 105 dB and the 1287 Hz instability, to 101 dB. In terms of $1/3^{\text{rd}}$ octave bands, displayed on the right side of Figure 3.5, the PIM is effective at reducing the SPLs at center frequencies of 630 Hz and 1250 Hz by more than 10 dB. Figure 3.5 (c) presents acoustic power spectra for case P4-75. The full power spectra for case P4-75, without foam

insert, expose harmonic instabilities similar in nature to those of the previous case. Peak SPLs of 133 dB and 134 dB occur near the frequencies pointed out for the previous case. At 736 Hz, the 133 dB peak is reduced to 98 dB with PIM, and the peak amplitude occurring at 1352 Hz reduces from 134 dB to 100 dB. The 1/3rd octave band SPLs, displayed on the right side of Figure 3.5 (c), help to illustrate the effect of PIM on instability. Collectively, the 1/3rd octave plots that are featured in Figure 3.5 help to illustrate the reduction of noise levels with PIM inserted.

Pressure $P = 3 \text{ atm}$

Next, spectral acoustic power measurements for cases with $P = 0.304 \text{ MPa}$ and $Q = 400 \text{ LPM}$ are discussed. First consider the case with $\phi = 0.75$ (P3-75). Spectral measurements for case P3-75, displayed in Figure 3.6(c), reveal dominant peaks of 132 dB and 141 dB, at 670 Hz and 1339 Hz, respectively. With foam insert, these peak levels are successfully reduced to 112 dB and 105 dB, respectively, with a 50 Hz phase shift. The corresponding 1/3rd octave band plot indicates instabilities, without PIM inserted, centered around 300 Hz, 630 Hz, and 1250 Hz. Again, PIM is effective at reducing the peak levels at the 630 Hz and 1250 Hz center frequencies, by 17 dB and 26 dB, respectively. Next, for case P3-65 ($\phi = 0.65$), Figure 3.6(b) shows several distinct peaks in the full sound power spectra without PIM; most of these peaks are reduced to background level with foam inserted. For example, with PIM, peak SPL values of 132 dB, 124 dB, and 131 dB – respectively occurring at 636 Hz, 1012 Hz, and 1274 Hz – are correspondingly suppressed to 113 dB, 101 dB, and 88 dB, with foam inserted. Likewise, band discretized SPL values about center frequencies, 630 Hz and 1250 Hz are reduced by 15 dB and 25 dB, respectively, by utilizing the PIM. Furthermore, sound

power spectra for the leanest mixture ($\phi = 0.55$), seen in Figure 3.6(a), show PIM suppressing instability peaks and broadband noise by a margin of 15 dB to 20 dB, with respect to background levels.

Pressure, $P = 2 \text{ atm}$

Figure 3.7 displays full and $1/3^{\text{rd}}$ octave band acoustic power spectra for cases with operating pressure, $P = 0.203 \text{ MPa}$. Again, first consider the case with $\phi = 0.75$. For case P2-75, power spectra in Figure 3.7 (c) reveal several peak values of 120 dB, or less. Four dominant peaks exist around frequencies, 150 Hz, 650 Hz, 1000 Hz, and 1250 Hz. At 642 Hz, the SPL is reduced from 129 dB, occurring without PIM, to 90 dB when foam is inserted. Similarly, the PIM reduces SPL from 122 dB to 85 dB, at 995 Hz, and from 135 dB to 86 dB, at 1284 Hz. Also, in Figure 3.6(c), a SPL of about 140 dB is measured across the frequency range between 100 Hz – 150 Hz; this is likely indirect noise resulting from thermo-fluid interactions between the cooling air and combustion products becoming important at the lower operating pressure.

Next, sound power spectra in Figure 3.7(b), for $\phi = 0.65$, reveal three distinct peaks at levels of 131 dB, 117 dB, and 122 dB. The full acoustic power spectra for case P2-65, with foam insert, confirms peak levels reducing from 131 dB to 88 dB, at 596 Hz, 117 dB to 86 dB, at 967 Hz; and 122 dB to 85 dB, at 1192 Hz. Notice that the $1/3^{\text{rd}}$ octave band SPLs, for combustion with PIM, are nearly a constant value across the entire band of frequencies. The SPL at the center frequency of 630 Hz band is damped from 143 dB without PIM to 117 dB with it, representing a 26 dB reduction. These results show that combustion with PIM has consistently suppressed combustion instabilities and noise encountered at high operating pressures.

Pressure $P = 1 \text{ atm}$

The porous insert has been proven to consistently suppress combustion instabilities and mitigate combustion noise for unstable operating conditions, including operating pressures from 0.203 MPa (2 atm) to 0.405 MPa (4 atm). Lastly, sound power spectra, for atmospheric pressure experiments, $P = 0.101 \text{ MPa}$ (1 atm), are shown in Figure 3.8. Relatively low amplitude instabilities are clearly present in Figure 3.8(a); however, the previous trends of instability seen around 600 Hz, 1000 Hz, and 1250 Hz are not present. With PIM, the noise levels are slightly higher within the range of 600 HZ to 1200 Hz; this trend repeats for different equivalence ratio cases presented in Figure 3.8. This result is likely caused by indirect noise contributions by the cooling air flow at the low pressure. Photographic flame images, both with and without PIM, are displayed in Figure 3.9. Notice that the flame with PIM stabilizes downstream in comparison to the swirl-stabilized flame, particularly at the low pressure. This shift in flame location can affect the indirect noise generated by interaction of the cooling air flow and combustion products. Also, recall that the sound probe is flush mounted with the inner wall surface of the pressurized enclosure, near the axial location where cooling air and combustion products interact. Further experiments would be necessary to clearly distinguish such indirect noise from direct combustion noise. As a summary of the results, with and without PIM, for the baseline flow rate, $Q = 400 \text{ LPM}$, Figure 3.10 shows total SPL vs. pressure.

(b) Effect of Flow Rate on PIM Performance

Next, the effect of the reactant flow rate on PIM performance is considered for combustion without and with PIM inserted. Table 3-2 summarizes total SPLs for all

cases with $Q = 300$ LPM and $T_{inlet} = 20$ °C. Notice that, for a given operating pressure, the sound levels, occurring when the porous insert is present, are equivalent; this was not revealed in cases with $Q = 400$ LPM. The effect of equivalence ratio on total SPL, for the cases without porous insert, is consistent with that of the cases with flow rate, $Q = 400$ LPM; refer back to Table3-1.

Table 3-2

Overall Sound Pressure Levels for Steel Combustor Tests with $Q = 300$ LPM and $T_i = 20$ °C

| Case | HRR (kW) | Without PIM, dB (dBA) | With PIM, dB (dBA) |
|-------|----------|-----------------------|--------------------|
| P1-65 | 11.0 | 124.2 (122.7) | 123.3 (118.6) |
| P1-75 | 33.1 | 125.3 (125.0) | 123.3 (121.1) |
| P3-65 | 12.7 | 126.8 (125.7) | 124.4 (115.6) |
| P3-75 | 38.2 | 130.8 (131.0) | 124.0 (123.0) |

Pressure, $P = 3$ atm

Figure 3.11 shows acoustic power spectra for $Q = 300$ LPM, $P = 0.304$ MPa, $T_{inlet} = 20$ °C, and $\phi = 0.65$ and 0.75 . The sound power spectra for case P3-75, shown in Figure 3.11(c), reveal several small peaks across the full frequency range and a 125 dB peak at 1300 Hz; this 1300 Hz instability is reduced to a peak value of 102 dB when foam is present, resulting in a 23 dB reduction. Similarly, for case P3-65, the plot of SPL across the $1/3^{rd}$ octave bands, displayed on the right side of Figure 3.11(b) shows a 10 dB

reduction in sound level across 1250 Hz band – the band in which the 125 dB peak occurs. Next, noise spectra featured in Figure 3.10(a), display distinct peaks ranging in levels between 100 dB and 105 dB, occurring near 600 Hz, 800 Hz, 1000 Hz, and 1200 Hz. Again, experimental evidence suggest that combustion with PIM is a successful technique for acquiring lower noise emissions (≥ 10 dB) – even for operating conditions that are relatively stable when using the standard swirl stabilization method.

Pressure, $P = 1$ atm

Finally, as shown in Figure 3.12, full and $1/3^{\text{rd}}$ octave band power spectra for operating conditions, $Q = 300$ LPM and $P = 0.101$ MPa (1 atm), display trends similar to those of operating conditions, $Q = 400$ LPM and $P = 0.101$ MPa (1 atm); however, SPL magnitudes are smaller. Three distinctive peaks reveal themselves in the full power spectra, shown in Figure 3.12(a). Among these are a 104 dB peak, at 550 Hz; a 95 dB peak, at 800 Hz; and a 110 dB peak, at 1155 Hz. The foam insert successfully reduces these peaks by 17 dB, 6 dB, and 8 dB, respectively. The $1/3^{\text{rd}}$ octave band power spectra, displayed in Figure 3.12(a) and Figure 3.12(b), reveal minor variations in acoustic power, with respect to equivalence ratio, with or without the use of porous insert. These results indicate, as pointed out in previous low-pressure cases, that the indirect noise from the cooling air flow could become dominant at low pressure. As a summary of the results, with and without PIM, for the flow rate, $Q = 300$ LPM, Figure 3.13 shows total SPL vs. pressure.

In earlier experiments conducted at atmospheric pressure, high amplitude instabilities have been consistently observed only at high reactant flow rates ($Q \geq 600$ LPM). Such instabilities are similar to those reported above for high pressure

experiments, of which are steep and dominate over the indirect noise associated with the cooling air flow. In such high flow rate, low-pressure experiments with significant instabilities, the foam insert was still effective at mitigating combustion instabilities and broadband combustion noise (Smith, 2011; Sequera, 2011).

(c) PIM Durability at High Operating Pressure

Experimental results provide evidence that swirl-stabilized combustion with foam insert is an effective technique to sustain stable combustion over a variety of operating pressures, reactant flow rates, and heat release rates. In previous investigations into the acoustic benefits of PIM combustion, porous materials have proven durability for atmospheric operations; however, as witnessed in the present study using a steel combustor, the structural aspects of porous inert materials still require advancement before implementation in high-pressure combustion applications. Figure 3.14 shows a post-experiment image of the insert used for experiments with conditions including $Q = 300$ LPM and $P = 0.304$ MPa. The porous insert was carefully removed, in several pieces, from the steel combustion chamber, and in the image, all the pieces are resting together, as they were supported by the combustion chamber. The PIM surface shows discoloration that is presumed to reveal surface temperature gradients. The downstream inner edge experiences the primary erosion because the flame tends to anchor within the inner void of the PIM insert, heating and shearing the downstream inner edge. Outer surface discoloration resulted from the high insert surface temperatures that were most likely driven by upstream axial conduction within the encircling sidewall of the steel combustion chamber. Furthermore, the high temperatures of the steel combustion

chamber cause it to expand; thus, so does the insert slightly. Insert fracturing and seizing is the result of the expansion difference between the combustor and the insert.

Figure 3.15 shows a post-experiment image of the insert used for conducting experiments with conditions including $Q = 400$ LPM and $P = 0.405$ MPa. In this case, the porous insert was seized beyond an intact extraction, so images were taken while the PIM was still encased in the combustor. Figure 3.16 shows the PIM upstream surface that mates to the inlet dump plane; and Figure 3.17 shows the PIM downstream surface within the steel combustion chamber. Again, images reveal primary erosion along the downstream inner edge of PIM.

In an attempt to collect data for more operating conditions, without jeopardizing PIM inventory, a custom fused quartz combustor, describe in detail in Chapter 2, was fabricated. It is presumed that the quartz minimizes the heating of PIM outer surface, preheating of reactants within the ceramic matrix, and PIM stress due to thermal expansion.

3.3.2 Suppression of Thermo-acoustic Instabilities when using a Quartz Combustor

Results obtained while using the quartz combustor are first considered for operating conditions duplicate to those of the results discussed in section 3.3.1 – that is, $Q = 400$ LPM; $P = 0.405$ MPa, 0.304 MPa, 0.203 MPa, and 0.101 MPa; and $\phi = 0.55$, 0.65 , and 0.75 . First, table 3-3 presents a summary of overall sound pressure levels obtained for the above conditions, without and with PIM. The custom quartz combustor is designed with length and i.d. equal to that of the steel combustor; however, the natural acoustic response of these combustor are not equivalent.

Without PIM, overall sound pressure levels with the quartz combustor are similar to those obtained while using the steel combustor; however, peak levels here, at operating conditions corresponding to those of steel combustor experiments, do vary by as much as 24 dB. Regardless of the change in acoustic response observed when using the quartz combustor, PIM is still effective in reducing overall sound pressure levels. Over the entire range of operating conditions for the cases with $Q = 400$ LPM, PIM reduces overall sound pressure levels by an average of 9.2 dB and 11.5 dBA – a noticeable difference. Only considering reductions for high pressure cases, average reductions in overall SPL are 7.8 dB and 10.1 dBA; this result suggest that instabilities at low pressure and low reactant flow rate are more prevalent when operating with the quartz combustion chamber. Evidence continues to qualify PIM combustion as an effective technique for producing lower sound pressure levels in turbulent, lean-premixed gas turbine systems and systems alike.

Table 3-3

Overall Sound Pressure Levels for Quartz Combustor Tests with $Q = 400$ LPM and $T_i = 20^\circ\text{C}$

| Case | HRR (kW) | Without PIM, dB (dBA) | With PIM, dB (dBA) |
|-------|----------|-----------------------|--------------------|
| P1-55 | 12.5 | 127.2 (124.5) | 126.8 (122.1) |
| P1-65 | 14.7 | 144.4 (143.4) | 128.8 (125.3) |
| P1-75 | 17.0 | 154.2 (154.8) | 130.1 (128.7) |
| P2-55 | 24.9 | 134.1 (129.8) | 132.0 (126.9) |
| P2-65 | 29.4 | 144.4 (144.4) | 133.5 (131.7) |
| P2-75 | 34.0 | 152.5 (153.0) | 135.3 (133.6) |
| P3-55 | 37.4 | 140.9 (139.2) | 146.0 (135.9) |
| P3-65 | 44.2 | 156.3 (155.4) | 147.1 (140.1) |
| P3-75 | 51.0 | 160.3 (159.2) | 150.7 (150.0) |
| P4-55 | 49.8 | 141.9 (137.6) | 142.6 (138.8) |
| P4-65 | 58.9 | 157.2 (157.5) | 142.0 (142.0) |
| P4-75 | 67.9 | 157.4 (157.5) | 145.6 (143.5) |

(a) Effect of Equivalence Ratio on PIM Performance

Pressure, $P = 4$ atm

Figure 3.18 displays acoustic power in the both the full spectrum and 1/3rd octave bands, for cases with $Q = 400$ LPM and $P = 0.405$ MPa. First, the full spectra SPL is considered for the high equivalence ratio case (P4-75), as seen in Figure 3.18(c). The full spectra results without PIM, shown on the left side of Figure 3.18(c), reveal distinct peak SPLs of 115 dB, at 99 Hz; 143 dB, at 670 Hz; 117 dB, at 1046 Hz; and 147 dB, at 1340 Hz. With PIM, these peak levels are respectively reduced to 99 dB, 109 dB, 112 dB, and 112 dB; however, with PIM, there are a couple peak levels where SPL is greater than it is

without PIM. Notice, peak values of 112 dB, at 1032 Hz, and 123 dB, at 1480 Hz; at these corresponding frequencies, without PIM, the SPLs are 109 dB and 108 dB. SPL in the 1/3rd octave bands, as displayed on the right side of Figure 3.18(c), demonstrate the overall ability of PIM to suppress instabilities for case P4-75. At center frequencies, 250 Hz, 630 Hz, and 1250 Hz, the SPLs are respectively reduced from 136 dB to 127 dB; 145 dB to 130 dB; and 156 dB to 136 dB. These distinct reductions contributed to a reduction of 12 dB in the overall SPL.

Similarly, full acoustic power spectra for the leaner case ($\phi = 0.65$) without PIM, displayed in Figure 3.18(b), reveal distinct peaks of 140 dB, 119 dB, and 146 dB; these peaks occur at frequencies of 647 Hz, 1015 Hz, and 1300 Hz, respectively. With PIM, the 647 Hz instability is reduced to 85 dB; the 1015 Hz instability, to 95 dB; and the 1300 Hz instability, to 101 dB. Notice, the acoustic patterns of cases P4-75 and P4-65 closely resemble with foam inserted. With PIM, peak values of 113 dB and 120 dB occur respectively at the frequencies, 1012 Hz and 1452 Hz; for these corresponding frequencies, without PIM, SPL values are 100 dB and 113 dB. Considering now the sound pressure levels discretized into 1/3rd octave bands, as shown on the right side of Figure 3.15(b), the SPL is 149 dB across the 630 Hz band and to 159 dB across the 1250 Hz band. Sound power of such magnitude, occurring within distinct bands, suggest a strong combustion driven resonance of the experimental system, which must produce a natural harmonic response to excitations occurring at frequencies near 630 Hz and 1250 Hz. With PIM, the resulting SPLs in the 630 Hz and 1250 Hz bands bare 123 dB and 134 dB, respectively; this yields 25 dB reductions that contributed to a 15 dB reduction in the overall SPL.

Sound power spectra for the leanest case ($\phi = 0.55$) without PIM, shown in Figure 3.18(a), reveal harmonic excitations that did not occur while using the steel combustion chamber. Peak values of 122 dB, 117 dB, 108 dB, and 112 dB occur at the respective frequencies: 311 Hz, 603 Hz, 950 Hz, and 1400 Hz. Again, the spectral profile with PIM, also seen in Figure 3.18(a), bears a close resemblance to those previously discussed for cases with PIM. Again, there are concentrated peak sound pressure levels revealed for a case with PIM. These peak levels are 113 dB and 119 dB, and they occur at frequencies of 983 Hz and 1449 Hz, respectively. The total SPLs across the 1/3rd octave bands, as displayed on the right side of Figure 3.18(a), help to explain how these peak levels with PIM contribute to the small reduction in overall SPL for case P4-55 ($\phi = 0.55$). Because PIM combustion produces such consistent sound power spectra for a given operating pressure, a reduction in overall SPL is dependent on the occurrence and reduction of high amplitude instabilities. This study has shown that instabilities are not consistently present when operating near the lean limit; this is most likely due to corner recirculation zones contributing less to unsteady heat release rates within the reaction zone, because the central zone is lengthened. Still, broadband noise is reduced by a small, but noticeable, amount.

Pressure, P = 3 atm

Figure 3.19 displays full and 1/3rd octave acoustic power spectra for the operating pressure, $P = 0.304$ MPa, without and with PIM. The full acoustic power spectra without PIM for $\phi = 0.75$, as seen in Figure 3.19(c), reveal distinct spikes of 143 dB, 118 dB, and 143 dB; these peaks occur at frequencies of 707 Hz, 1038 Hz, and 1346 Hz, respectively. Also, notice a broad peak of 122 dB at a frequency of 332 Hz. The three distinct spikes

are reduced to 91 dB, 96 dB, and 102 dB; as ordered above. The peak level occurring near 350 Hz is reduced to 90 dB at the approximate frequency of 332 Hz. As seen in the previous results gathered from tests with the quartz combustion chamber, there are significant SPL peaks occurring with PIM. For case P3-75 with PIM, sound power spectra, as seen on the left of Figure 3.19(c), show high peaks of 138 dB, occurring at 640 Hz; 116 dB, at 1038 Hz; and 127 dB, at 1346 Hz. At the equivalent frequencies, SPLs without PIM are 130 dB, 107 dB, and 134 dB, respectively. It appears that instabilities may occur with PIM combustion, and for equivalent operating conditions and combustor geometry; such instabilities may follow a similar spectral behavior to those encountered without PIM inserted. However, PIM is still effective at reducing the amplitude of instabilities and may also shift frequencies, at which such instabilities occur, as to reduce the overall SPL.

Sound pressure levels across the $1/3^{\text{rd}}$ octave bands, for case P3-75, are displayed on the right side of Figure 3.19(c). The frequency signature without PIM reveals peak levels of 155 dB and 152 dB - totaled across the 630 Hz and 1250 Hz bands, respectively. The SPL across the 630 Hz band is reduced to 148 dB with PIM combustion. Similarly, the SPL across the 1250 Hz band is reduced to 141 dB with PIM combustion. The greatest reduction across the $1/3^{\text{rd}}$ octave bands – 31 dB – occurs across the 800 Hz band. These reductions result in a 10 dB drop in overall SPL for case P3-75.

Next, the full acoustic power spectra for $\phi = 0.65$ without PIM, as displayed on the left side of Figure 3.19(b), reveal many significant peaks of 120 dB or greater, which suggest harmonic excitations of multiple modes. A spike of 134 dB occurs at 315 Hz; one of 136 dB, at 640 Hz; one of 123 dB, at 1009 Hz; and one of 131 dB, at 1278 Hz.

With PIM, the 315 Hz spike is reduced to 106 dB; the 640 Hz spike, to 91 dB; the 1009 Hz spike, to 97 dB; and the 1278 Hz spike, to 99 dB. Again, with PIM, distinct peaks do present themselves, as seen in Figure 3.19(b); however, these peak values are of lower magnitude relative to those encountered in cases without PIM. Sound pressure levels across the 1/3rd octave bands for case P3-65, as displayed on the right side of Figure 3.19(b), help to illustrate the overall effectiveness of the PIM on combustion instabilities and noise. A significant reduction of 24 dB is noticed across the 500 Hz band. Similarly, a reduction of 15 dB is noticed across the 630 Hz band, and reduction of similar magnitude are noticed across the bands: 800 Hz, 1000 Hz, 1250 Hz, and 1600 Hz. These reductions result in a 9 dB reduction in the overall SPL for case P3-65.

Full power spectra for the leanest case ($\phi = 0.55$) without PIM, as displayed on the left side of Figure 3.19(a), reveal moderate peaks that indicate possible instability. Among these spikes, is a peak of 107 dB, occurring at an approximate frequency of 580 Hz, and a peak of 107 dB, occurring at an approximate frequency of 1239 Hz. These two spikes are consistent with those of the high equivalence ratio cases that were responsible for SPL peak levels across the 500/630 Hz bands and 1250 Hz band; however, for the particular flow rate and operating pressure, the amplitude of these excitations are small relative to the broadband combustion noise that is generated by PIM combustion.

Pressure, P = 2 atm

Now, acoustic power spectra for cases with $Q = 400$ LPM and $P = 0.203$ MPa are discussed. Figure 3.20(c) displays the full frequency SPL for the high equivalence ratio ($\phi = 0.75$) case. Here, without PIM, potential harmonic excitations are revealed with peak levels of 127 dB, at 636 Hz; 124 dB, at 994 Hz; and 139 dB, at 1276 Hz. With PIM

the 636 Hz peak is reduced to 81 dB; the 994 Hz peak, to 83 dB; and the 1276 Hz peak, to 85 dB. The SPL across the 1/3rd octave bands, as displayed on the right side of Figure 3.20(c), suggests that these excitations contribute mainly to the 630 Hz and 1250 Hz bands, as previous results have suggested. PIM combustion is consistently effective at eliminating such harmonic responses. Furthermore, broadband noise is reduced throughout the frequency range.

Figure 3.20(b) shows acoustic power spectra for the leaner case ($\phi = 0.65$). Without PIM, the full frequency power reveals harmonic excitations similar to those discussed for the richest case. Among these excitations, is a peak of 125 dB, occurring at 619 Hz; a peak of 113 dB, at 976 Hz; and a peak of 125 dB, at 1242 Hz. With PIM, the 619 Hz SPL becomes 89 dB; the 976 Hz SPL, 85 dB; and the 1242 Hz SPL, 98 dB. With PIM, the frequency behavior and magnitudes are consistent with highest equivalence ratio case discussed above. Also, the peak amplitudes without PIM are somewhat smaller relative to those of the highest equivalence ratio case. With these two relationships in mind, SPL in the 1/3rd octave bands for case P2-65, as displayed on the right side of Figure 3.20(b), reveal slightly smaller reductions; however, major reductions are still present across the 630 Hz and 1250 Hz bands. The SPL across the 630 Hz band is reduced from 134 dB to 119 dB, and the SPL across the 1250 Hz band, from 144 dB to 128 dB. These reductions are responsible for a 10 dB reduction in the overall SPL for case P2-65.

Figure 3.20(a) displays acoustic power spectra for the leanest case ($\phi = 0.55$) with $Q = 400$ LPM and $P = 0.203$ MPa. The full power spectra, displayed on the left side of Figure 3.20(a), reveal a behavior similar to that of the previous two cases; however,

magnitudes are much less. With PIM, reductions occurring near 150 Hz, 950 Hz, and 1200 Hz are responsible for only a 2 dB (3 dBA) reduction in the total SPL for case P2-55.

Pressure, $P = 1 \text{ atm}$

Lastly, Figure 3.21 displays acoustic power spectra for cases with $Q = 400 \text{ LPM}$ and $P = 0.101 \text{ MPa}$. For the highest equivalence ratio case ($\phi = 0.75$) without PIM, the full power spectra, as shown in Figure 3.21(c), show harmonic excitations of multiple modes. A 119 dB spike occurs at a frequency of 183 Hz; a 107 dB spike, at 300 Hz; a 114 dB spike, at 630 Hz; a 116 dB spike, at 810 Hz; and a 143 dB spike, at 1271 Hz. With PIM, the 183 Hz spike is reduced to 83 dB; the 300 Hz spike is reduced to 94 dB; the 630 Hz spike, to 88 dB; the 810 Hz spike, to 102 dB; and the 1271 Hz spike, to 87 dB. Because spikes are so broadly distributed across the full frequency range, the SPL across the $1/3^{\text{rd}}$ octave bands, as displayed on the right side of Figure 3.21(c), is broadly reduced by 10 dB or greater, with PIM combustion. Particularly, the SPL across the 630 Hz band is reduced from 126 dB to 116 dB. Similarly, the SPL across the 1250 Hz band is reduced from 153 dB to 126 dB, a 27 dB reduction. These reductions, illustrated by the SPL across the $1/3^{\text{rd}}$ octave bands, are responsible for a 24 dB reduction in the overall SPL for case P1-75.

The full power spectra for the leaner case ($\phi = 0.65$) without PIM, as displayed on the left side of Figure 3.21(b), suggest that, relative to the high equivalence ratio case, sound power is shifted and concentrated about more distinct frequency ranges. A peak level of 124 dB occurs at a frequency of 510 Hz; a peak level of 106 dB, at 909 Hz; and a peak level of 126 dB, at 1170 Hz. With PIM, the SPL is reduced to 98 dB, at 510 Hz; 86

dB, at 909 Hz; and 95 dB, at 1170 Hz. SPL across the 1/3rd octave bands, shown on the right side of Figure 3.21(b), help to illustrate the effectiveness of the porous insert in suppressing such concentrated sound power. With PIM, the SPL across the 500 Hz band is reduced from 141 dB to 123 dB, and across the 1250 Hz band, the SPL is reduced from 140 dB to 121 dB. These spectral reductions of nearly 20 dB result in a 16 dB reduction in the overall SPL for case P1-65.

Lastly, full power spectra for the leanest case ($\phi = 0.55$) without PIM, as displayed on the left side of Figure 3.21(a), reveal few distinct spikes. Peaks are relatively low (≤ 100 dB); however, there are three peaks worth discussing. A 108 dB peak occurs at a frequency of 180 Hz; a 110 dB peak, at 300 Hz; and a 102 dB peak, at 1204 Hz. With PIM, similar peaks are observed and are reoccurring for cases with $Q = 400$ LPM and $P = 0.101$ MPa. With PIM, the 180 Hz peak becomes 108 dB – no change; the 300 Hz peak, 104 dB; and the 1204 Hz peak, 83 dB. SPL across the 1/3rd octave bands, as displayed on the right side of Figure 3.21(a), reveal only small reduction across the 500 Hz, 630 Hz, 800 Hz, and 1250 Hz bands. These reductions contribute to a negligible reduction in the overall SPL for case P1-55.

As a summary of the results, with and without PIM, for the baseline flow rate, $Q = 400$ LPM, Figure 3.22 shows total SPL vs. pressure. The technique of PIM combustion is presented to consistently suppress combustion instabilities and mitigate combustion noise for unstable operating conditions, including operating pressures from 0.101 MPa (1 atm) to 0.405 MPa (4 atm). The porous insert consistently reduces overall sound pressure levels by 10 dB or greater – excluding the extremely lean cases ($\phi = 0.55$). Without the use of the insert, it is shown that resonant instability is a major contributor to the overall

SPL. As presented through spectral analysis, PIM exhibits the ability to eliminate such instabilities, along with broadly distributed background noise. In previous investigations into the acoustic benefits of PIM combustion at atmospheric pressure, it has been shown that instabilities are more prevalent for high reactant flow rates, $Q \geq 600$ LPM; thus, results are next considered for additional cases with $Q = 600$ LPM and $P = 0.203$ MPa and 0.304 MPa.

(b) Effect of Reactant Flow Rate on PIM Performance

The effect of reactant flow rate on PIM performance is considered for combustion without and with PIM inserted. Table 3-4 summarizes total SPLs for all cases with $Q = 600$ LPM; $P = 0.203$ MPa and 0.304 MPa; $\phi = 0.55, 0.65,$ and 0.75 ; and $T_{inlet} = 20$ °C.

Table 3-4

Overall Sound Pressure Levels for Quartz Combustor Tests with $Q = 600$ LPM and $T_i = 20$ °C

| Case | HRR (kW) | Without PIM, dB (dBA) | With PIM, dB (dBA) |
|-------|----------|-----------------------|--------------------|
| P2-55 | 37.4 | 139.9 (136.6) | 139.7 (134.7) |
| P2-65 | 44.2 | 150.4 (150.8) | 139.6 (136.4) |
| P2-75 | 51.0 | 154.4 (153.5) | 140.1 (138.5) |
| P3-55 | 56.1 | 160.1 (159.2) | 147.1 (144.6) |
| P3-65 | 66.2 | 155.7 (155.3) | 142.8 (140.4) |
| P3-75 | 76.4 | 156.0 (155.5) | 155.5 (154.0) |

First, notice in Table 3-4 that overall SPLs, without PIM, show the increasing nature of combustion noise, with respect to increasing equivalence ratio; except for case P3-55.

Acoustic power spectra are analyzed to determine how the trends differ from cases with $Q = 400$ LPM and how PIM is effective at reducing the overall SPL of the present cases.

Pressure, $P = 3$ atm

Figure 3.23 displays full and $1/3^{\text{rd}}$ octave acoustic power spectra for cases with $Q = 600$ LPM and $P = 0.304$ MPa. Without PIM, the full acoustic power spectra for case P3-75, as displayed on the left side of Figure 3.23(c), reveal harmonic excitations. Among these excitations, there is a peak of 150 dB, occurring at a frequency of 639 Hz; a peak of 128 dB, at 800 Hz; and a spike of 134 dB, at 1279 Hz. With PIM, the 639 Hz spike is reduced to 145 dB; the 800 Hz spike, to 97 dB; and the 1279 Hz spike, to 129 dB. The occurrence of such high amplitude harmonic excitations with PIM combustion suggests that small-scale turbulence, due to increased axial velocity, may create unsteady recirculation zones on the downstream surface of the porous ring, thus geometric optimization may be necessary. In other words, more of the reactant flow may be crossing the porous ring through the center void, then expanding at the downstream end of the insert to form compact recirculation zones that are similar to those formed across the standard dump plane when the insert is not present.

SPL across the $1/3^{\text{rd}}$ octave bands for case P3-75, as displayed on the right side of Figure 3.19(c), help to demonstrate consistent reductions across the entire frequency range despite the occurrence of instability in the PIM case; however, this broad effectiveness results in a negligible reduction in the total SPL for case P3-75.

Next, the leaner case ($\phi = 0.65$) is considered. The full acoustic power spectra for case P3-65 without PIM, as displayed on the left side of Figure 3.23(b), reveal harmonic excitations similar to those of the previous case. A spike of 140 dB occurs at a frequency

of 676 Hz; a spike of 129 dB, at 727 Hz; a spike of 122 dB, at 1095 Hz; and a spike of 127 dB, at 1347 Hz. With PIM, the 676 Hz spike is reduced to 87 dB; the 727 Hz spike, to 95 dB; the 1095 Hz spike, to 94 dB; and the 1347 Hz spike, to 96 dB. For this case with PIM, no harmonic excitations are clearly indicated. The SPL across the 1/3rd octave bands, as displayed on the right side of Figure 3.23(b), help to demonstrate the overall performance of the PIM in eliminating such harmonic disturbances. Major reductions occur across the 630 Hz and 800 Hz bands. Across the 630 Hz band, the SPL is reduced from 152 dB to 130 dB. Similarly, with the use of porous insert, the SPL across the 800 Hz band is reduced from 144 dB to 124 dB. These major reductions of 20 dB, along with reductions in the broadly distributed background noise, contribute to a 13 dB reduction in the overall SPL for case P3-65.

Full acoustic power spectra for the leanest case ($\phi = 0.55$) without PIM, as displayed on the left side of Figure 3.23(a), reveal peaks of 147 dB, 126 dB, and 134 dB; these spikes occur at frequencies of 637 Hz, 801 Hz, and 1273 Hz, respectively. With PIM, a spike of 123 dB occurs at a frequency of 313 Hz; a spike of 129 dB, at 601 Hz – near 637 Hz; a spike of 110 dB, at 953 Hz; and a spike of 120 dB, at 1224 Hz – near 1273 Hz. SPL across the 1/3rd octave bands for case P3-55, as displayed on the right side of Figure 3.23(a), help to illustrate the overall effects of reduced spikes and phase shifting that occur with PIM. With the use PIM, the SPL across the 630 Hz band is reduced from 159 dB to 143 dB, and across the 800 Hz band, the SPL is reduced from 145 dB to 122 dB. Furthermore, the SPL is reduced by 9 dB or greater across the 1000 Hz, 1250 Hz, and 1600 Hz bands. These reductions are responsible for a 13 dB reduction in the total SPL for case P3-55.

Pressure, $P = 2 \text{ atm}$

Figure 3.24 displays full and $1/3^{\text{rd}}$ octave acoustic power spectra for cases with $Q = 600 \text{ LPM}$ and $P = 0.203 \text{ MPa}$. The full acoustic power spectra for the richest case ($\phi = 0.75$) without PIM, as displayed on the left side of Figure 3.24(c), reveal harmonic excitations of multiple modes. A spike of 142 dB occurs at a frequency of 634 Hz; a spike of 127 dB, at 831 Hz; a spike of 125 dB, at 1017 Hz; and a spike of 136 dB, at 1266 Hz. With PIM, the 634 Hz spike is reduced to 88 dB; the 831 Hz spike, to 89 dB; the 1017 Hz spike, to 125 dB; and the 1266 Hz spike, to 100 dB. Furthermore, with PIM, additional spikes of 113 dB and 120 dB occur at frequencies of 306 Hz and 1377 Hz, respectively. Without PIM, the SPLs occurring at 306 Hz and 1377 Hz are 92 dB and 105 dB, respectively. In summary of the full acoustic power spectra for case P2-75, PIM is effective at mitigating the steep, high amplitude spikes that occur without PIM; however, PIM does generate some relatively small amplitude spikes that do not occur without PIM.

To better understand the overall effectiveness of PIM in the present case, the acoustic power is considered across the $1/3^{\text{rd}}$ octave bands, as displayed on the right side of Figure 3.24(c). The SPLs across the $1/3^{\text{rd}}$ octave bands reveal good performance of PIM combustion across the full frequency range. Particularly, the SPL across the 630 Hz band is reduced from 149 dB to 121 dB. Similarly, the SPL across the 800 Hz band is reduced from 141 dB to 119 dB. Furthermore, the SPL is reduced by 9 dB or greater across the 1000 Hz, 1250 Hz, and 1600 Hz bands. These reductions contribute to a 14 dB reduction in the total SPL for case P2-75.

Next, the full and $1/3^{\text{rd}}$ octave acoustic power spectra are considered for the leaner case ($\phi = 0.65$). The acoustic power across the full frequency range for case P2-65

without PIM, as displayed on the left side of Figure 3.24(b), expose harmonic excitations at frequencies traditionally seen for cases with $\phi = 0.65$. Three significant acoustic spikes that are concentrated about three equally spaced frequencies indicate the resonant behavior. A spike of 126 dB occurs at a frequency of 649 Hz; a spike of 118 dB, at 999 Hz; and a spike of 135 dB, at 1299 Hz. With PIM, these acoustic spikes are eliminated. The 649 Hz spike is reduced to 84 dB; the 999 Hz spike, to 92 dB; and the 1299 Hz spike, to 100 dB. Furthermore, with PIM, additional spikes occur that do not occur without PIM. Spikes of 115 dB and 118 dB occur at frequencies of 303 Hz and 1360 Hz, respectively. Without PIM, the SPLs at 303 Hz and 1360 Hz are 102 dB and 105 dB, respectively. Again, to illustrate the overall effectiveness of the porous insert, the SPL is considered across the 1/3rd octave bands.

The acoustic power across the 1/3rd octave bands, for case P2-65, is displayed on the right side of Figure 3.24(b). PIM is again effective at reducing the combustion noise across the broad frequency range beyond 300 Hz. Particularly, the SPL across the 630 Hz band is reduced from 137 dB to 121 dB. Furthermore, the SPL is reduced by 7 dB or greater across the 800 Hz, 1000 Hz, 1250 Hz, and 1600 Hz bands. These reductions contribute to an 11 dB reduction in the total SPL for case P2-65.

Lastly, the leanest case ($\phi = 0.55$) is considered. The full acoustic power spectra for case P2-55 without PIM, as displayed on the left side of Figure 3.24(a), reveal three relatively low amplitude peaks of 111 dB, 108 dB, and 109 dB; these peaks occur at frequencies of 948 Hz, 1202 Hz, and 1399 Hz, respectively. With PIM, the 948 Hz peak is reduced to 90 dB; the 1202 Hz peak, to 84 dB, and the 1399 Hz peak, to 89 dB. Also, as seen for the other equivalence ratios with PIM, additional acoustic spikes occur at

frequencies near 300 Hz, 1150 Hz, and 1350 Hz. Specifically, a 115 dB spike occurs at a frequency of 303 Hz; a 109 dB spike, at 1160 Hz; and a 111 dB spike, at 1345 Hz.

Without PIM, the SPL occurring at 303 Hz is 97 dB; the SPL at 1160 Hz is 84 dB; and that at 1345 Hz is 91 dB. Due to the lack of consistent acoustic resonance with $\phi = 0.55$, the slight reduction in overall SPL for case P2-55 is negligible.

As a summary of the results, with and without PIM, for the flow rate, $Q = 600$ LPM, Figure 3.25 shows total SPL vs. pressure. For a given reactant flow rate and pressure, PIM combustion is seen to produce acoustic responses that are similar in behavior and amplitude. For most cases without PIM, both harmonic excitations and background noise are of much greater magnitude than those witnessed with PIM combustion of equivalent operating conditions.

(c) PIM Durability at High Operating Pressure

Previous moderate flow experiments were conducted using a steel combustion chamber. The porous inserts used for those previous high-pressure experiments showed signs of thermal fatigue. It is speculated that a combination of upstream axial conduction through the steel combustor and pressure sensitive surface temperature elevations are responsible for stressing the PIM insert to a point where it fractures and even breaks down. Furthermore, upstream axial conduction through the steel combustor acts to preheat reactant flow.

A custom quartz combustion chamber, with length and i.d. equivalent to those of the steel combustion chamber, was designed to both prevent upstream axial conduction from preheating the reactant flow and reduce overall surface temperatures along the PIM exterior. The PIM durability showed no signs of deterioration during trail tests

conducted at pressures of 0.101 MPa (1 atm), 0.152 MPa (1.5 atm), and 0.203 MPa (2 atm); however, the porous insert began showing signs of stress during experiments conducted with $Q = 600$ LPM and $P = 0.203$ MPa. Figure 3.26 displays images of the porous insert that was used during experiments with $Q = 400$ LPM and 600 LPM; $P = 0.203$ MPa; and $\phi = 0.55, 0.65,$ and 0.75 . The PIM insert featured in Figure 3.21 shows little sign of erosion; however, the ring is fractured midway along the entire circumference. There was no fusing of the PIM to the quartz wall; the porous insert was easily removed but in two pieces.

A fresh porous insert was used for further experiments with $P = 0.304$ MPa and 0.405 MPa. This insert showed slight signs of erosion along the downstream inner edge after completing experiments with $P = 0.304$ MPa and $Q = 400$ LPM and 600 LPM; however, the insert was intact and utilized for further experiments with $P = 0.405$ MPa. The insert quality was monitored between flow rate adjustments. After completing experiments with $Q = 400$ LPM, the insert was intact, and when experiments were complete for $Q = 600$ LPM, the insert was reexamined. In this case, the PIM was seized to the quartz wall. Several fractures were noted before handling the combustor and PIM. Surface color showed on the outer exterior. The PIM showed signs of interior combustion near the surfaces. The insert did not remain intact through the process of dismounting the combustion chamber.

3.4 Conclusions

The common swirl stabilization method used in LPM combustion systems is manipulated in this study by introducing a ceramic foam insert, intended for combustion instability and noise mitigations, at the dump plane of the combustor. The novel passive

control technique reduces turbulent intensity and heat release fluctuations in reaction zones. The foam insert also serves as an acoustic damper of pressure fluctuations generated in and around the reactions zones. An experimental investigation was performed to determine the effectiveness of PIM combustion by varying the operating pressure, equivalence ratio, and reactant flow rate. Experiments show that instabilities are more prominent at high operating pressures and that the foam insert is effective at mitigating instabilities and suppressing noise over a broad range of operating conditions. The present approach can be easily retrofitted to current swirl-stabilized gas turbine combustion systems; thus, it offers an important opportunity for gas turbine applications. Further testing and geometry optimization may still be necessary to ensure long term durability of the ceramic foam materials employed in this concept.

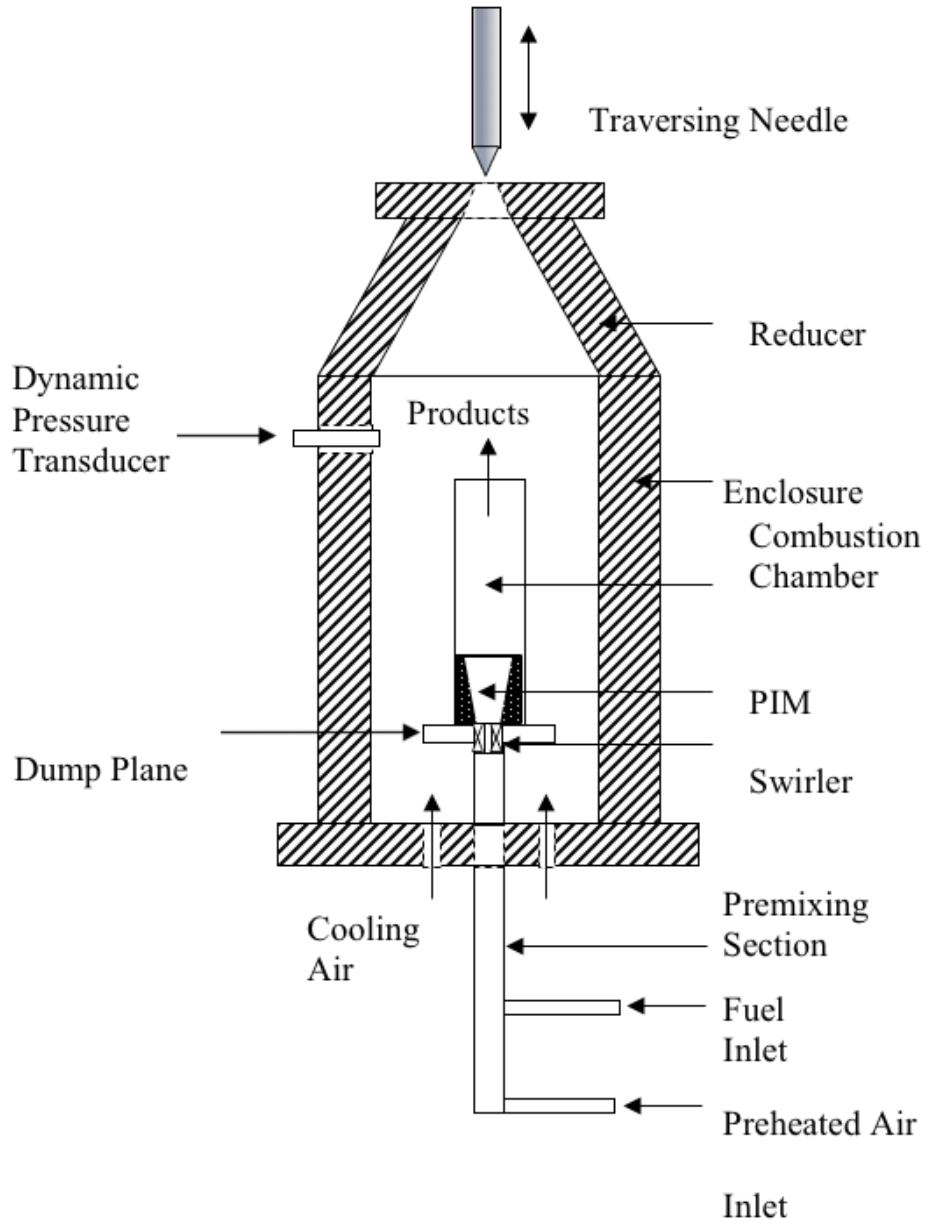


Figure 3.1. Experimental apparatus

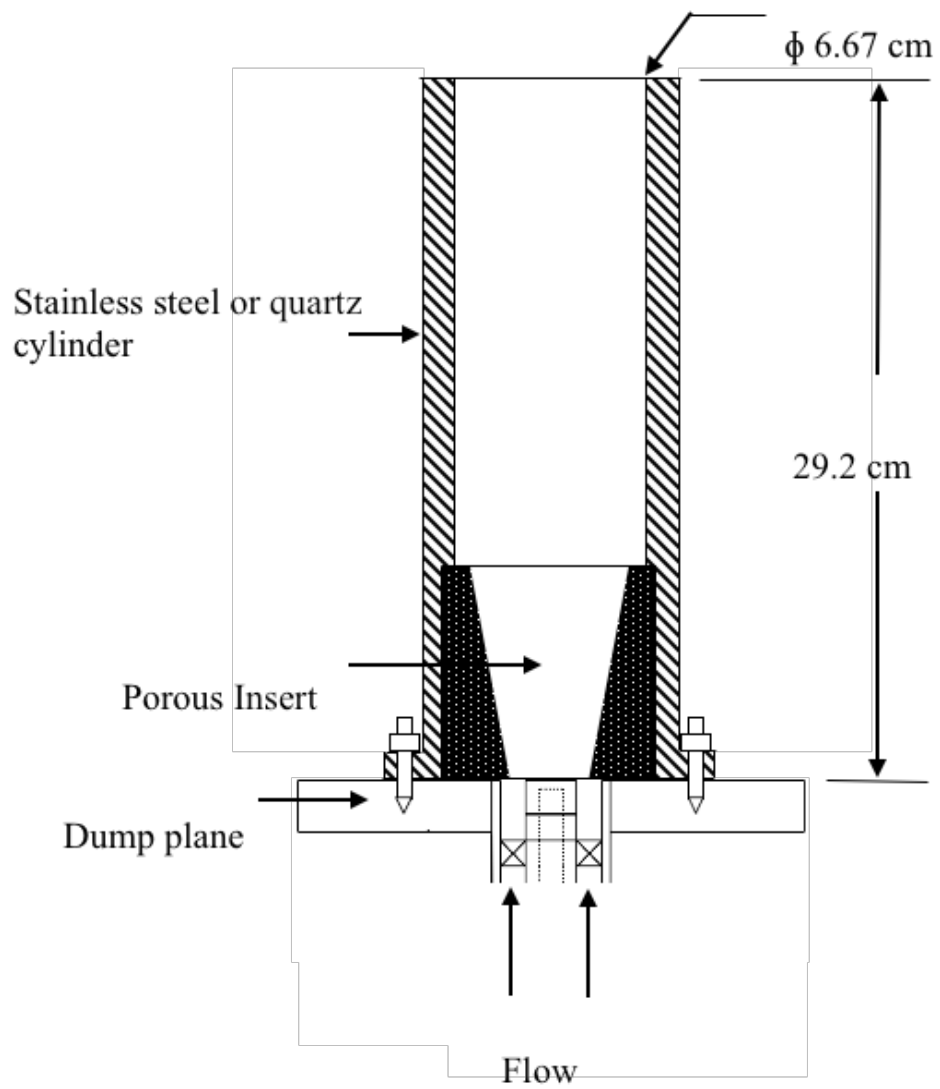
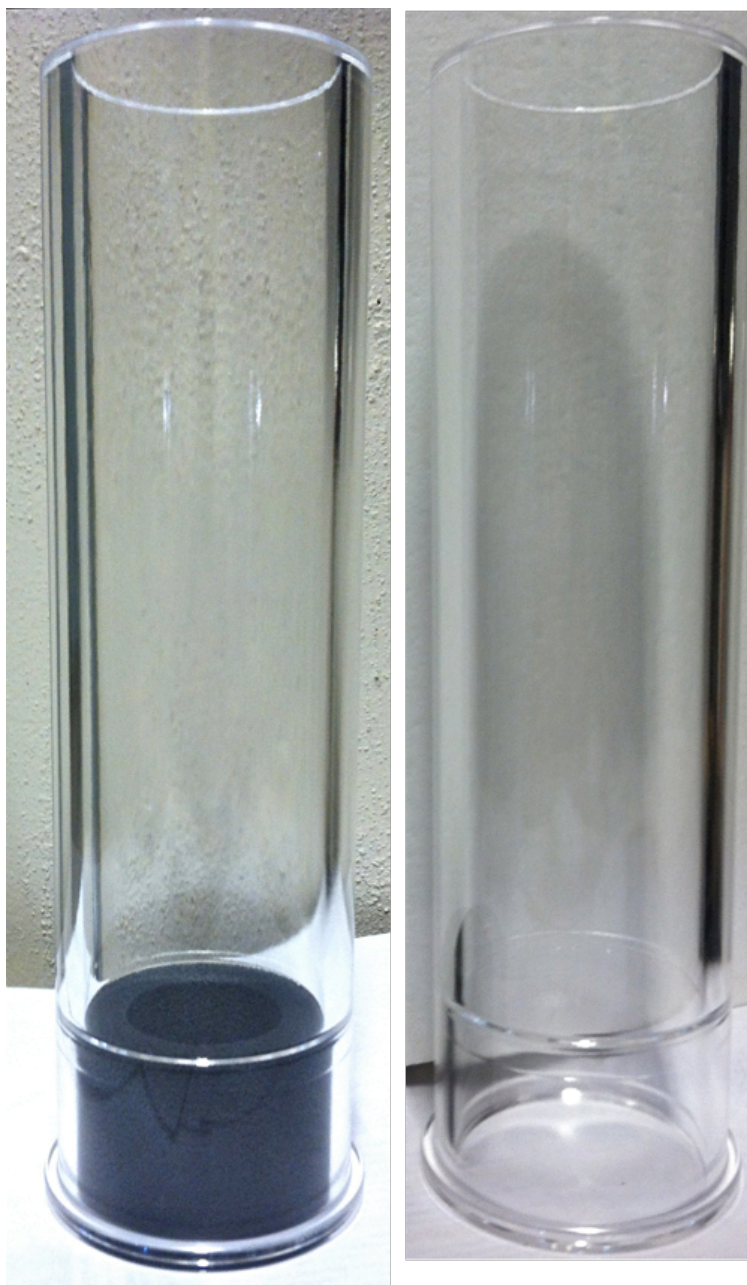


Figure 3.2. Porous insert within a swirl-stabilized combustor



With PIM

Without PIM

Figure 3.3. Photographs of custom quartz combustor with and without PIM

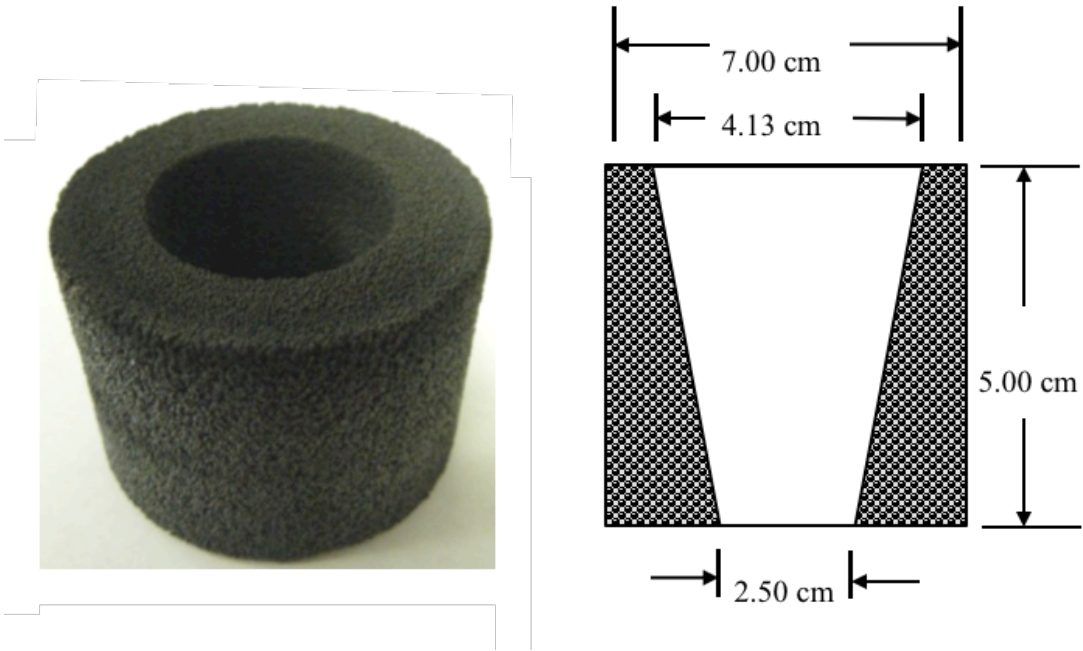


Figure 3.4. Photograph (left) and drawing (right) of porous insert

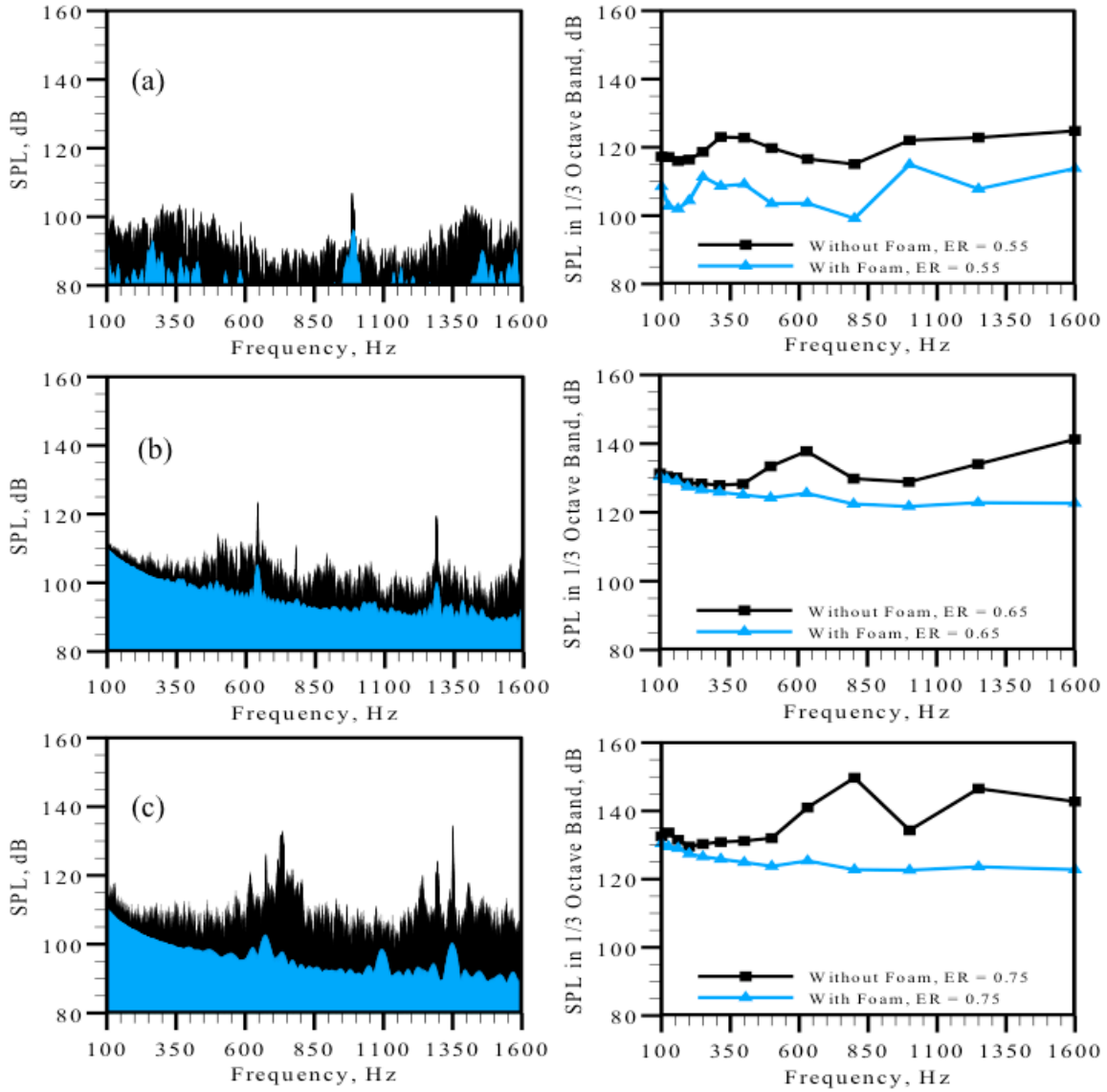


Figure 3.5. Acoustic power spectra and SPL in 1/3rd octave band for P = 0.405 MPa, Q = 400 LPM, (a) $\phi = 0.55$ (case P4-55), (b) $\phi = 0.65$ (case P4-65), and (c) $\phi = 0.75$ (case P4-75)

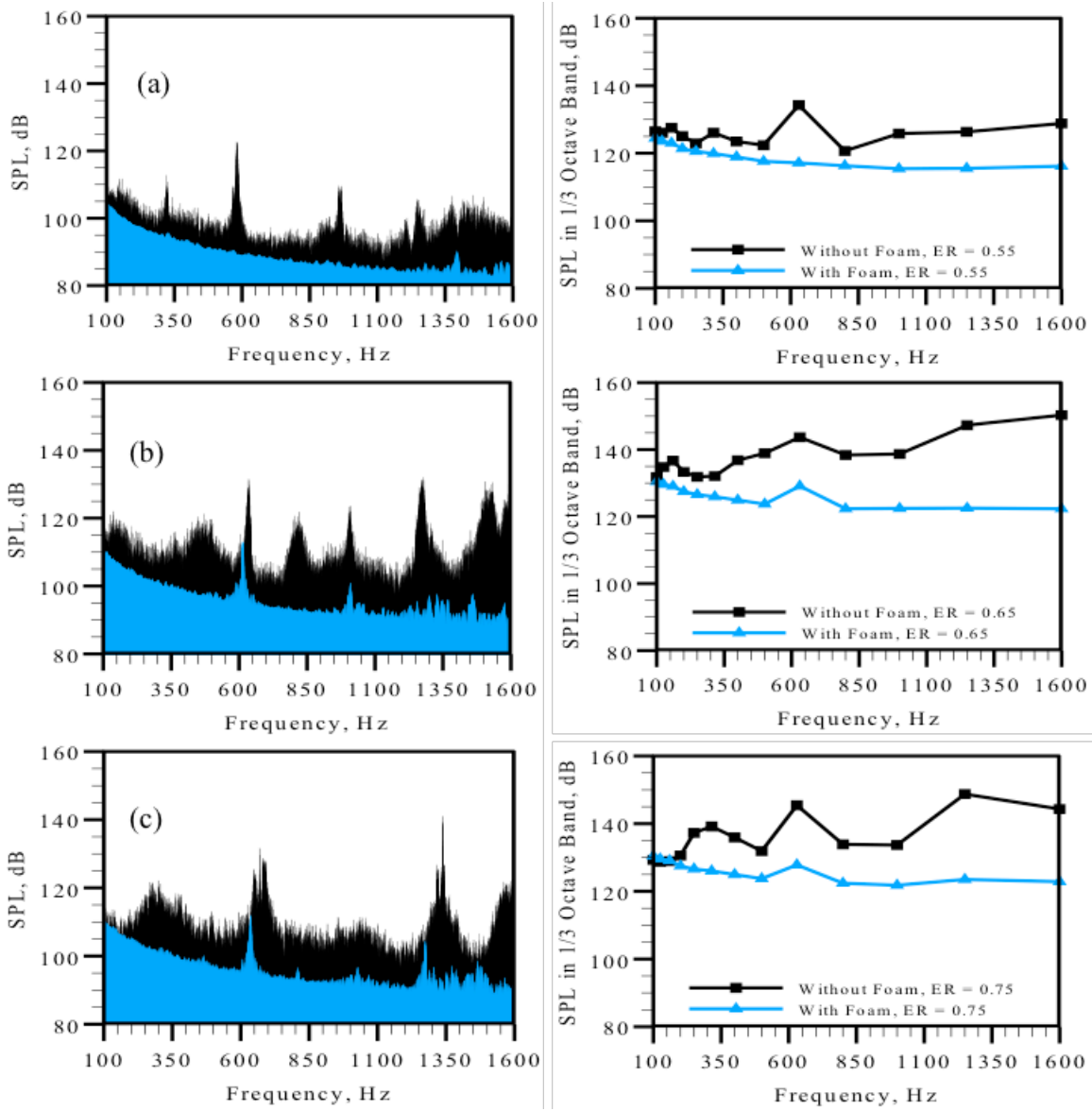


Figure 3.6. Acoustic power spectra and SPL in 1/3rd octave band for $P = 0.304$ MPa, $Q = 400$ LPM, (a) $\phi = 0.55$ (case P3-55), (b) $\phi = 0.65$ (case P3-65), and (c) $\phi = 0.75$ (case P3-75)

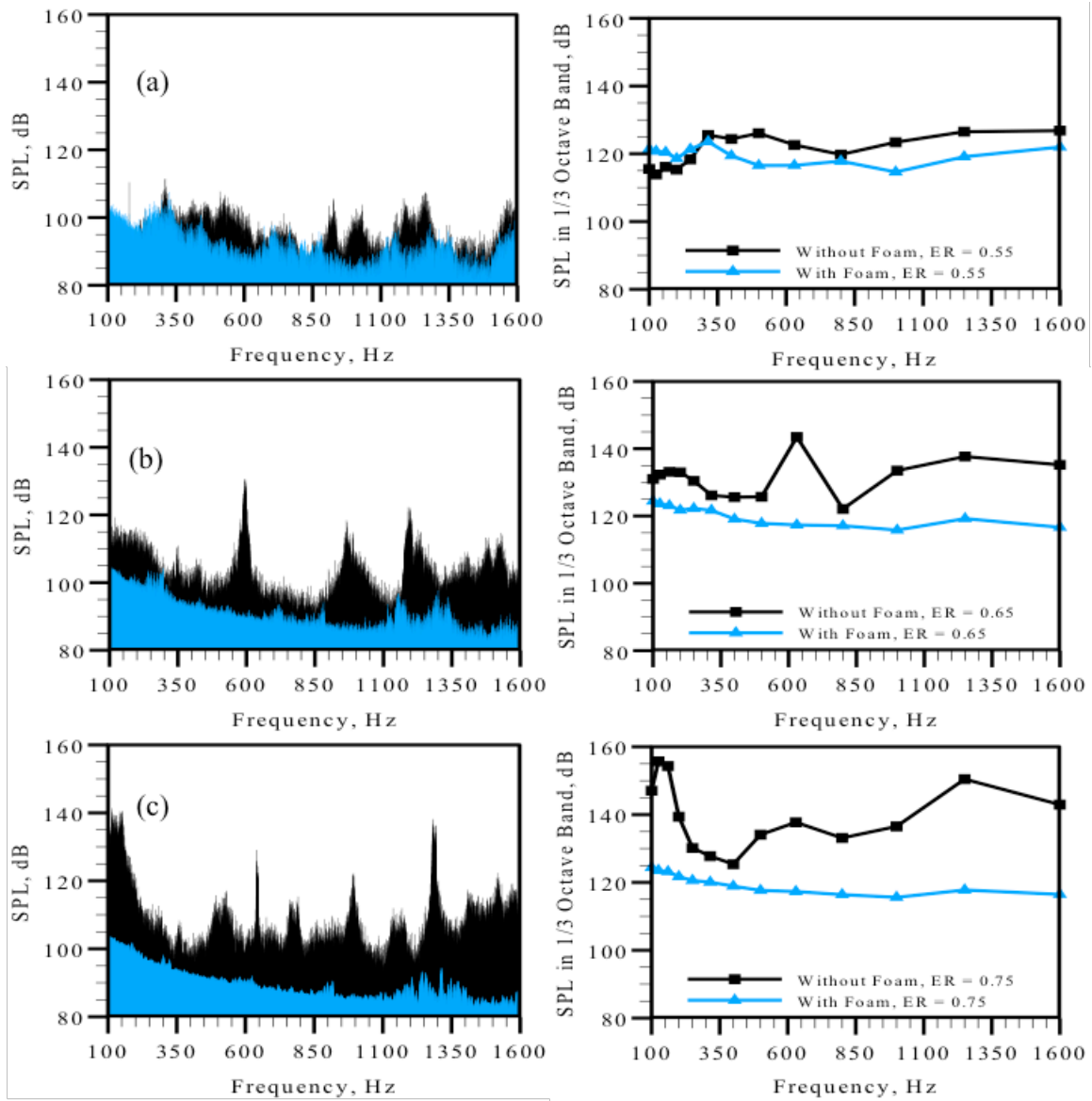


Figure 3.7. Acoustic power spectra and SPL in 1/3rd octave band for P = 0.203 MPa, Q = 400 LPM, (a) $\phi = 0.55$ (case P2-55), (b) $\phi = 0.65$ (case P2-65), and (c) $\phi = 0.75$ (case P2-75)

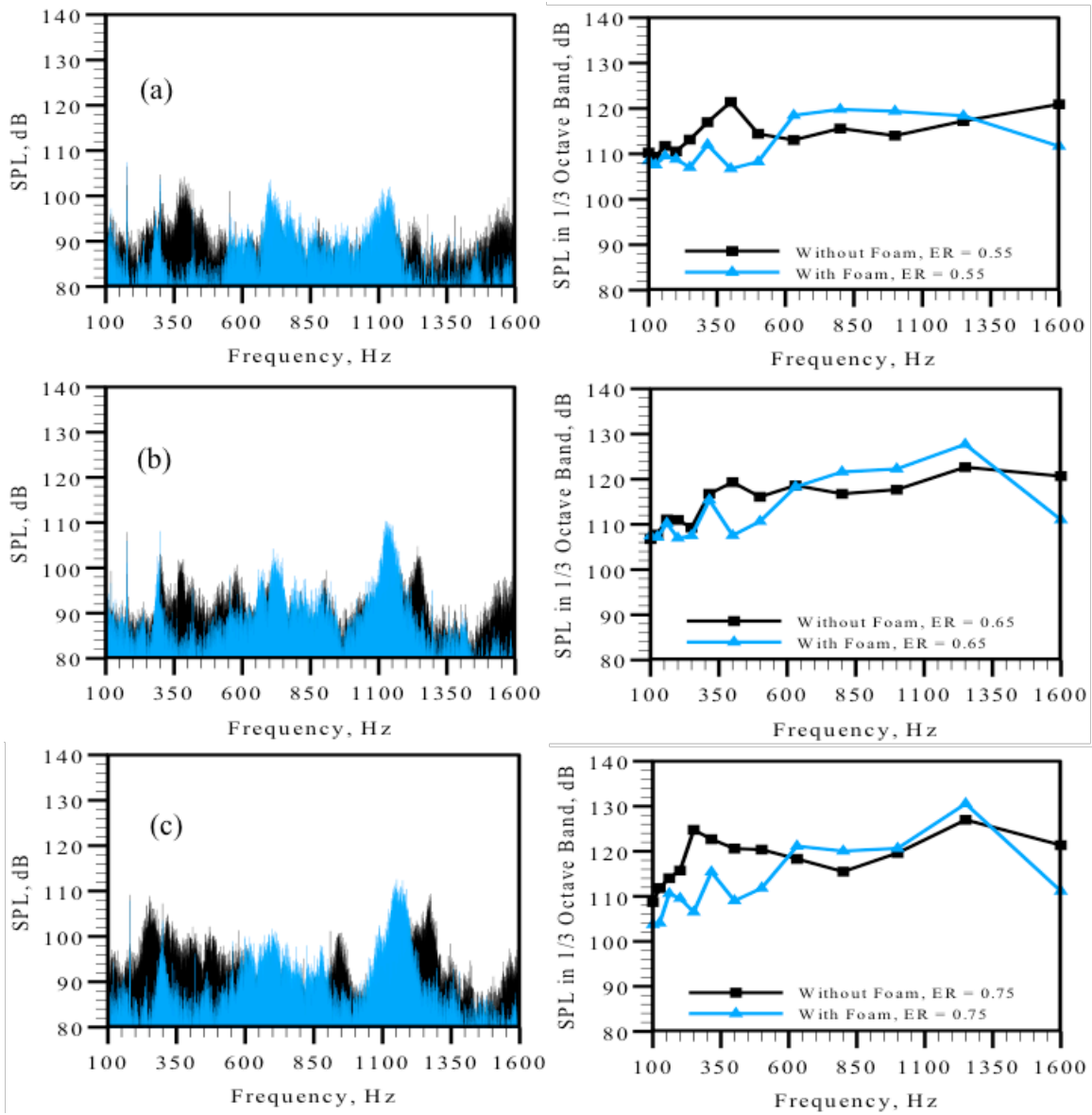


Figure 3.8. Acoustic power spectra and SPL in 1/3rd octave band for P = 0.101 MPa, Q = 400 LPM, (a) $\phi = 0.55$ (case P1-55), (b) $\phi = 0.65$ (case P1-65), and (c) $\phi = 0.75$ (case P1-75)

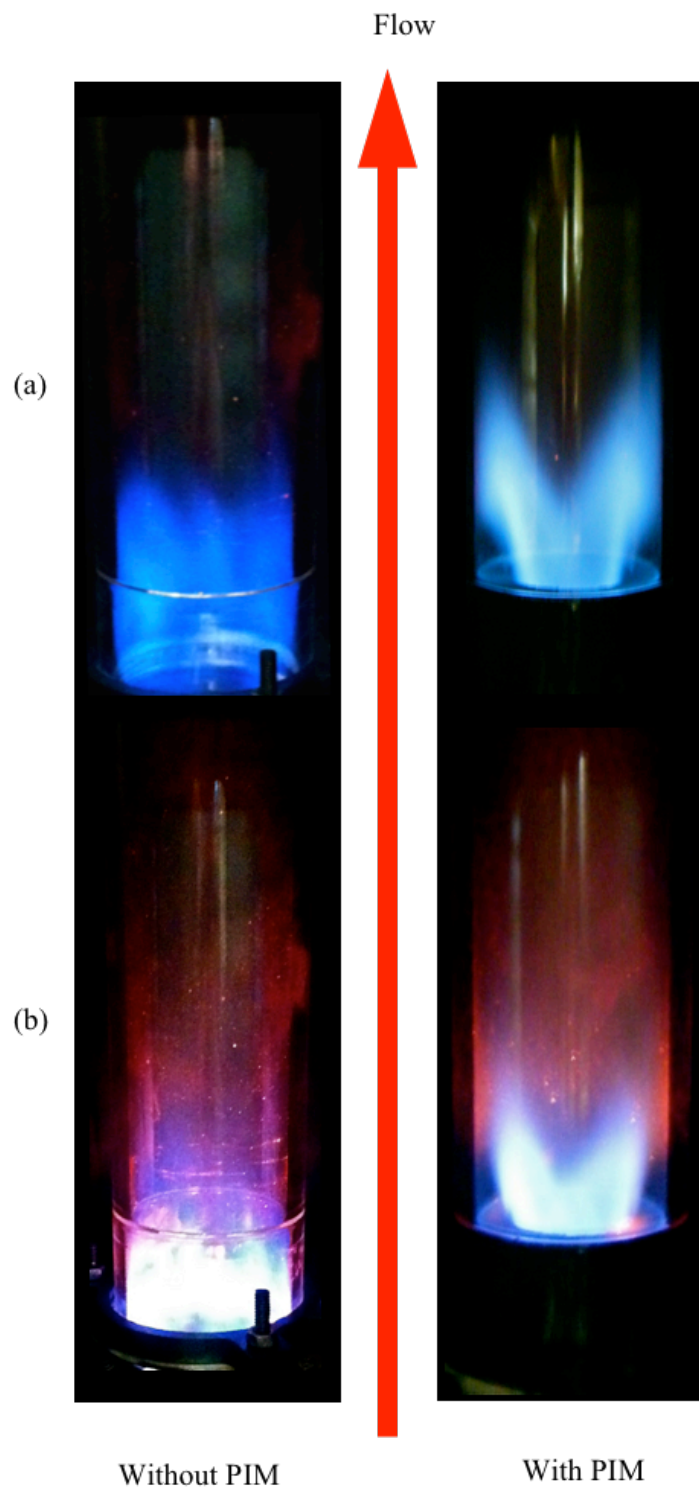


Figure 3.9. Photographs of atmospheric flames for (a) $\phi = 0.65$ and (b) $\phi = 0.75$, both with and without porous insert

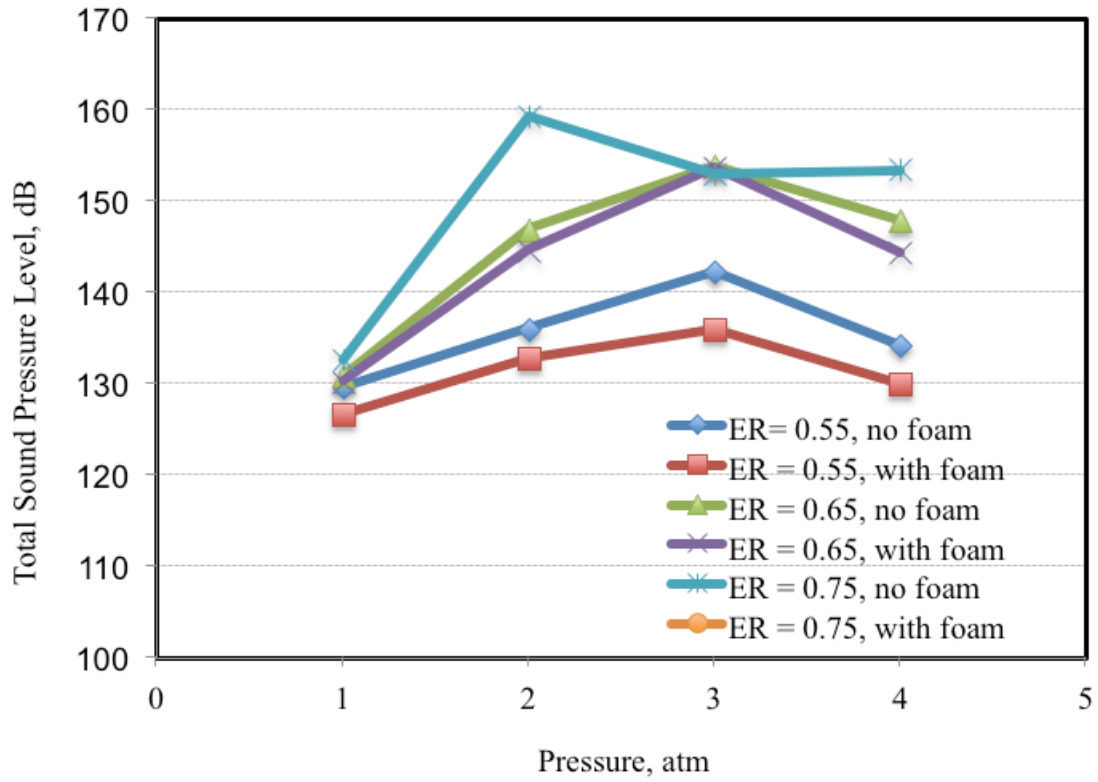


Figure 3.10. Plot of total sound pressure levels, gathered during steel combustor experiments, for cases with baseline flow rate, $Q = 400$ LPM

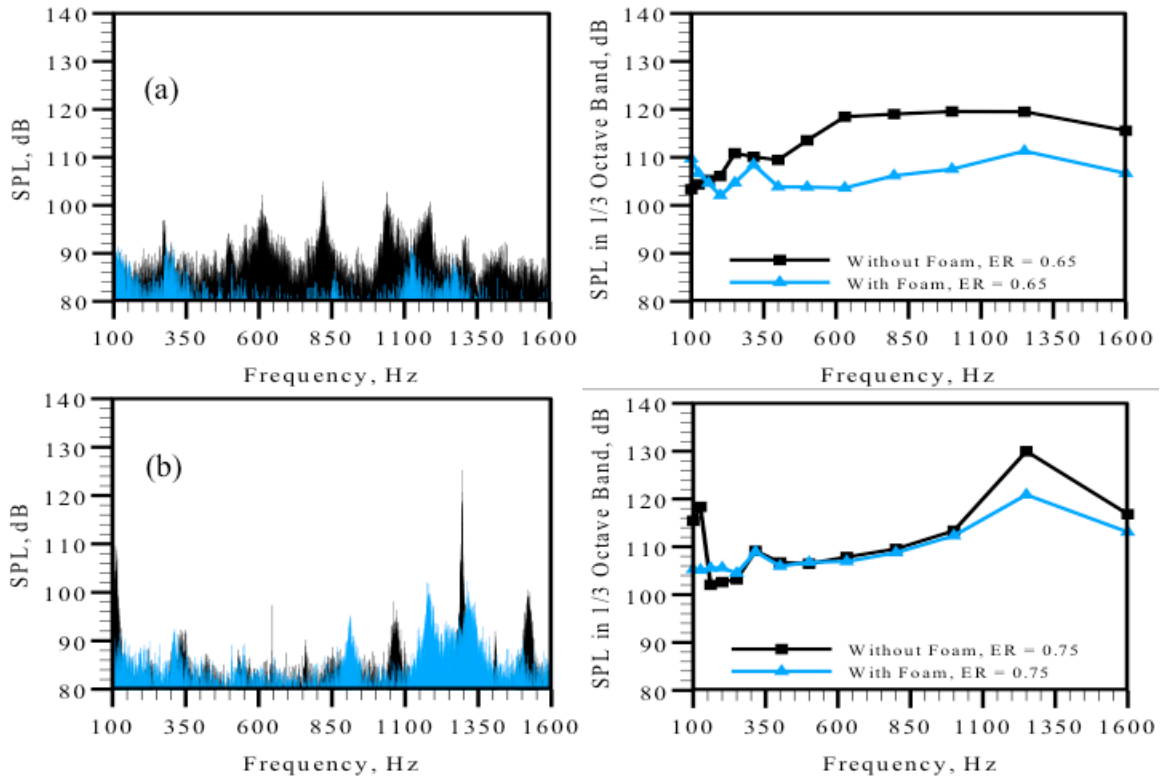


Figure 3.11. Acoustic power spectra and SPL in 1/3rd octave band for P = 0.304 MPa, Q = 300 LPM, (a) $\phi = 0.65$ (case P3-65), and (b) $\phi = 0.75$ (case P3-75)

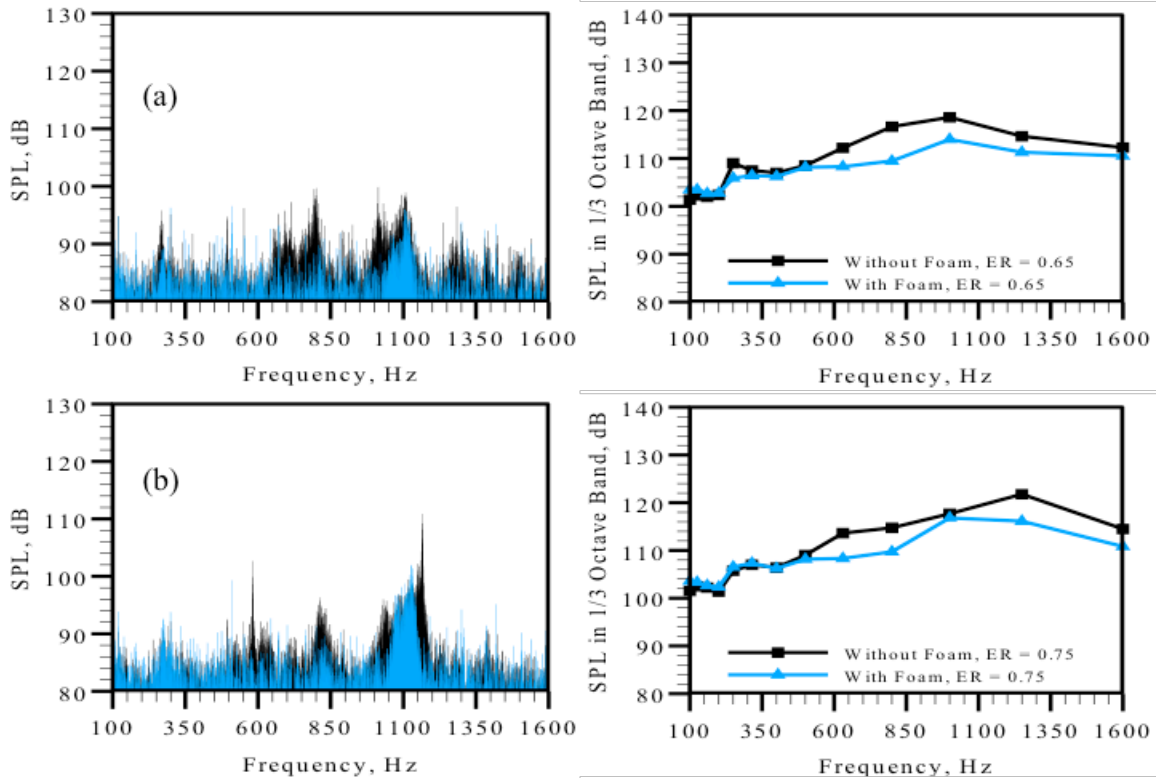


Figure 3.12. Acoustic power spectra and SPL in 1/3rd octave band for $P = 0.101$ MPa, $Q = 300$ LPM, (a) $\phi = 0.65$ (case P1-65), and (b) $\phi = 0.75$ (case P1-75)

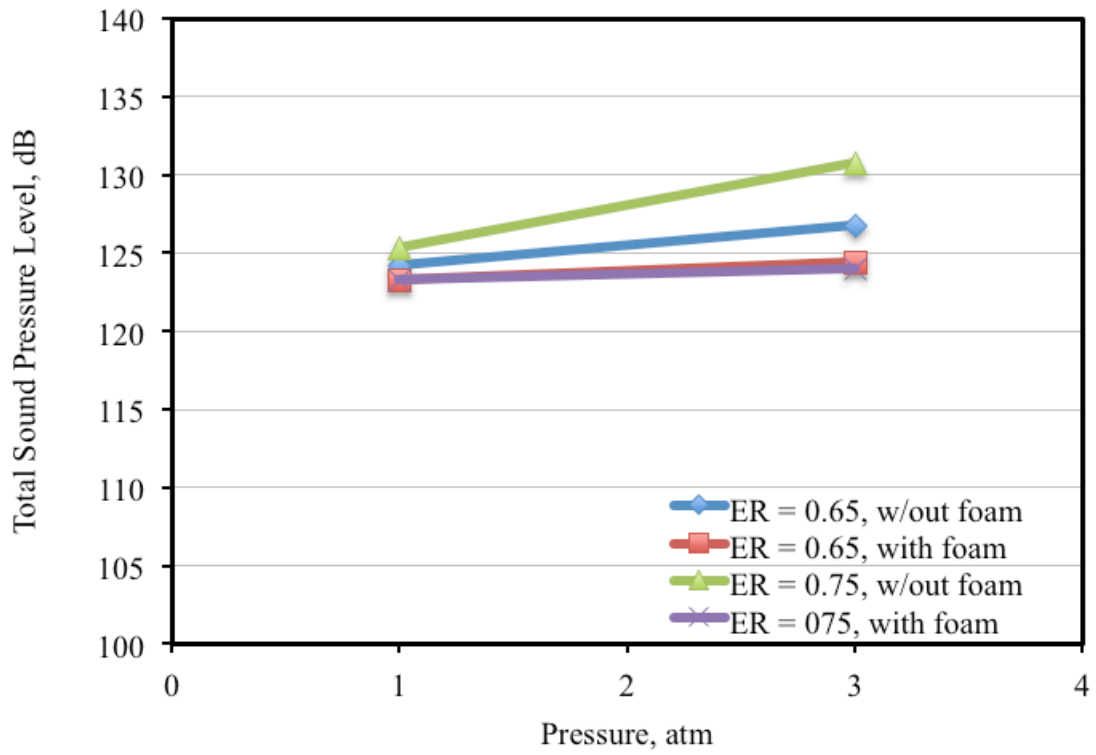


Figure 3.13. Plot of total sound pressure levels, gathered during steel combustor experiments, for cases with flow rate, $Q = 300$ LPM



Primary erosion (along inner rim)

Fractures

Figure 3.14. Signs of critical surface temperatures when operating with a steel combustor at elevated pressures, this one $Q = 300$ LPM, $P \leq 0.304$ MPa (3 atm) and $\phi \leq 0.75$

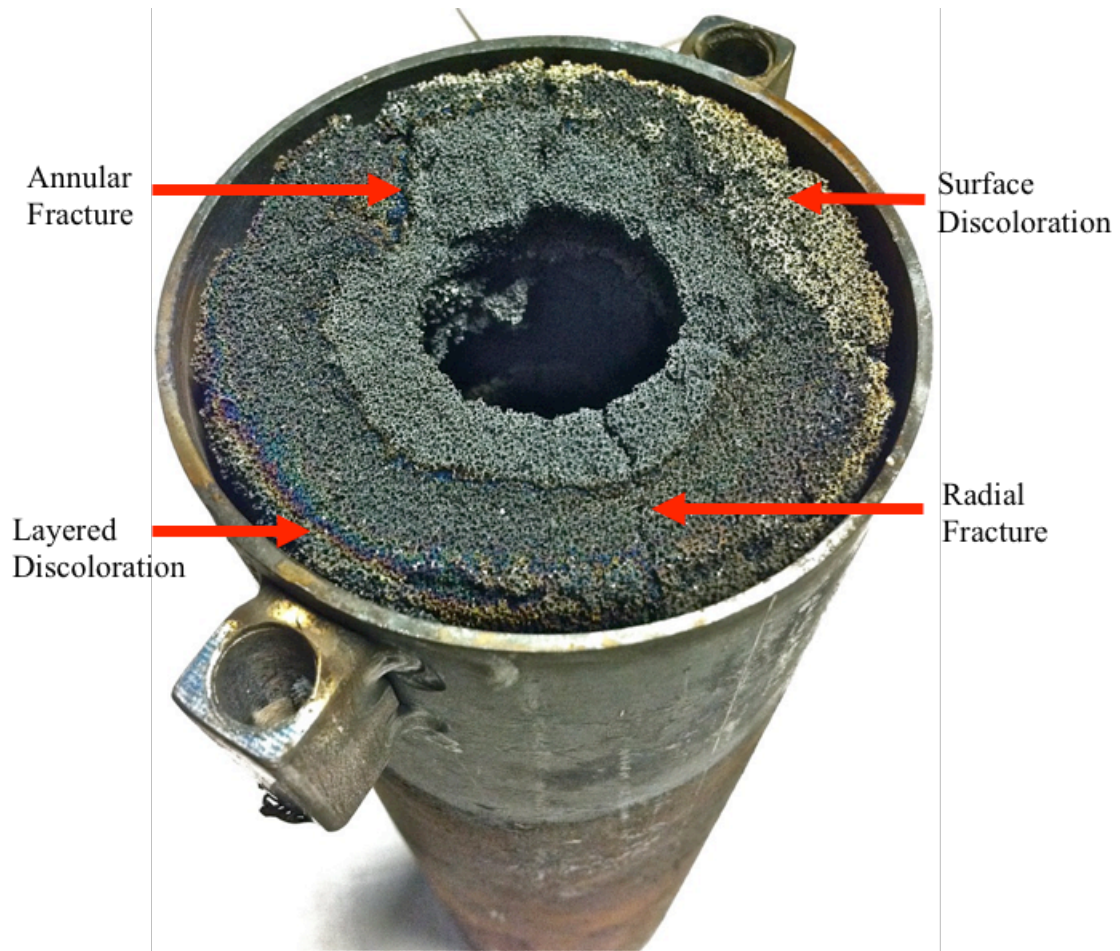


Figure 3.15. Upstream surface of PIM damaged and seized by heat in test case

$Q = 400 \text{ LPM}$, $P = 0.405 \text{ MPa (4 atm)}$, and $\phi \leq 0.75$

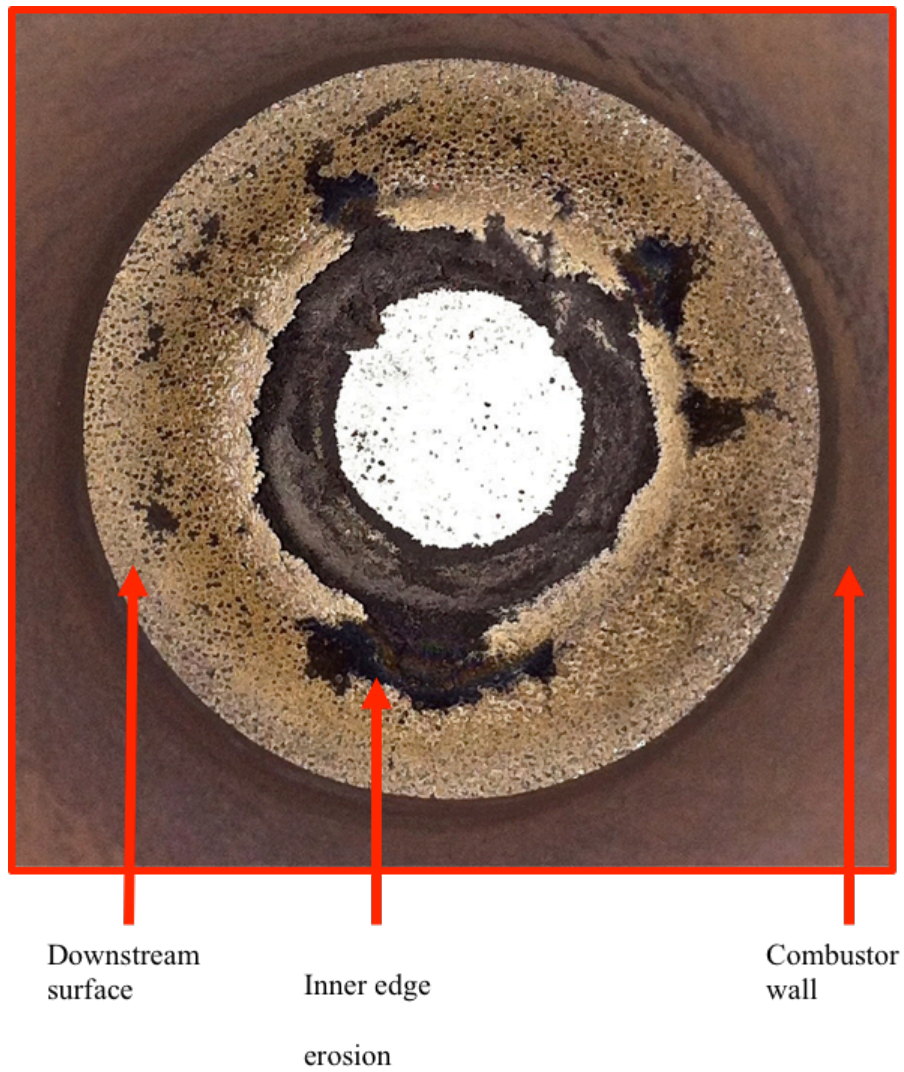


Figure 3.16. PIM damaged and seized by heat in test case Q = 400 LPM, P = 0.405 MPa (4 atm), and $\phi \leq 0.75$

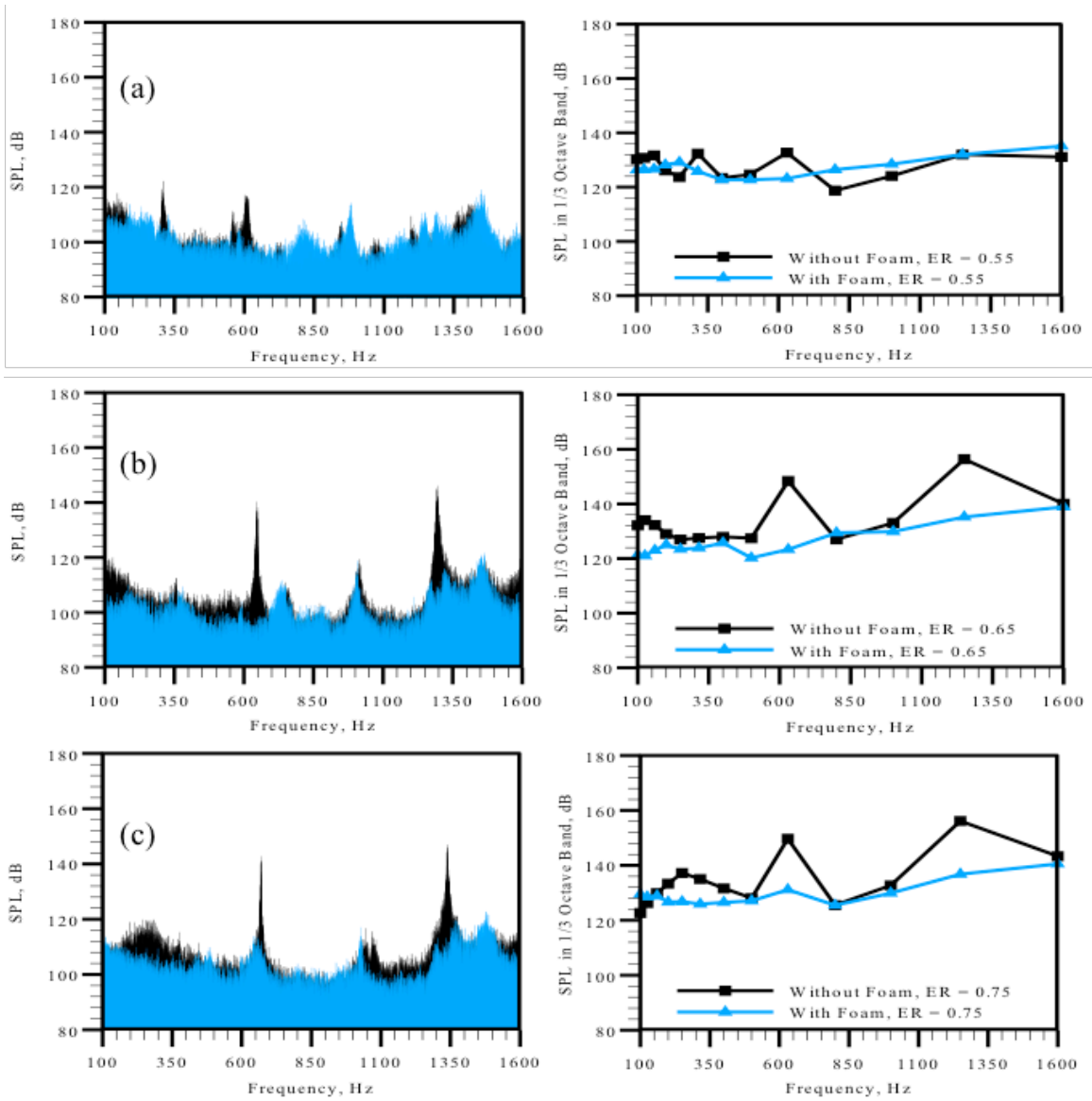


Figure 3.17. Acoustic power spectra and SPL in 1/3rd octave band for P = 0.405 MPa, Q = 400 LPM, (a) $\phi = 0.55$ (case P4-55), (b) $\phi = 0.65$ (case P4-65), and (c) $\phi = 0.75$ (case P4-75)

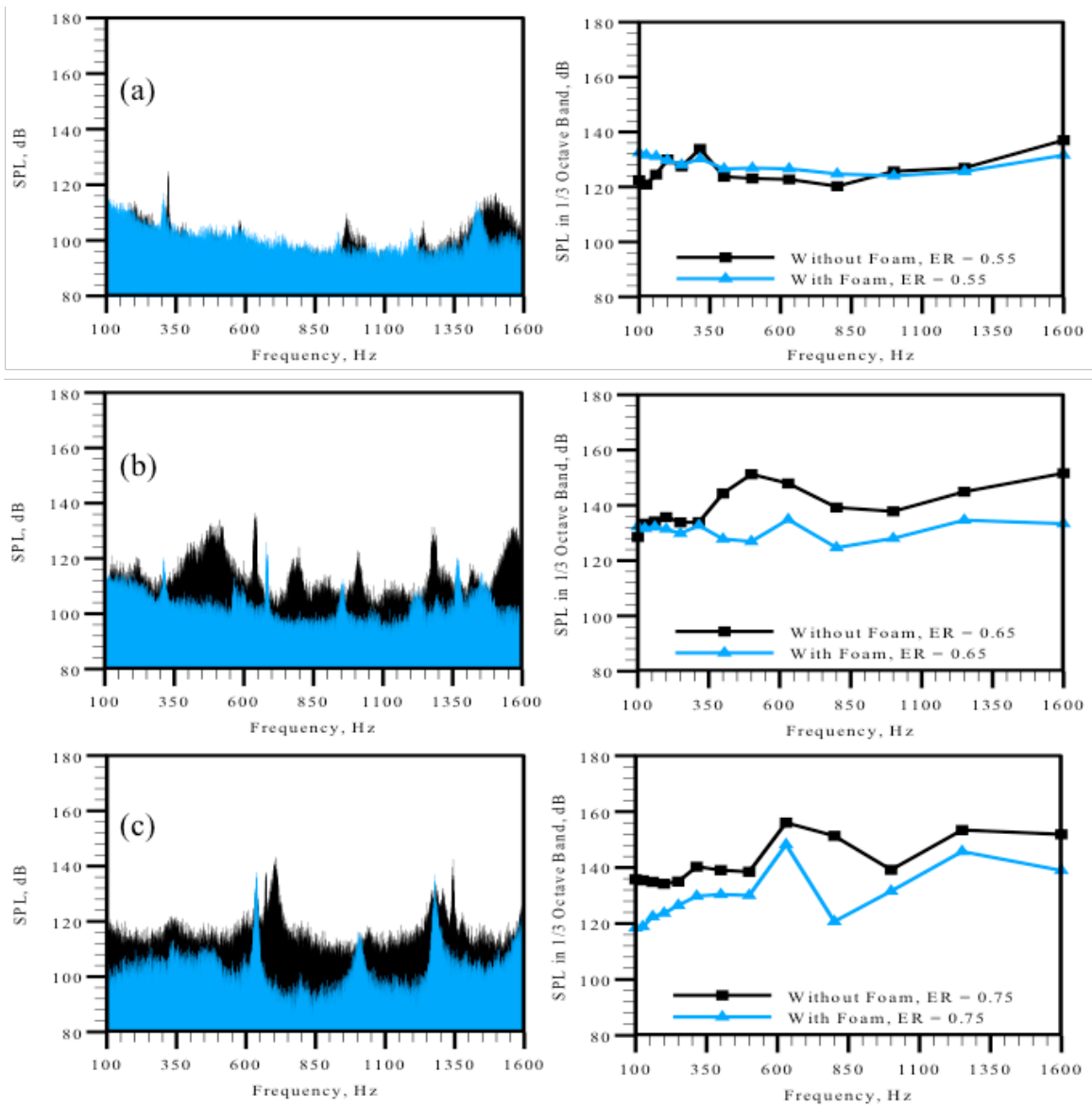


Figure 3.18. Acoustic power spectra and SPL in 1/3rd octave band for $P = 0.304$ MPa, $Q = 400$ LPM, (a) $\phi = 0.55$ (case P3-55), (b) $\phi = 0.65$ (case P3-65), and (c) $\phi = 0.75$ (case P3-75)

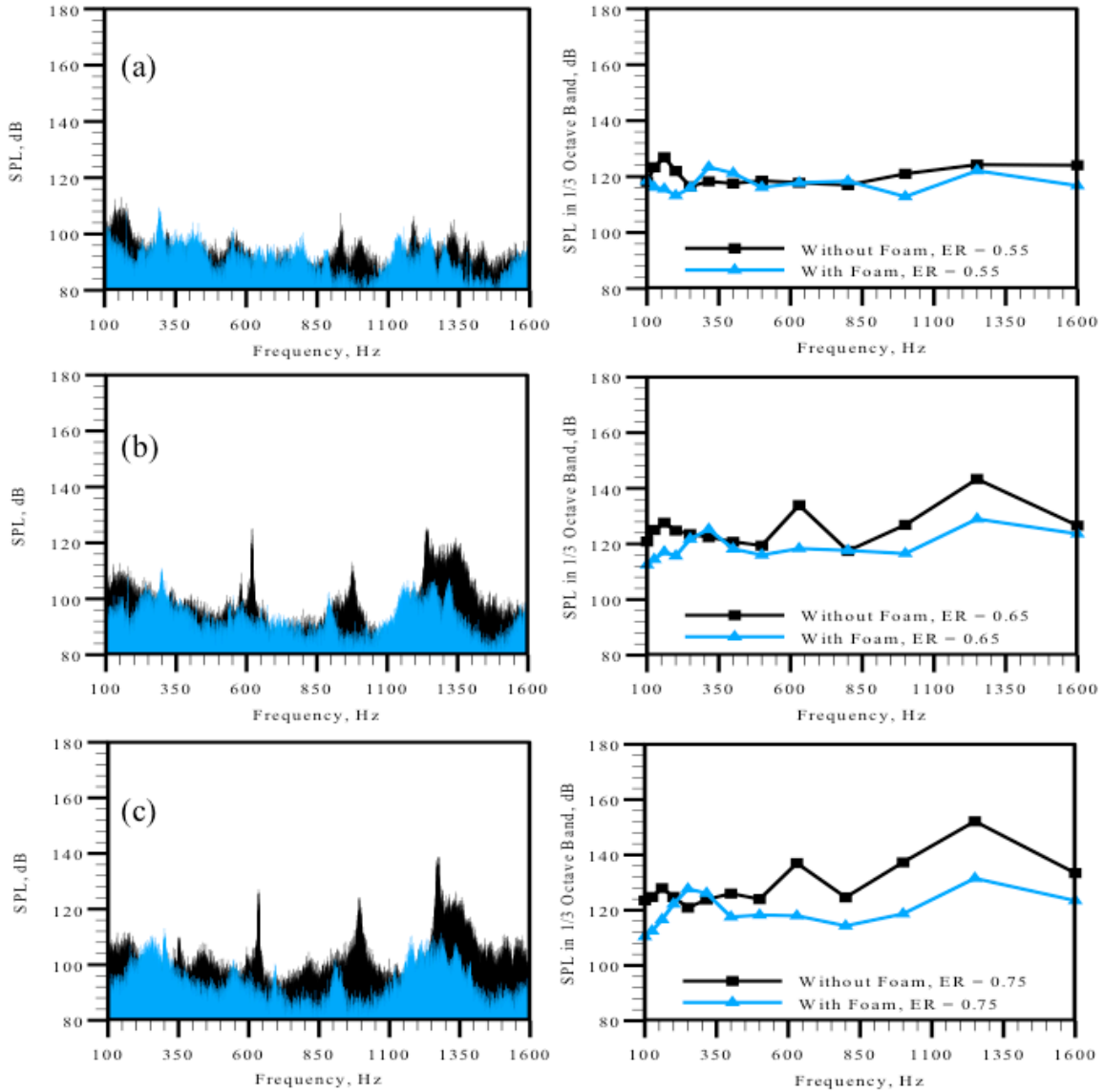


Figure 3.19. Acoustic power spectra and SPL in $1/3^{\text{rd}}$ octave band for $P = 0.203 \text{ MPa}$, $Q = 400 \text{ LPM}$, (a) $\phi = 0.55$ (case P2-55), (b) $\phi = 0.65$ (case P2-65), and (c) $\phi = 0.75$ (case P2-75)

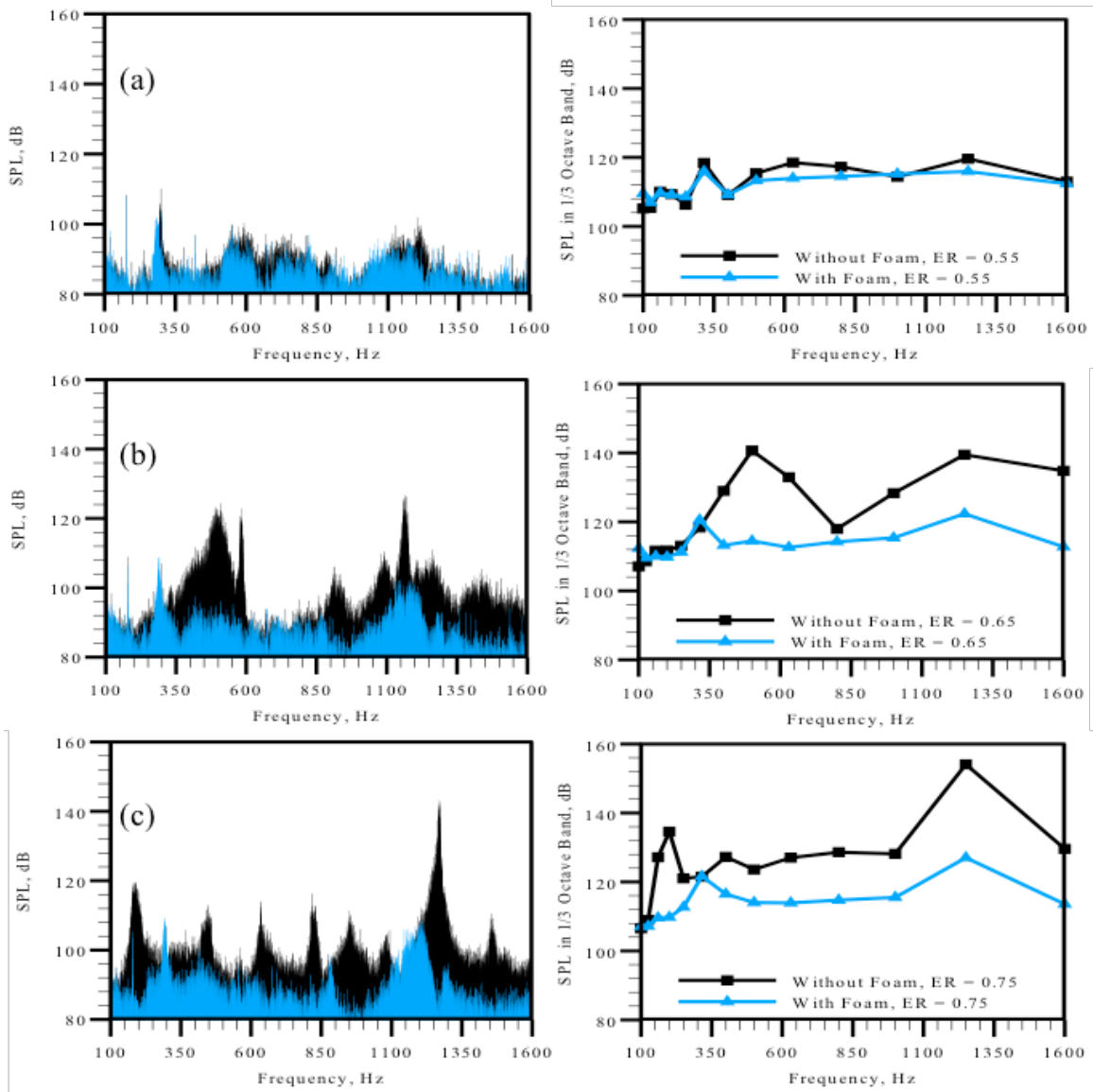


Figure 3.20. Acoustic power spectra and SPL in $1/3^{\text{rd}}$ octave band for $P = 0.101$ MPa, $Q = 400$ LPM, (a) $\phi = 0.55$ (case P1-55), (b) $\phi = 0.65$ (case P1-65), and (c) $\phi = 0.75$ (case P1-75)

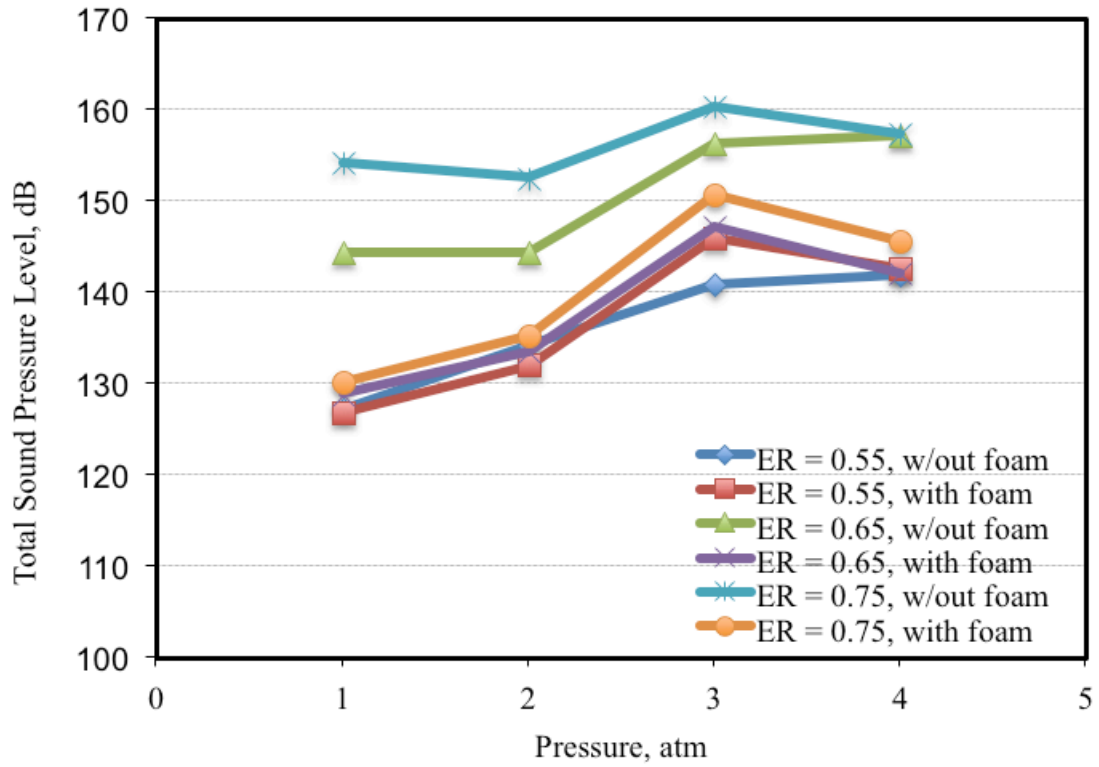


Figure 3.21. Plot of total sound pressure levels, gathered during quartz combustor experiments, for cases with baseline flow rate, $Q = 400$ LPM

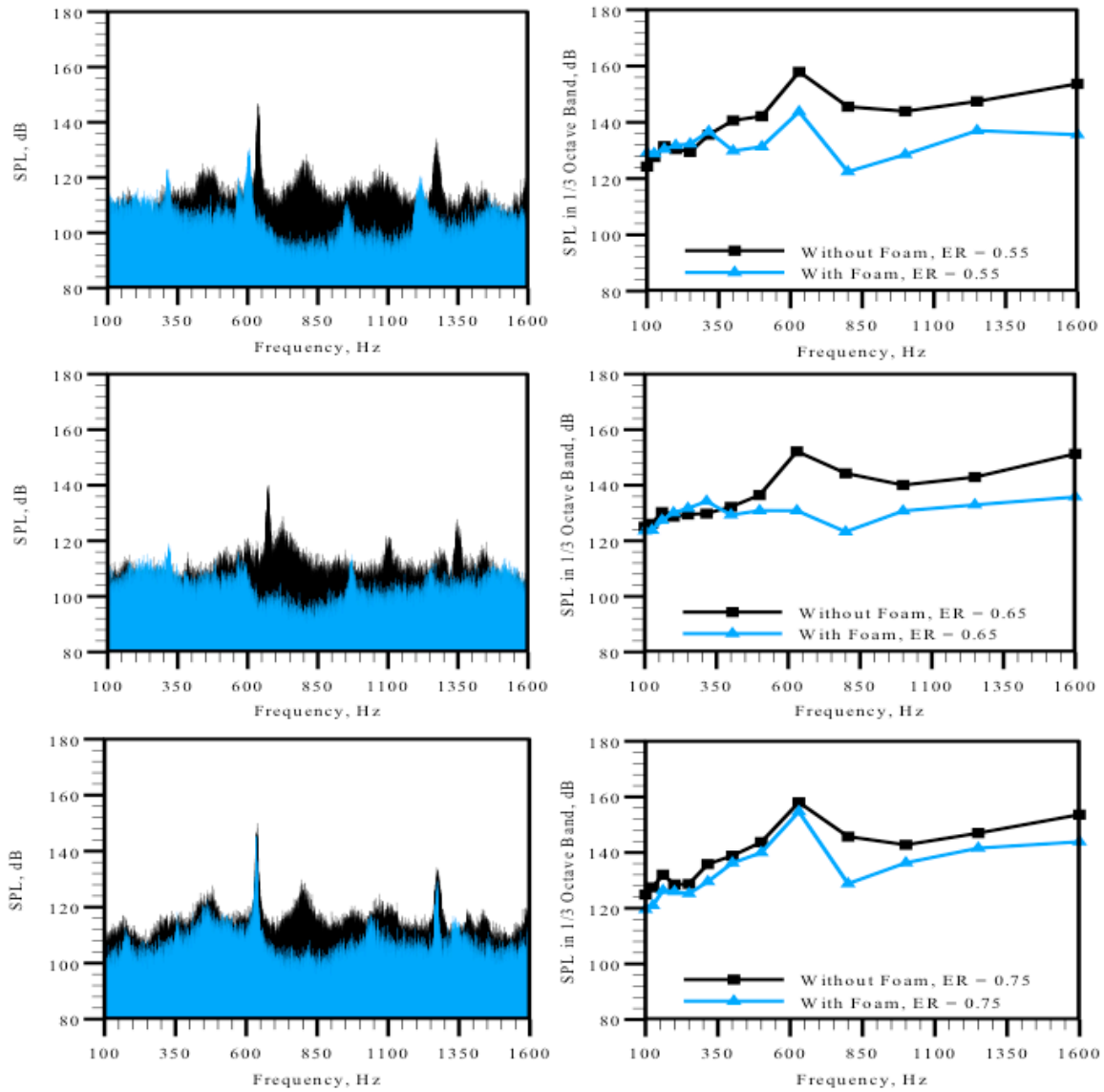


Figure 3.22. Acoustic power spectra and SPL in 1/3rd octave band for P = 0.304 MPa, Q = 600 LPM, (a) $\phi = 0.55$ (case P3-55), (b) $\phi = 0.65$ (case P3-65), and (c) $\phi = 0.75$ (case P3-75)

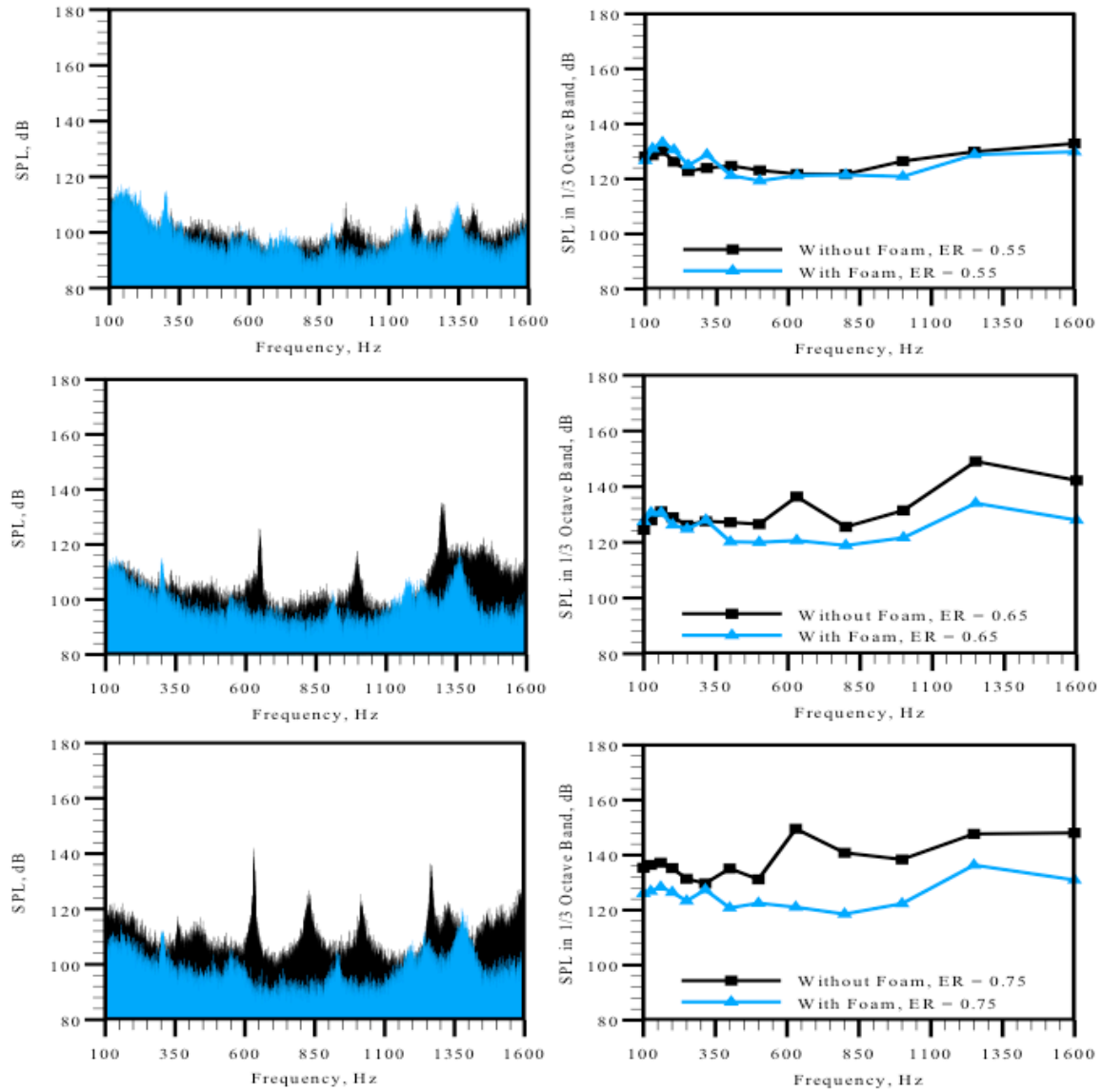


Figure 3.23. Acoustic power spectra and SPL in 1/3rd octave band for $P = 0.203$ MPa, $Q = 600$ LPM, (a) $\phi = 0.55$ (case P2-55), (b) $\phi = 0.65$ (case P2-65), and (c) $\phi = 0.75$ (case P2-75)

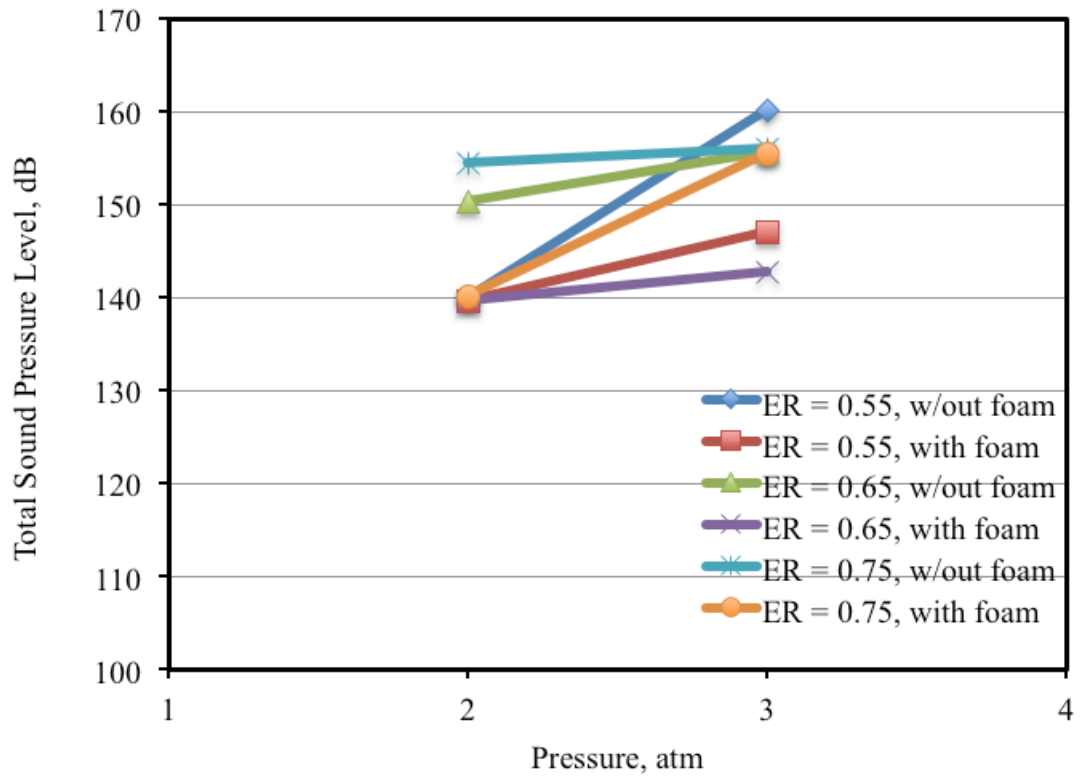


Figure 3.24. Plot of total sound pressure levels, gathered during quartz combustor experiments, for cases with baseline flow rate, $Q = 400$ LPM

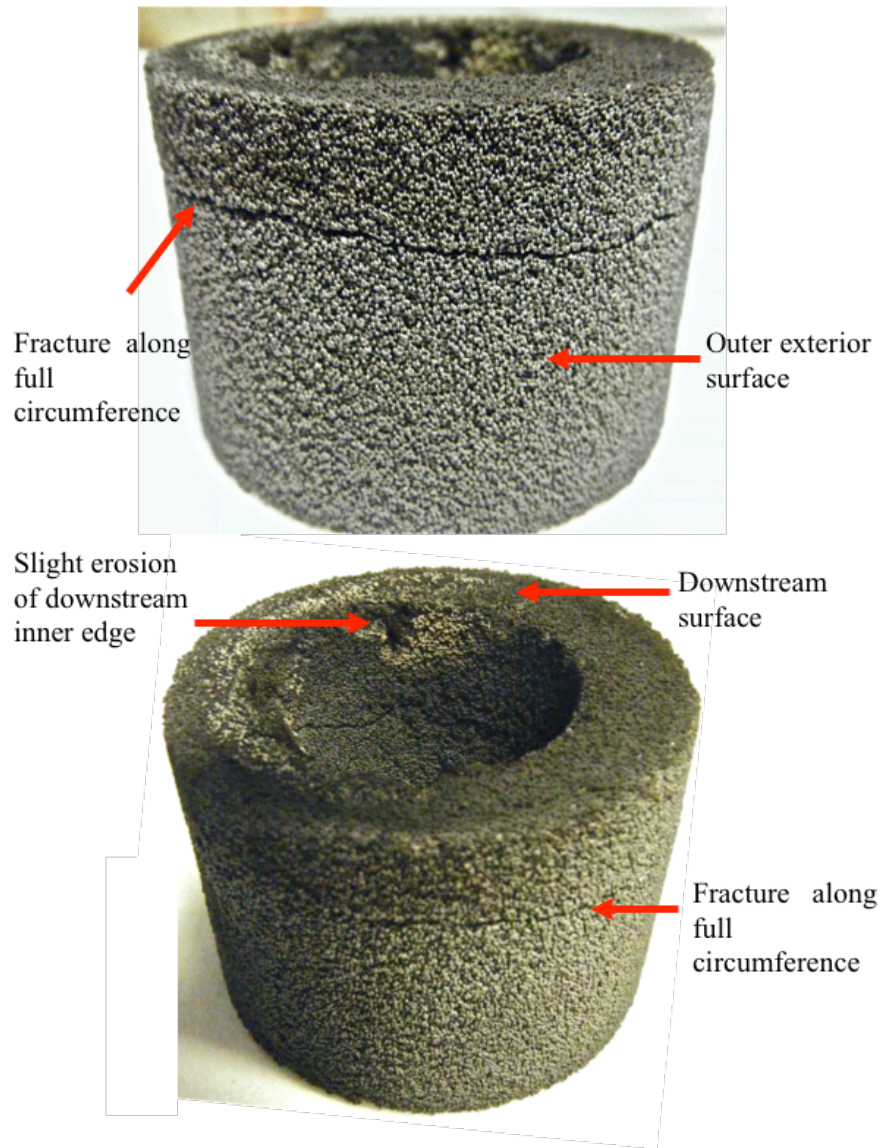


Figure 3.25. PIM fractured along its full circumference after completing experiments for cases with $Q = 400$ LPM and 600 LPM; $P = 0.203$ MPa (2 atm); and $\phi = 0.55, 0.65$ and 0.75

CHAPTER 4

CONCLUSIONS AND RECOMMENDATIONS

4.1 Conclusions

The present study retrofits a swirl-stabilized lean-premixed combustor by inserting ceramic foam at the dump plane to mitigate combustion instabilities and suppress combustion noise. The passive approach alters the flow field within reaction zones to fundamentally reduce both turbulent intensities and heat release rate fluctuations that lead to thermo-acoustic instabilities. The technique reduces direction combustion noise and minimizes resulting instabilities.

An experimental apparatus was developed within a high-pressure combustion laboratory facility to perform experiments over a range of operating pressures, equivalence ratios, and reactant flow rates. The design features and operating procedure of the facility are presented in detail. The experimental apparatus was used to conduct an extensive set of combustion tests for analyzing the performance characteristics of PIM combustion at elevated pressures. The mitigation of thermo-acoustic instabilities with ceramic foam inserted was examined by operating at conditions that exhibited consistent instabilities without the foam inserted. Total SPL was quantified both without and with PIM for each test case. Results from this study can be utilized for optimizing PIM geometry for high-pressure combustion. With PIM optimized, future work should be conducted at elevated pressures beyond 5 atm.

Main conclusions from the work presented are:

- Significant reduction in peak sound pressure levels that were the result of harmonic excitations was achieved using PIM combustion in a swirl-stabilized

LPM combustor. Findings mostly agreed with those of *Sequera and Agrawal* (2011), which reported the effectiveness and optimization characteristics of PIM combustion at atmospheric pressure. PIM combustion is qualified as an effective passive control strategy for combustion noise and combustion instabilities within a high pressure gaseous combustion system operating at lean equivalence ratios.

- The ceramic foam insert was proven to be consistently effective at reducing, if not completely eliminating, densely concentrated peaks in SPL, or, instabilities. In such cases, instability was shown to be a dominant source of total sound pressure level; thus, the elimination of instability resulted in significant reduction of total SPL.
- Insert surface temperatures, elevated by high chamber pressure, presented issues with PIM durability during high-pressure experiments. As result, a custom quartz combustion chamber was designed to minimize the heating of the foam material. Results were compared between experiments conducted with a steel combustion chamber and experiments conducted with the custom quartz combustor. Sound power frequency behavior was shown to be consistent for both combustion chambers; however, peaks were more defined for cases with the quartz combustor. Likely, elevated product gas temperatures, occurring with the quartz combustor, were responsible for enhanced spectral definition. It was common to find that the consistent frequency behavior slightly shifted phase forward (+ 50 Hz) for cases of higher heat release rates (e.g. from case P4-65 to case P4-75). The consistent spectral behavior with the test rig suggests that the

instabilities are a flow and temperature driven cavity resonance rather than a structural one.

4.2 Recommendations

Recommendations for future research and improvement of current work are:

- Reduce PIM pore density and/or begin diffusion of PIM slightly downstream (~ 0.5 inch) of dump plane to enhance reactant flow penetration at all operating conditions.
- Further optimize PIM parameters and combustor/mounting mechanism to eliminate foam insert fatigue during elevated pressure operations.
- Conduct high-pressure testing with increased reactant inlet temperatures.
- Implement combustion with PIM in a high-pressure liquid fuel combustion system.

REFERENCES

- Agrawal, A.K. & S. Vijaykant, (2010). Passive Noise Attenuation System. *U.S. Patent Application 20100059311*, The University of Alabama.
- Bussman, W. & Jayakaran, J. (2001). *Noise. The John Zink Combustion Handbook*. New York: CRC Press.
- Cabot, G., Vauchelles, D., Taupin, B., & Boukhalfa, A. (2004). Experimental study of lean premixed turbulent combustion in a scale gas turbine chamber. *Experimental Thermal and Fluid Science*, 28, 683-690.
- Choi, G.-M., Tanahashi, M., & Miyauchi, T. (2005). Control of oscillating combustion and noise based on local flame structure. *Proceedings of the Combustion Institute*, 30, pp. 1807-1814. Elsevier.
- Duchaine, P., Zimmer, L., & Schuller, T. (2009). Experimental investigation of mechanisms of sound production by partially premixed flames. *Proceedings of the Combustion Institute*, 32, pp. 1027-1034. Elsevier.
- Durox, D., Schuller, T., Noiray, N., Birbaud, A. L., & Candel, S. (2009). Rayleigh criterion and acoustic energy balance in unconfined self-sustained oscillating flames. *Combustion and Flame*, 156, 106-119.
- Flemming, F., Sadiki, A., & Janicka, J. (2007). Investigation of combustion noise using a LES/CAA hybrid approach. *Proceedings of the Combustion Institute*, 31, pp. 3189-3196. Elsevier.
- Hirsch, C., Wasle, J., Winkler, A., & Sattelmayer, T. (2007). A spectral model for the sound pressure from turbulent premixed combustion. *Proceedings of the Combustion Institute*, 31, pp. 1435-1441. Elsevier.
- Huang, Y., & Yang, V. (2009). Dynamics and stability of lean-premixed swirl-stabilized combustion. *Progress in Energy and Combustion Science*, 35, 293-364.
- Huang, Y., & Yang, V. (2005). Effect of swirl on combustion dynamics in a lean-premixed swirl-stabilized combustor. *Proceedings of the Combustion Institute*, 30, pp. 1775-1782. Elsevier.
- Johnson, C. E., Neumeier, Y., Lieuwen, T. C., & Zinn, B. T. (2000). Experimental determination of the stability margin of a combustor using exhaust flow and fuel inject rate modulations. *Proceedings of the Combustion Institute*, 28, pp. 757-763.

- Naeem, M., Singh, R., & Probert, D. (2000). Implications of engine's deterioration upon an aero-engine HP turbine blade's thermal fatigue life. *International Journal of Fatigue* , 22, 147-160.
- Noiray, N., Durox, D., & Schuller, T. C. (2009). Dynamic phase converter for passive control of combustor instabilities. *Proceedings of the Combustion Institute*. 32, pp. 3163-3170. Elsevier.
- Rabinowitz, P. M. (2000). Noise-Induced hearing loss. *American Family Physician* , 61 (9) , 2749-56, 2759-60.
- Rajaran, R., Gray, L., Lieuwen, T. (2006). Premixed combustion noise scaling: Total power and spectra. *AIAA paper* 2006-2612
- Richards, G. A., Mcmillian, M. M., Gemmen, R. S., Rogers, W.A., and Cully, S. R. (2001). Issues for low-emission, fuel flexible power systems. *Progress in Energy and Combustion Science*, 27, pp. 141-169.
- Schwartz, A., Janicka, J. (2009). Combustion noise, springer-verlang Berlin Heidelberg. Germany
- Sequera, D. (2011). Reduction of combustor noise and instabilities using porous inert material with a swirl-stabilized burner. *Daniel Sequera 2011* .
- Sequera, D., & Agrawal, A. K. (2011). Passive control of noise and instability with a swirl-stabilized combustor with the use of high-strength porous insert. *Proceedings of ASME Turbo Expo*.
- Smith, Z. A. (2011). Passive control of combustion noise and thermo-acoustic instability with porous inert media. *Zachary A. Smith 2011* .
- Stohr, M., Boxx, I., Carter, C., & Weier, W. (2011). Dynamics of lean blowout of a swirl-stabilized flame in a gas turbine model combustor. *Proceedings of the Combustion Institute*. 33, pp. 2953-2960. Elsevier.
- Stone, C., & Menon, S. (2002). Swirl control of combustion instabilities in a gas turbine combustor. *Proceedings of the Combustion Institute*, 29, pp. 155-160.
- Tiribuzi, S. (2008). CFD simulation of noise in gas turbine combustors by means of turbulence re fluctuation method. *Proceedings of the ASME Turbo Expo*, 3, pp. 113-124
- Wicksall, D. M., & Agrawal, A. K. Acoustics measurements in a lean premixed combustor operated on hydrogen/hydrocarbon fuel mixtures. *International Journal of Hydrogen Energy* , 32, 1103-1112.

APPENDIX A

DETAILED DRAWINGS OF FACILITY AND EXPERIMENTAL APPARATUS

The high-pressure combustion apparatus described in Chapter 2 is located within a laboratory facility particularly designed for high-pressure experimentation. A general schematic of the entire high-pressure facility is shown in Figure A.1. The facility incorporates both an atmospheric burner and a high-pressure burner. Each burner feeds off of the same air and fuel supplies. Both air and fuel supplies are redirected from the high-pressure apparatus to the atmospheric one via 4.33" long globe valves. Flow conditions for each burner are controlled from the same central location, as shown in Figure A.2. Various schematic views of the laboratory area are featured in Figures A.3, A.4, and A.5. The combustion products from both test stands are removed from above the stands, integrated, and exhausted from a central location on the roof of the building. A photograph of the integrated exhaust system is shown in Figure A.6. Various schematic views, seen in Figures A.7, A.8, and A.9, illustrate the orientation of exhaust ducting relative to the test stands.

The high-pressure combustion apparatus is composed of a plenum base, a support pipe and flange, and an enclosure. Furthermore, the enclosure is equipped with two rectangular ports designed for optical access. In the previous enclosure design, optical windows were clamped into the rectangular ports via steel rectangular frames, which bolt to the outer surface of the enclosure. Figure A.10 shows details of the plenum base plate. Figure A.11 shows details of the support pipe and connected flange. As illustrated in Figure A.12, the threaded end of the support pipe is welded to the base plate to form the

assembled plenum base. Details of the high-pressure enclosure are given in Figures A.13, A.14, and A.15. Furthermore, as shown in Figure A.16, the enclosure wall integrates several threaded access ports. Similarly, the optical access ports are shown in Figure A.17, and the window frames are shown in Figure A.18. Details of the optical panels are shown in Figure A.19.

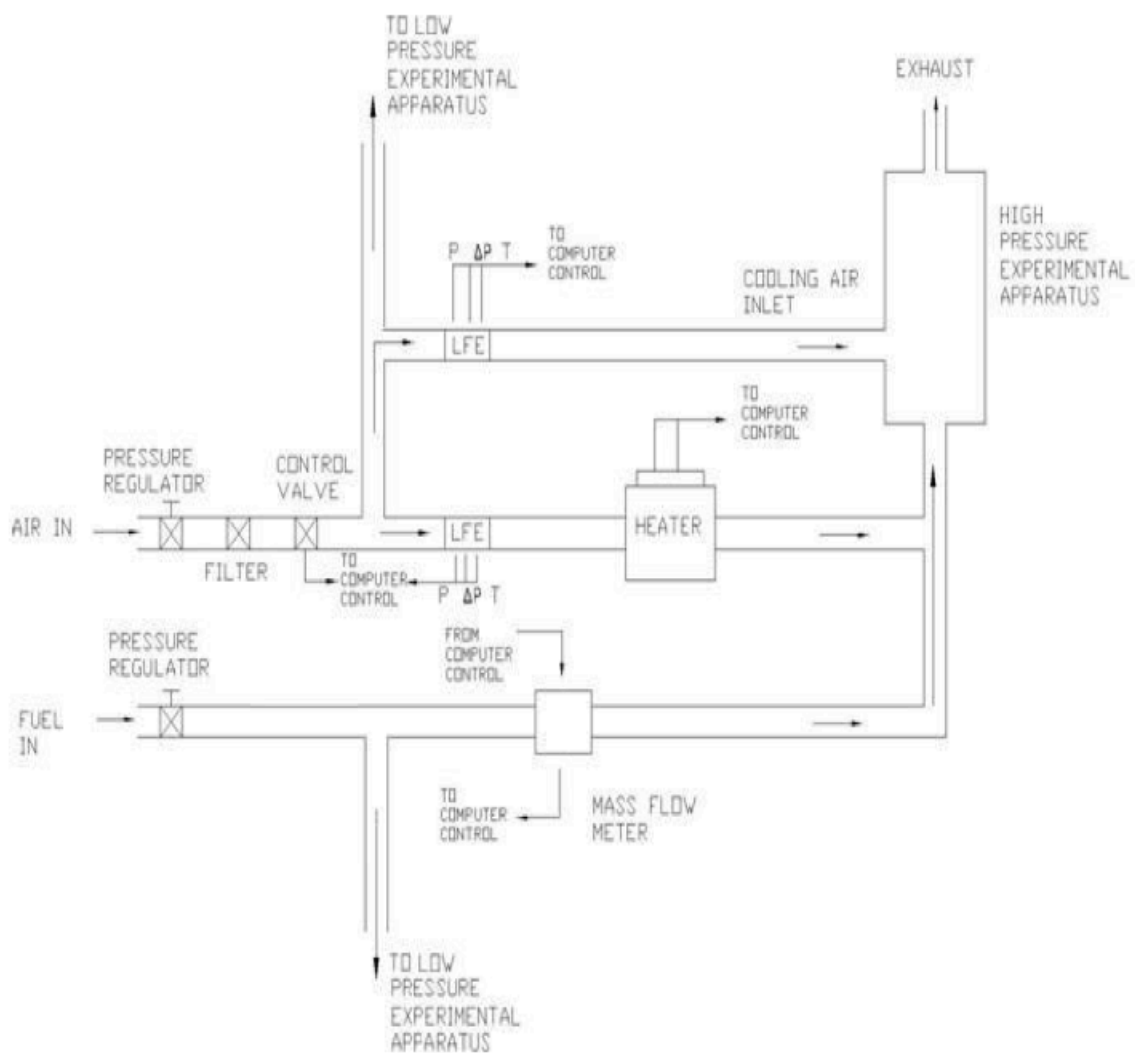


Figure A.1. General schematic of high-pressure combustion laboratory

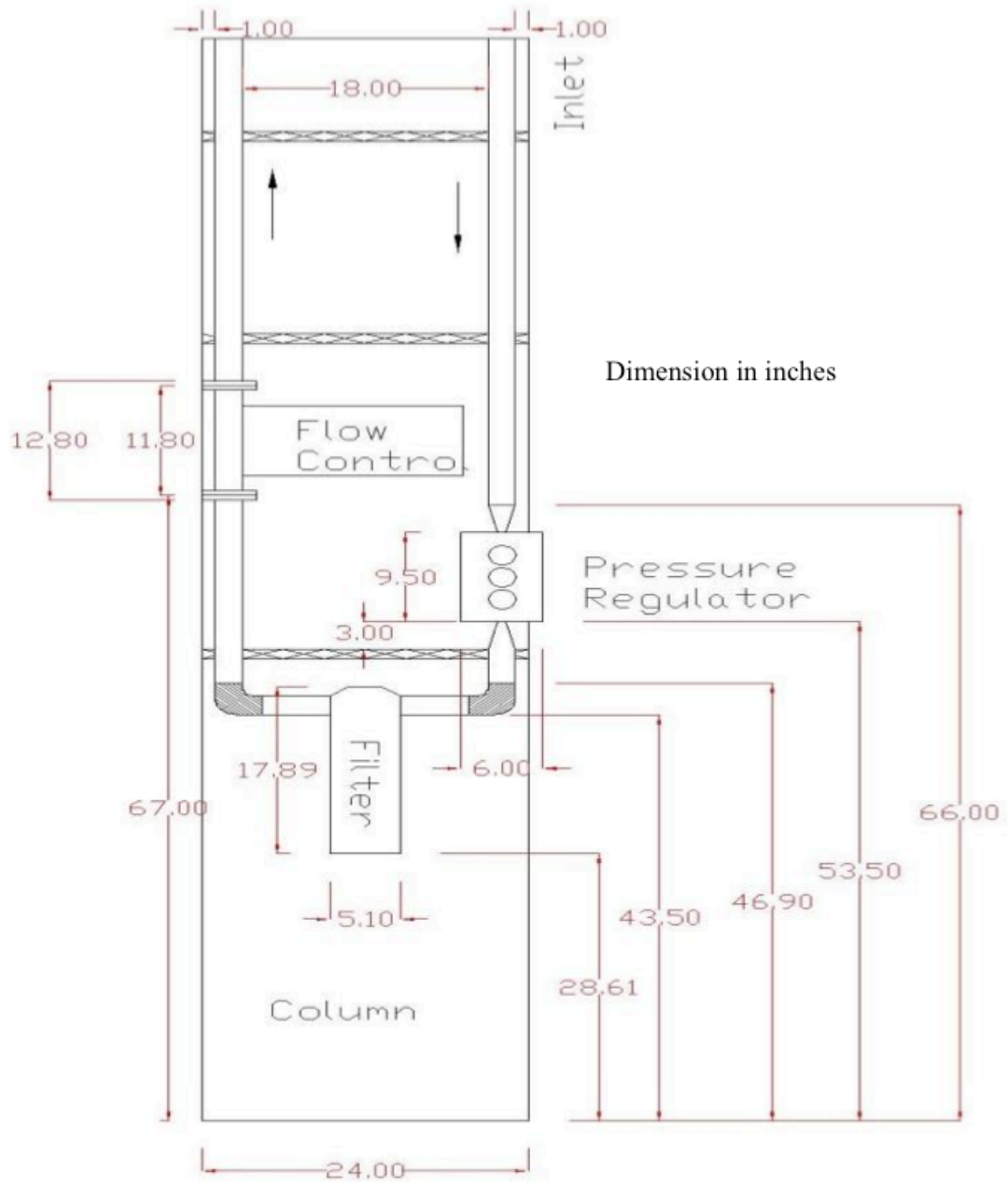


Figure A.2. Layout of air flow control system

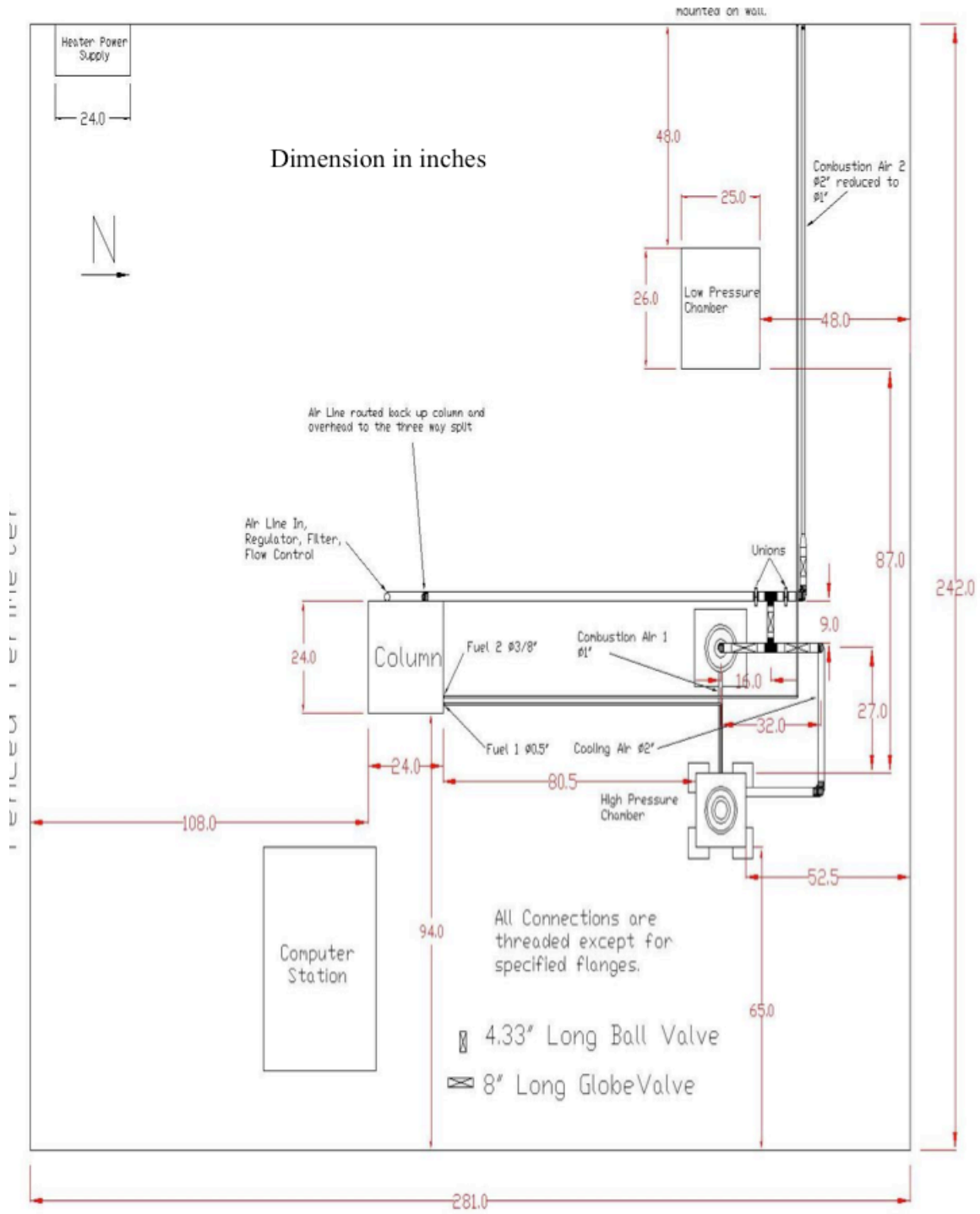


Figure A.3. Top view layout of high-pressure combustion laboratory

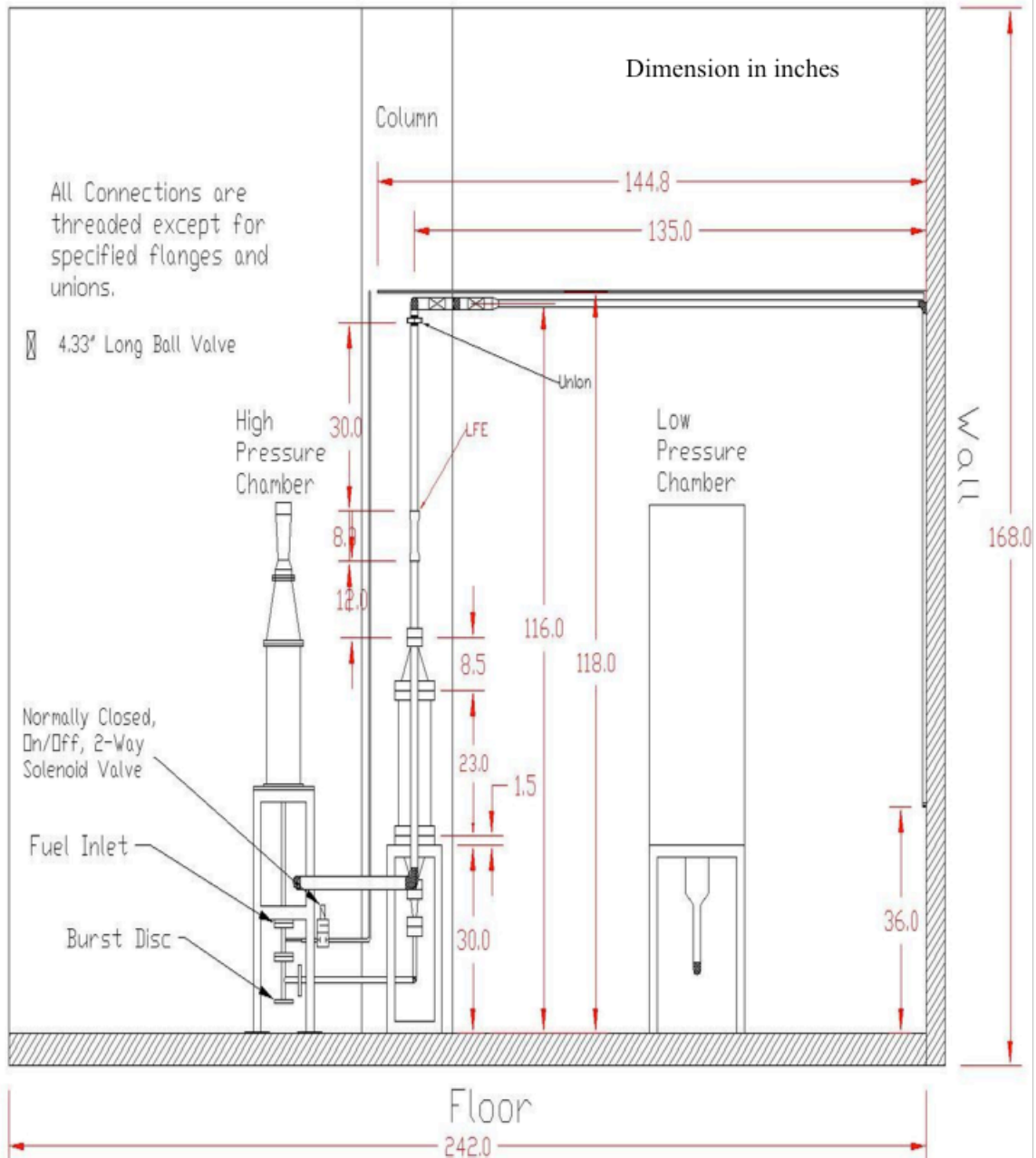


Figure A.4. Side view layout of high-pressure combustion laboratory

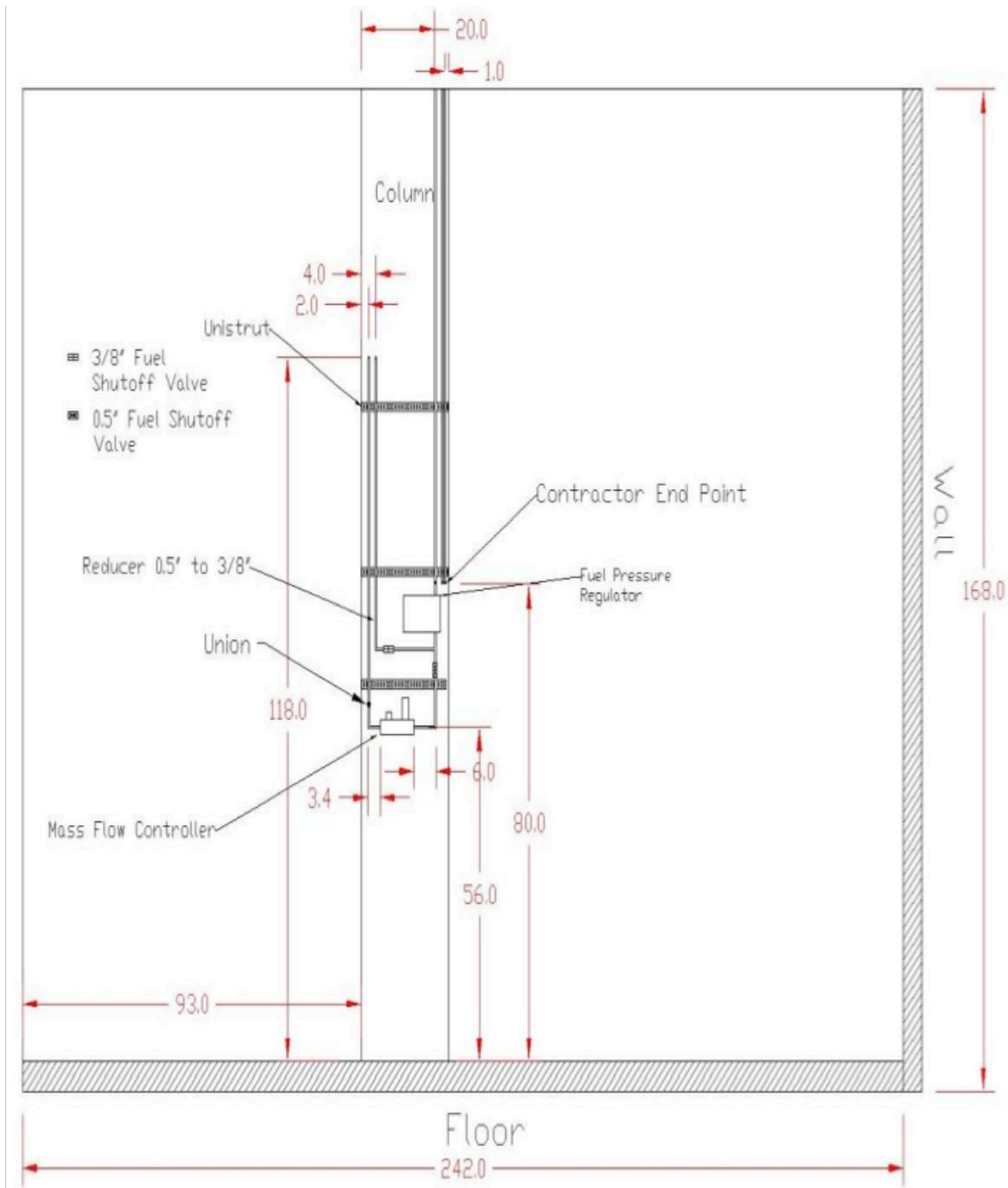


Figure A.5. Layout of fuel flow control system

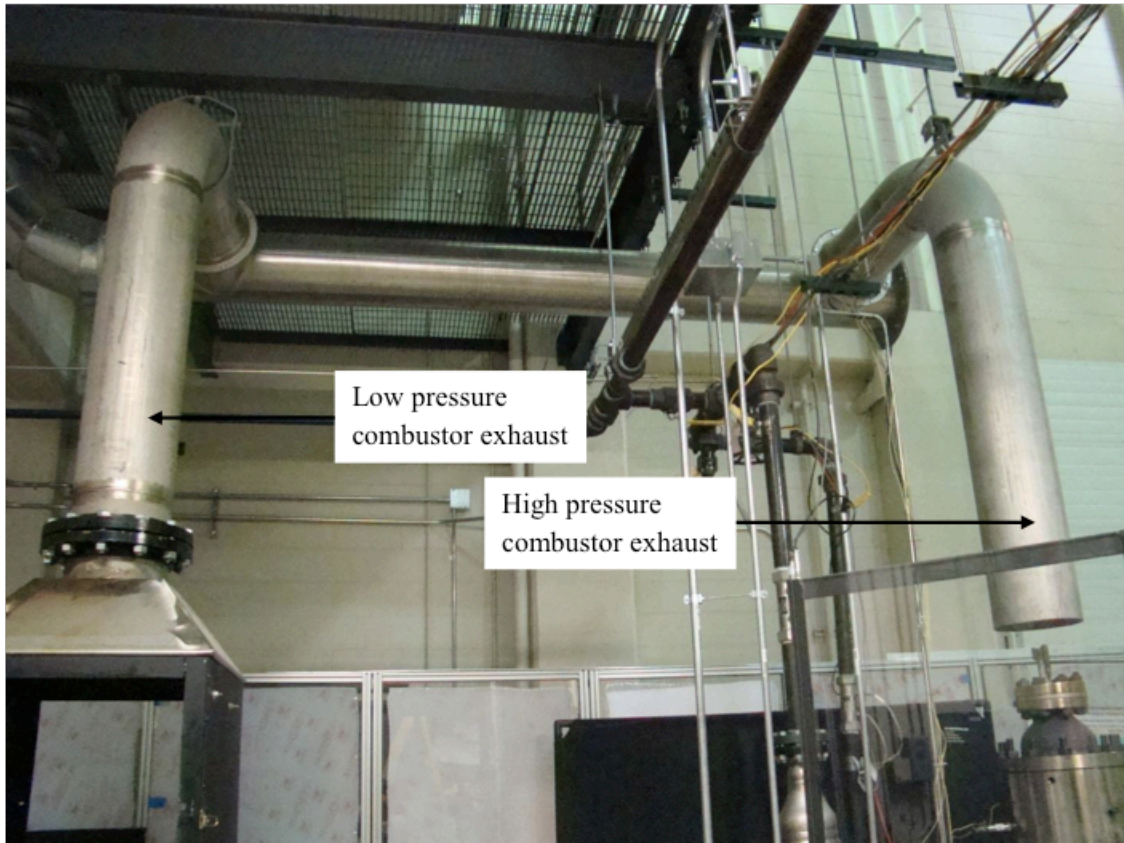


Figure A.6. Photograph (front view) of exhaust system

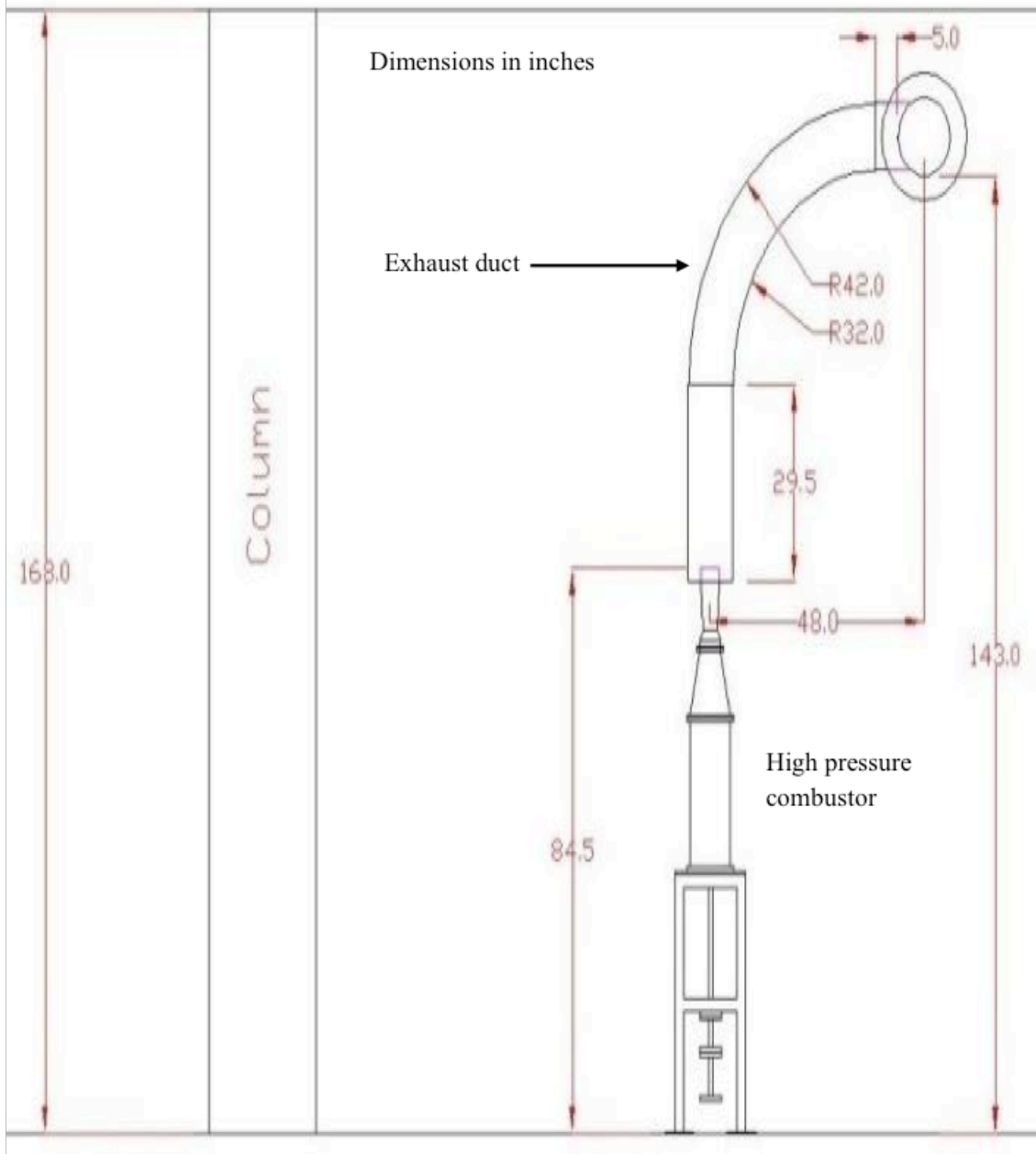


Figure A.7. Side view of exhaust system layout

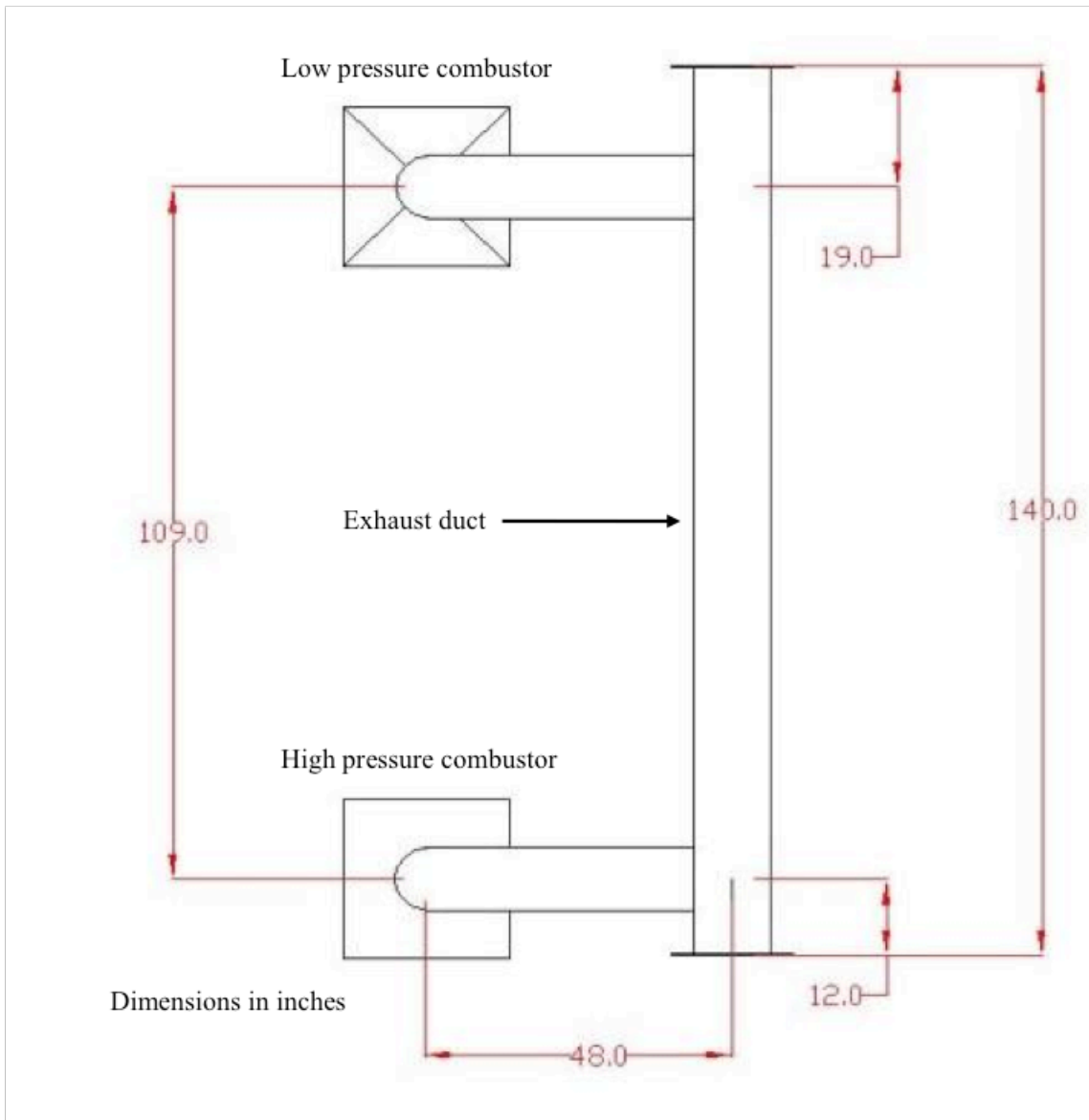


Figure A.8. Overhead view of exhaust system layout

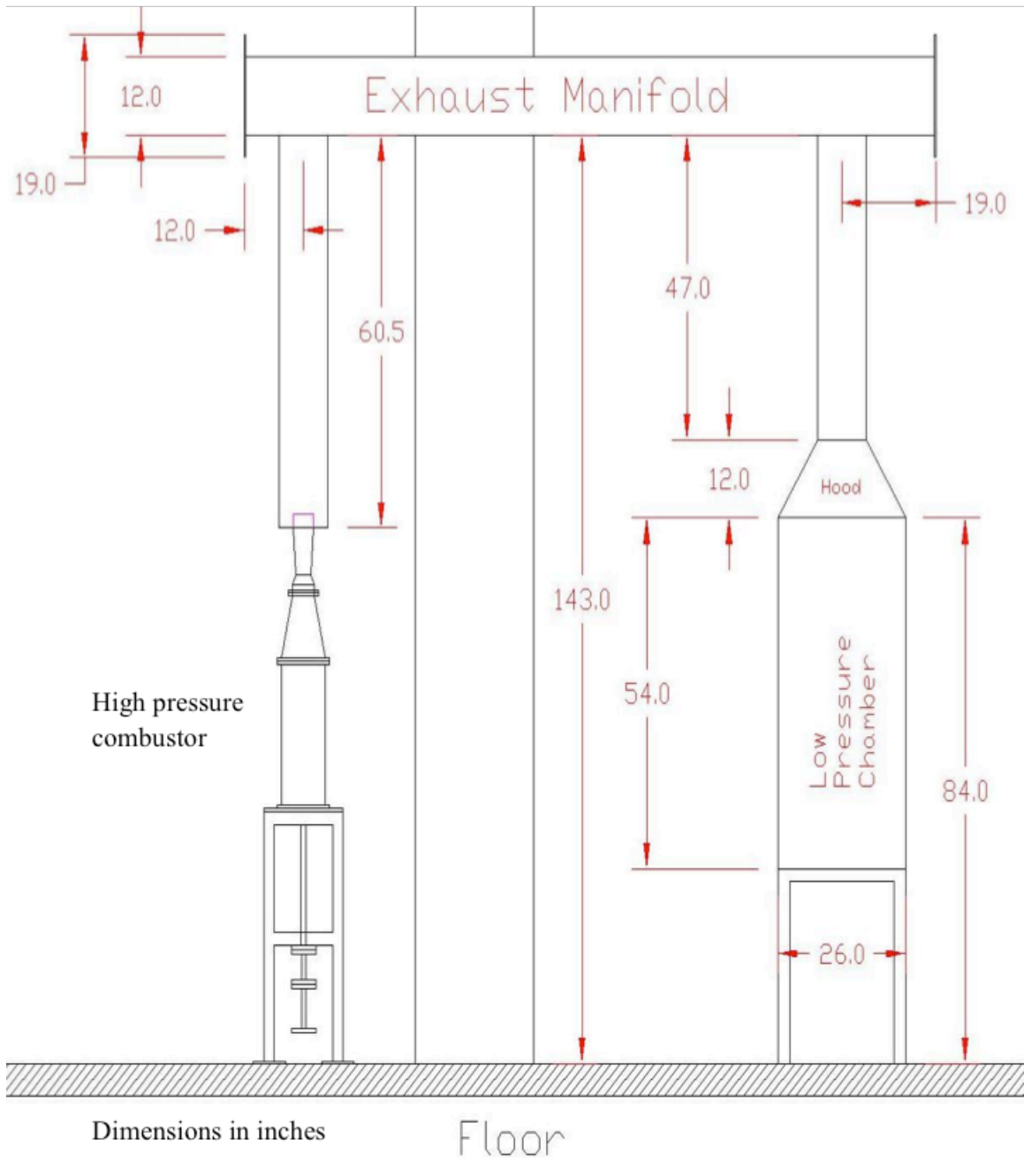


Figure A.9. Back view of exhaust system layout

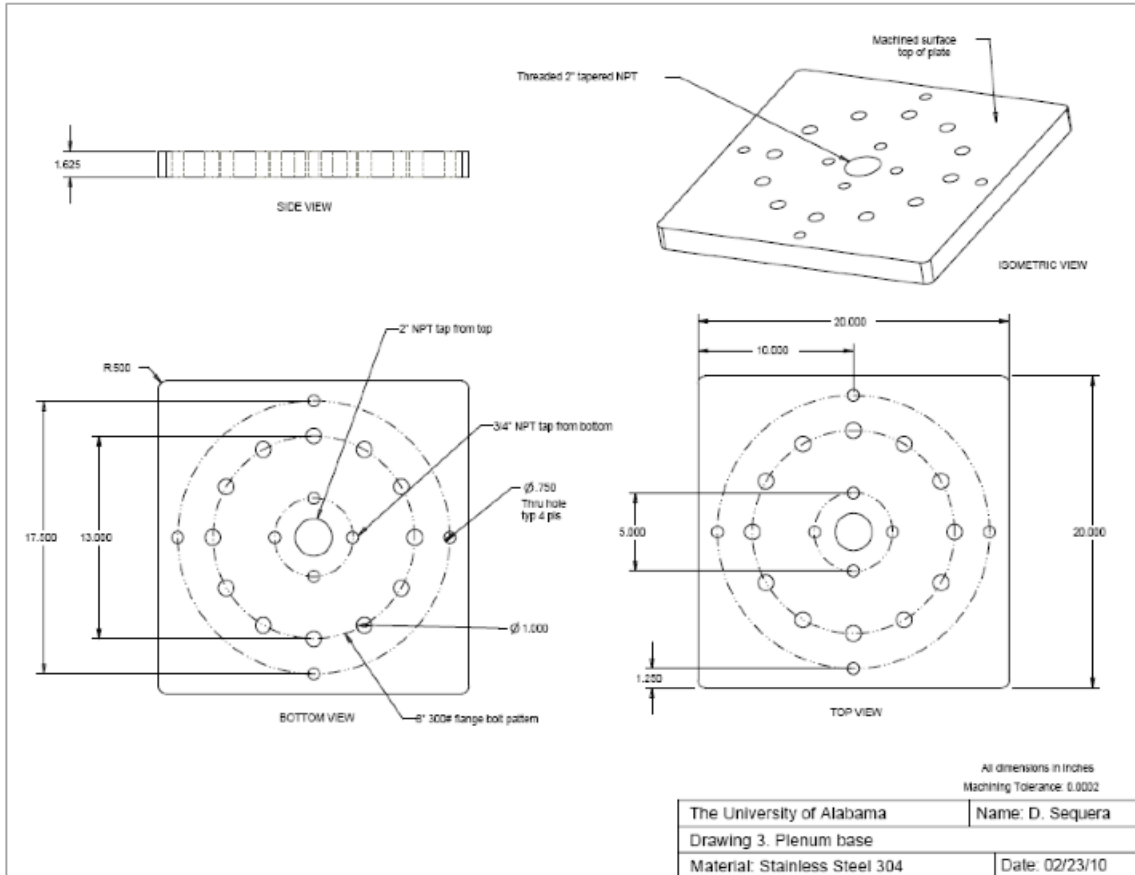


Figure A.10. Details of plenum base

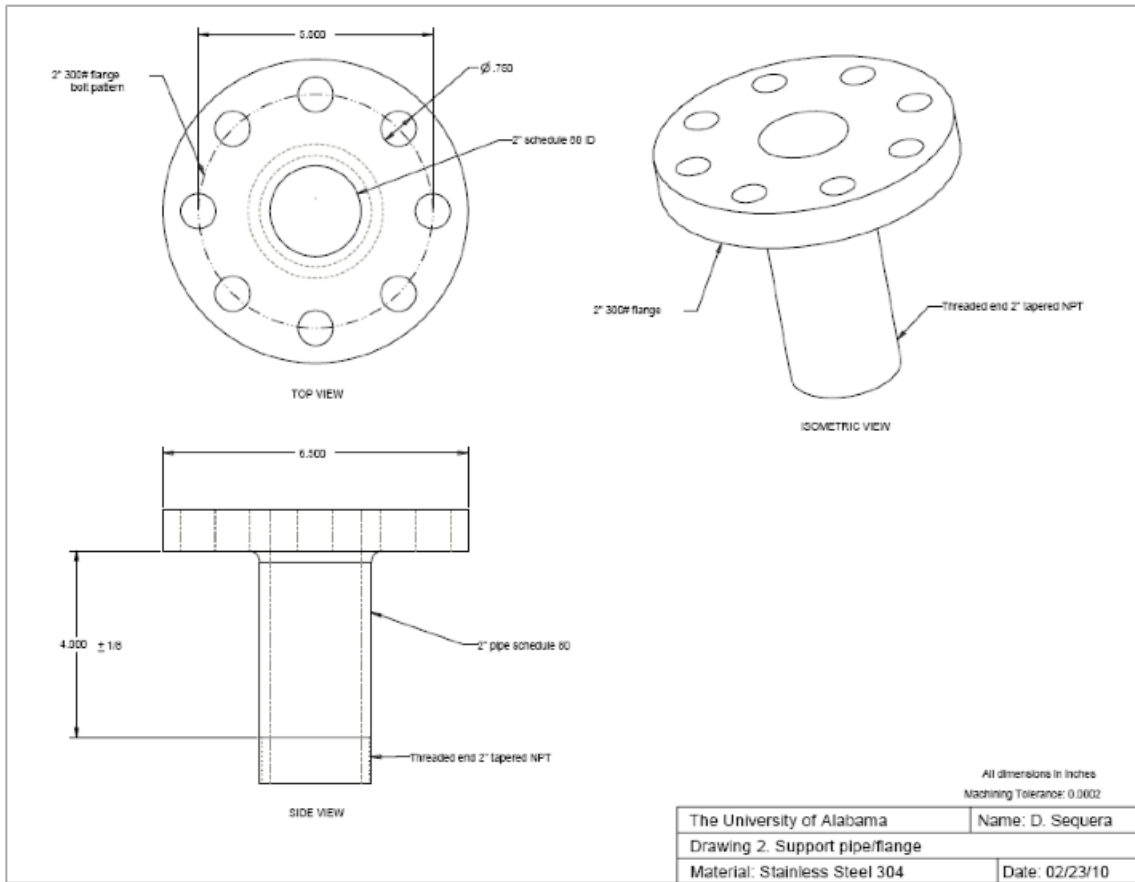


Figure A.11. Details of support pipe and flange

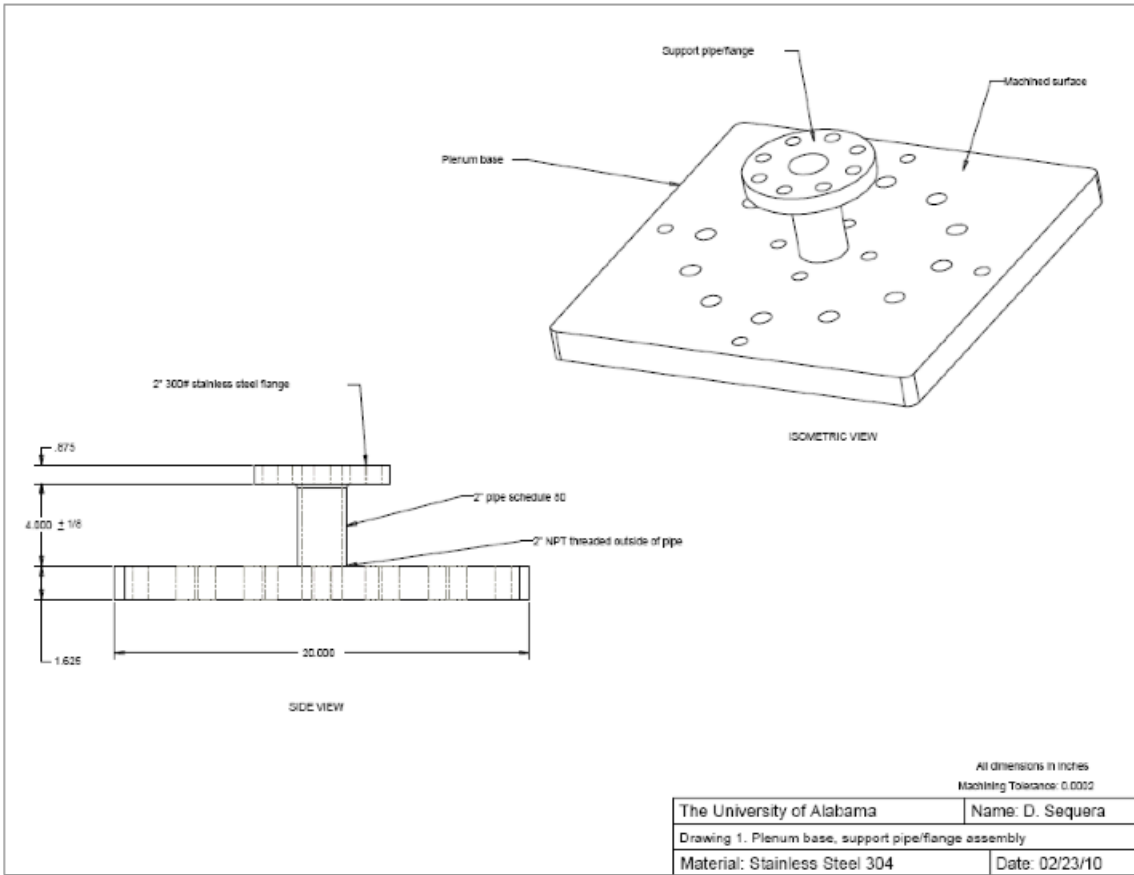


Figure A.12. Details of assembled plenum base

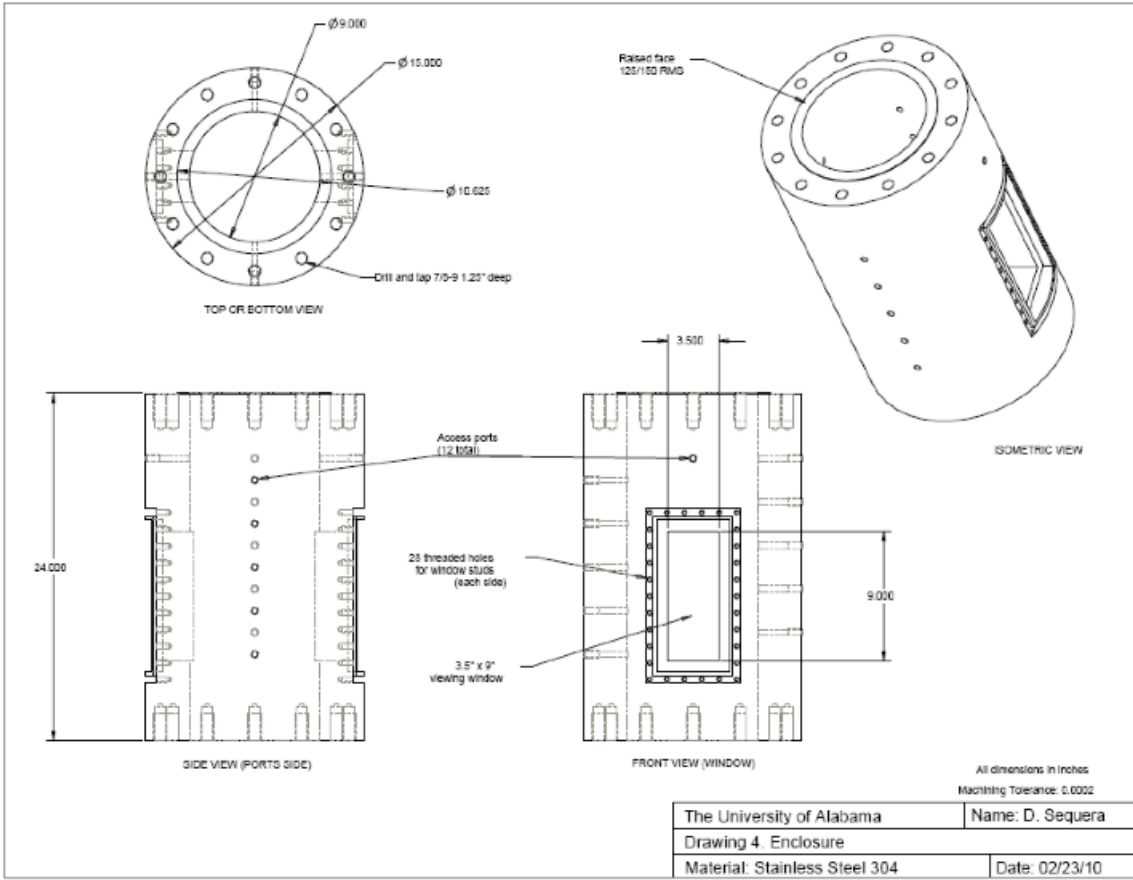


Figure A.13. Details of enclosure

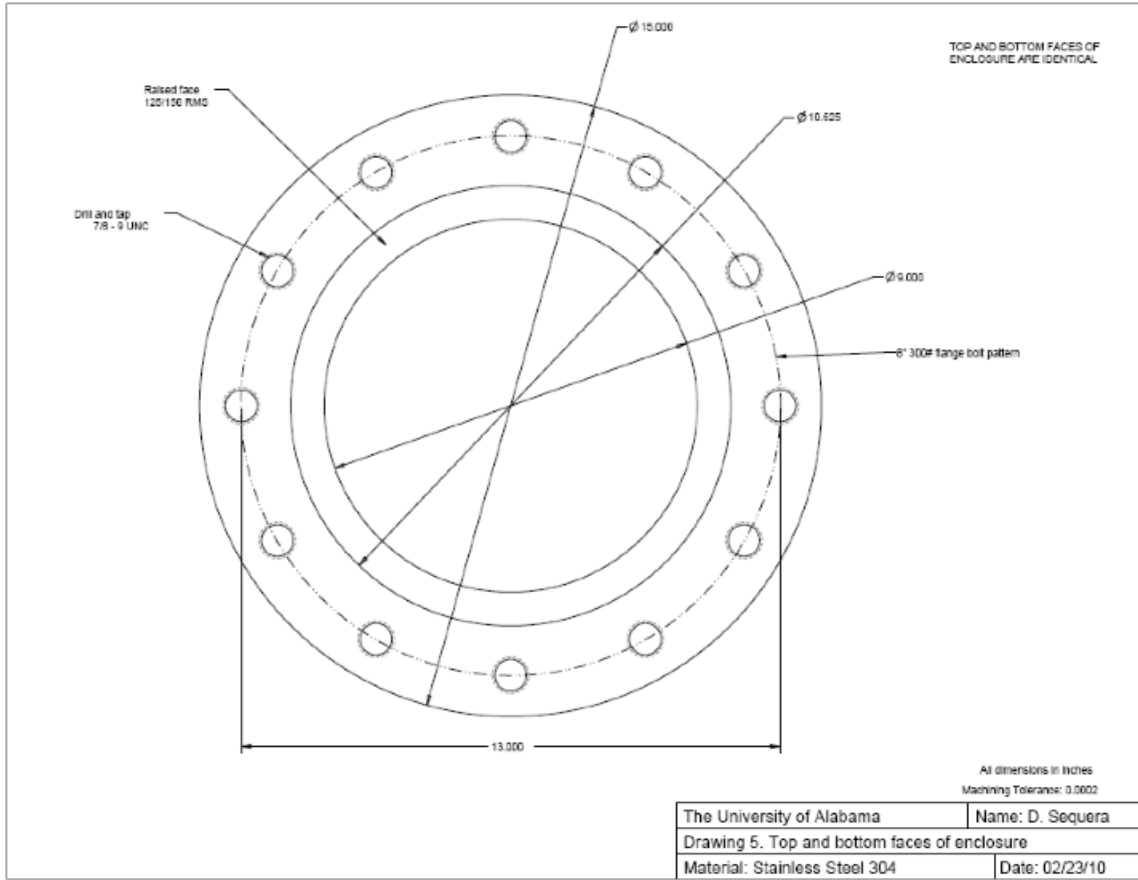


Figure A.14. Detail of enclosure faces

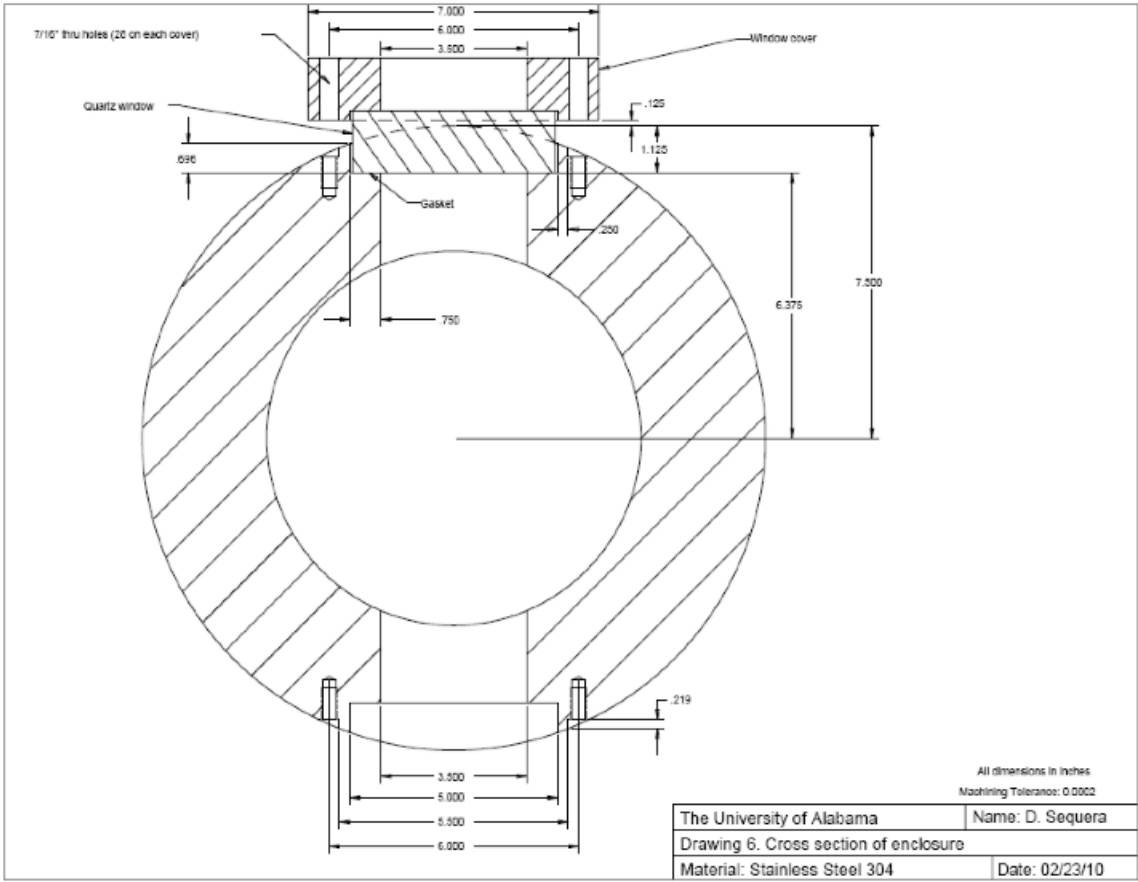


Figure A.15. Details of enclosure cross section

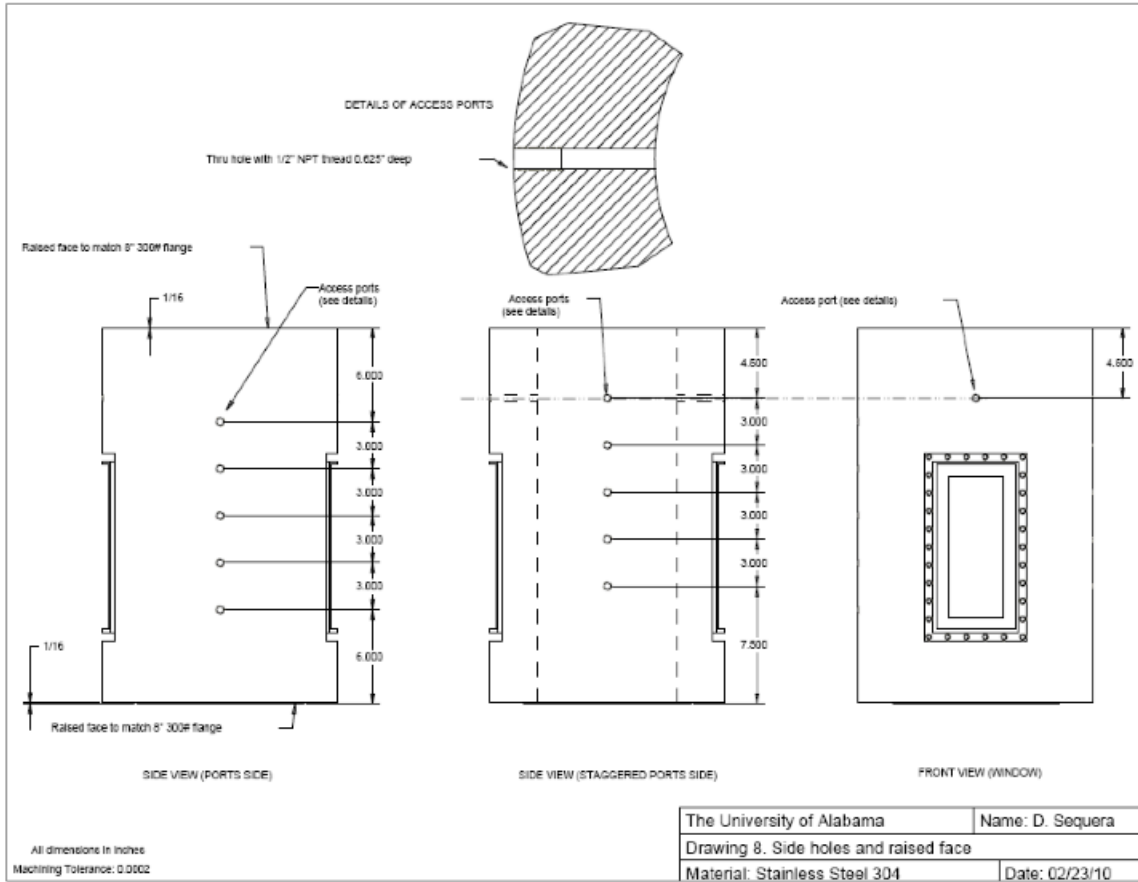


Figure A.16. Details of enclosure access ports

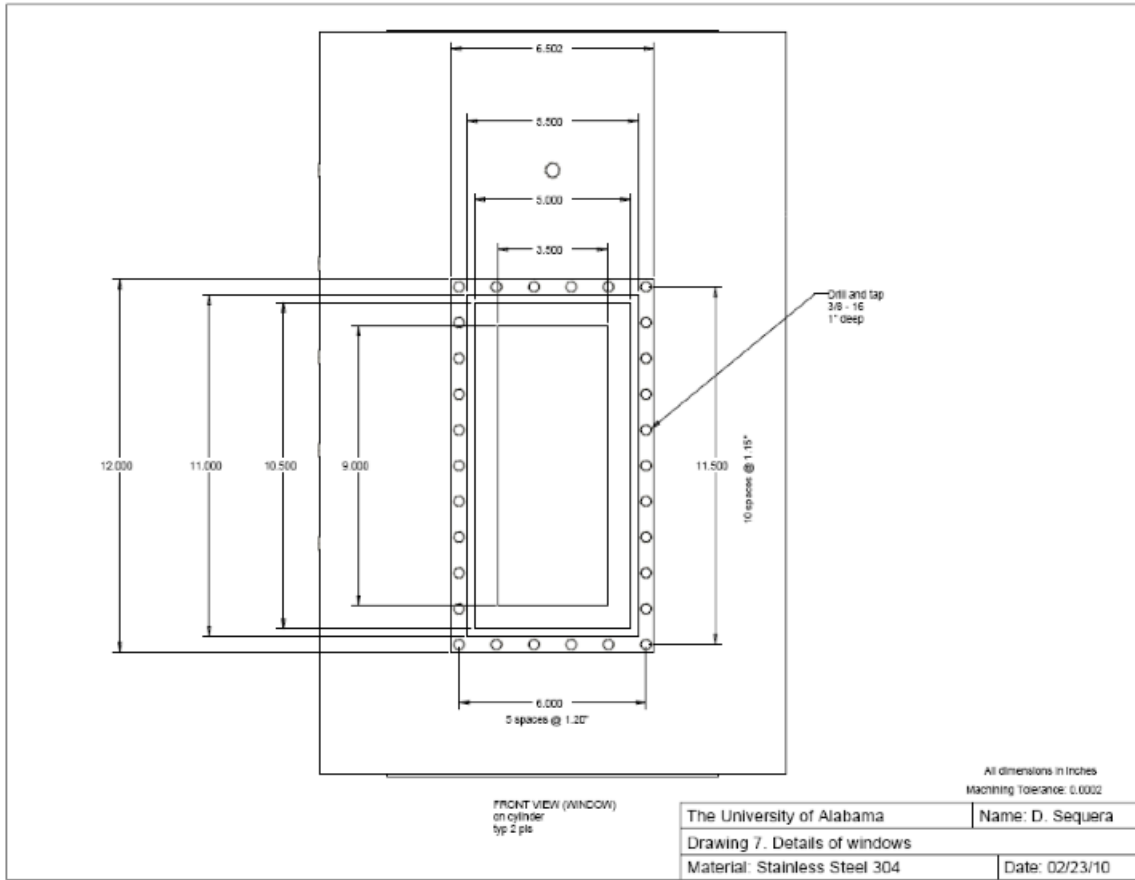


Figure A.17. Details of window ports

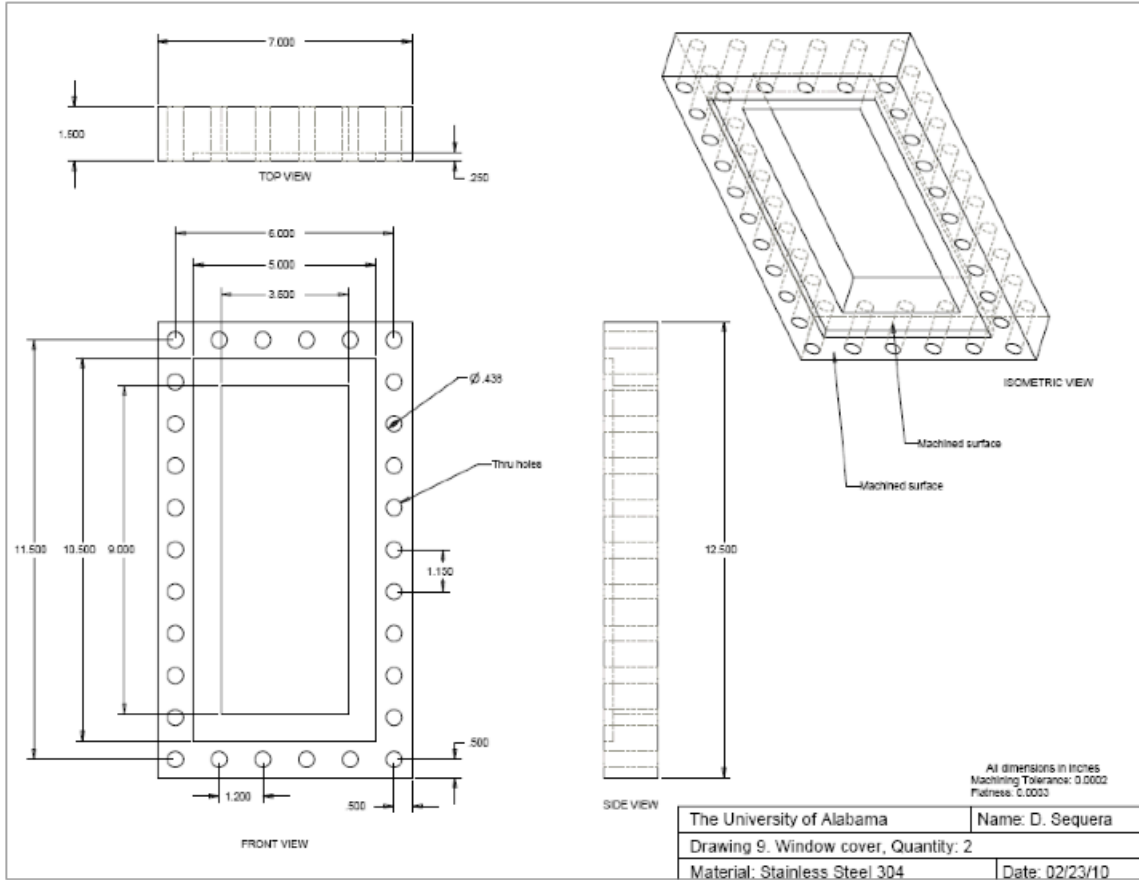


Figure A.18. Details of window frame

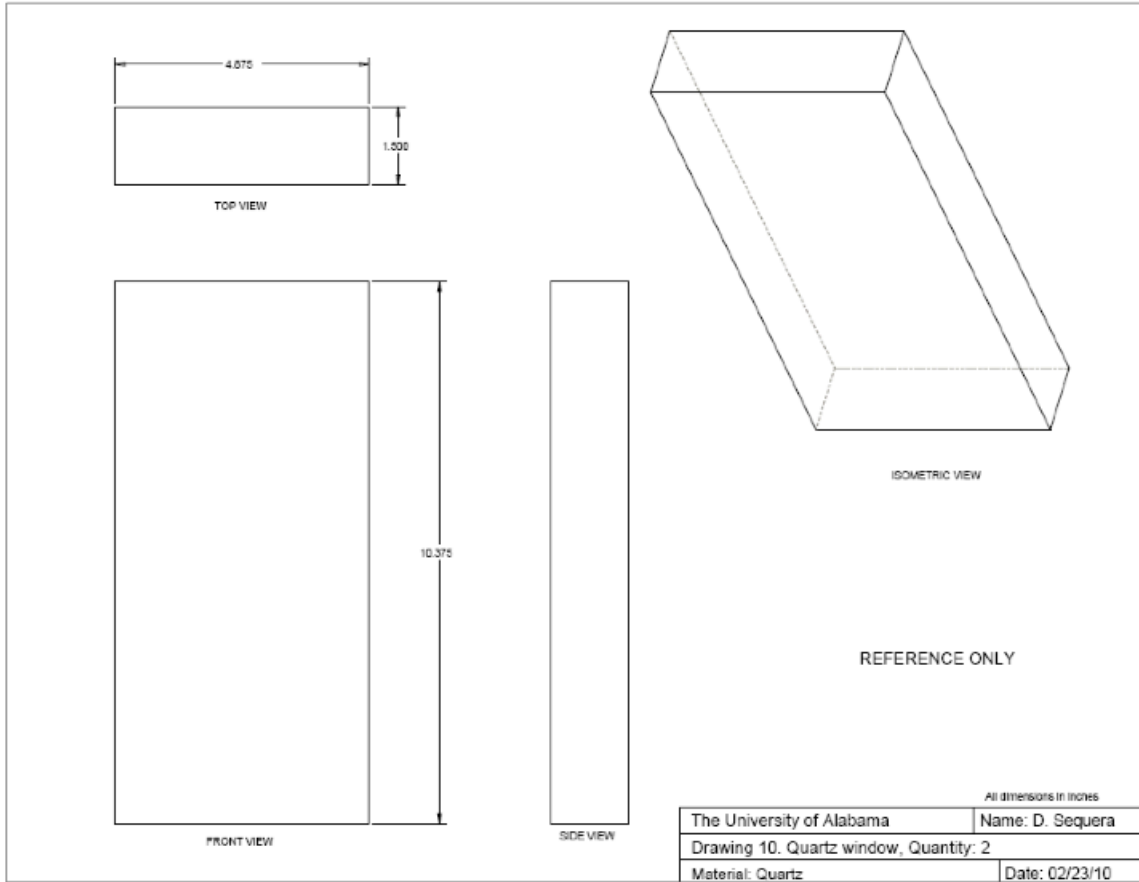


Figure A.19. Details of optical access panel

APPENDIX B

CALCULATION OF SWIRL NUMBER

The flow swirler used in this study is illustrated in Figure B.1.

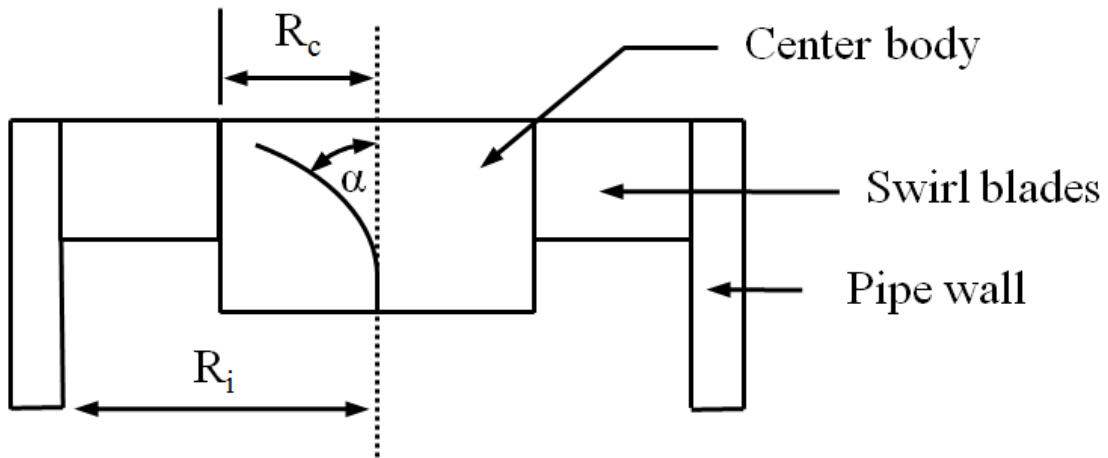


Figure B.1. Schematic of flow swirler

The swirl number, S , is calculated in accordance with Johnson et al. as:

$$S = \frac{2}{3} \tan \alpha \left(\frac{1-R^2}{1-R^2} \right) \quad (\text{B.1})$$

where α is the vane angle with respect to the vertical axis, and R is the effective radius defined by Johnson et al. as:

$$R = \frac{R_c}{R_i} \quad (\text{B.2})$$

where R_c is defined as the center body radius, and R_i is defined as the total swirler radius.

For the swirler used in this study:

- $\alpha = 62^\circ$
- $R_c = 0.7$ cm
- $R_i = 1.2$ cm

which gives:

$$R = 0.58$$

and

$$S = 1.5$$

APPENDIX C

CALCULATION OF REACTANT FLOW RATE AND EQUIVALENCE RATIO

As described in Chapter 2, differential pressure is measured across laminar flow elements (LFEs) in both combustion and cooling airlines, and upstream of each LFE, temperature is measure using a K-type thermocouple. Furthermore, absolute pressure is measured at the LFEs. With these three parameters and LFE manufacturer specifications, the volumetric flow rate upstream of sonic nozzle is calculated as:

$$Q_{CFM} = ((B \times \Delta P) + (C \times \Delta P^2)) \times \frac{\mu_{std}}{\mu_f} \quad (C.1)$$

where Q_{CFM} is the actual volumetric flow rate (CFM), B and C are calibration constants provided by the manufacturer, ΔP is differential pressure (in W.C.), μ_{std} is the viscosity of flow gas at 20 °C (micropoise), and μ_f is the viscosity of flow gas at actual temperature (micropoise). The viscosity of the flow gas is calculated using Sutherland's equation:

$$\mu_f = \frac{bT^{3/2}}{T+S} \quad (C.2)$$

where T is temperature (K), b and S are constants for air:

$$b = 14.58 \frac{\mu P}{K^{1/2}} \quad (C.3)$$

and

$$S = 110.4 \text{ K} \quad (C.4)$$

The volumetric flow rate is converted from CFM to LPM using:

$$Q_{LPM} = Q_{CFM} \times 28.317 \frac{L}{ft^3} \quad (C.5)$$

Actual volumetric flow rates through the apparatus, or those downstream of sonic nozzles, are calculated based on the principle of constant mass flow rates in choked flow, using:

$$\dot{m} = (\rho \times Q)_{upstream} = (\rho \times Q)_{downstream} \quad (C.6)$$

or

$$Q_{downstream} = Q_{upstream} \times \frac{\rho_{upstream}}{\rho_{downstream}} \quad (C.7)$$

where ρ is the density of air at flow temperature.

Equation (C.7) will calculate the downstream volumetric flow rate in units consistent with those of the upstream flow rate, but note, densities must be of consistent units.

Density of air at the flow temperature is calculated by the Ideal Gas Law:

$$\rho = \frac{P_{abs}}{RT} \quad (C.8)$$

where P_{abs} is absolute air pressure (Pa), R is the specific gas constant for air (J/Kg-K), and T is temperature (K).

Equivalence ratio, ϕ , is calculated for methane-air combustion as:

$$\phi = \frac{AF_{st}}{AF} \quad (C.9)$$

where AF_{st} is the mass based stoichiometric air to fuel ratio and AF is the mass based actual air to fuel ratio. For methan-air combustion:

$$AF_{st} = 17.19 \quad (C.10)$$

and

$$AF = \frac{\dot{m}_{air}}{\dot{m}_{CH_4}} = \frac{(\rho \times Q)_{air}}{(\rho \times Q)_{CH_4}} \quad (C.11)$$

APPENDIX D

SOUND PRESSURE LEVEL CALCULATION

As described in Chapter 2, a Matlab script code is used to calculate total SPL for sound measurements in this study. LabVIEW is used to perform an FFT of the scaled microphone voltage, which is subsequently fed into the script code to calculate SPL per frequency, SPL per one-third octave band, and total SPL. All sound pressure level calculations are based on a reference pressure of 20 μPa .

```
%Determine power per one-third octave frequency band
%%%%%%%%%%%%%%%%%%%%%%%%%%%%%%%%%%%%%%%%%%%%%%%%%%%%%%%%%%%%%%%%%%%%%%%%
j=1;
for i=91:113
band1(i)=Prms(i);
end
P(j)=sum(band1);
j=j+1;
%%%%%%%%%%%%%%%%%%%%%%%%%%%%%%%%%%%%%%%%%%%%%%%%%%%%%%%%%%%%%%%%%%%%%%%%
for i=113:141    %generating array
%total power in frequency band and generating SPL array
band2(i)=Prms(i);    %generating array end
P(j)=sum(band2);    %total power in frequency band
j=j+1;
```

```
%%%%%%%%%
```

```
for i=141:178
```

```
band3(i)=Prms(i);    %generating array
```

```
end
```

```
P(j)=sum(band3);    %total power in frequency band and generating SPL array
```

```
j=j+1;
```

```
%%%%%%%%%
```

```
for i=178:226
```

```
band4(i)=Prms(i);    %generating array
```

```
end
```

```
P(j)=sum(band4);    %total power in frequency band and generating SPL array
```

```
j=j+1;
```

```
%%%%%%%%%
```

```
for i=226:281
```

```
band5(i)=Prms(i);    %generating array
```

```
end
```

```
P(j)=sum(band5);    %total power in frequency band and generating SPL array
```

```
j=j+1;
```

```
%%%%%%%%%
```

```
for i=281:356
```

```
band6(i)=Prms(i);
```

```
end
```

```
P(j)=sum(band6);
```

```

%generating array

%total power in frequency band and generating SPL array

j=j+1;

%%%%%%%%

for i=356:451

band7(i)=Prms(i);    %generating array

end

P(j)=sum(band7);    %total power in frequency band and generating SPL array

j=j+1;

%%%%%%%%

for i=451:561

band8(i)=Prms(i);    %generating array

end

P(j)=sum(band8);    %total power in frequency band and generating SPL array

j=j+1;

%%%%%%%%

for i=561:701

band9(i)=Prms(i);    %generating array

end

P(j)=sum(band9);    %total power in frequency band and generating SPL array

j=j+1;

%%%%%%%%

for i=701:901

```

```

band10(i)=Prms(i);
end
P(j)=sum(band10);
j=j+1;
%generating array %total power in frequency band and generating SPL array
%%%%%%%%%%%%
for i=901:1121
band11(i)=Prms(i); %generating array
end
P(j)=sum(band11); %total power in frequency band and generating SPL array
j=j+1;
%%%%%%%%%%%%
for i=1121:1401
band12(i)=Prms(i); %generating array
end
P(j)=sum(band12); %total power in frequency band and generating SPL array
j=j+1;
%%%%%%%%%%%%
for i=1401:1776
band13(i)=Prms(i); %generating array
end
P(j)=sum(band13); %total power in frequency band and generating SPL array
j=j+1;

```

```

%%%%%%%%%%
for i=1776:2251
band14(i)=Prms(i);    %generating array
end
P(j)=sum(band14);    %total power in frequency band and generating SPL array
j=j+1;
%%%%%%%%%%
for i=2251:2801
band15(i)=Prms(i);    %generating array
end
P(j)=sum(band15);    %total power in frequency band and generating SPL array
j=j+1;
%%%%%%%%%%
for i=2801:3551
band16(i)=Prms(i);    %generating array
end
P(j)=sum(band16);    %total power in frequency band and generating SPL array
j=j+1;
%%%%%%%%%%
for i=3551:4501
band17(i)=Prms(i);    %generating array
end
P(j)=sum(band17);    %total power in frequency band and generating SPL array

```

```

j=j+1;
%%%%%%%%%%

for i=4501:5616

band18(i)=Prms(i);    %generating array

end

P(j)=sum(band18);    %total power in frequency band and generating SPL array

j=j+1;
%%%%%%%%%%

for i=5616:7066

band19(i)=Prms(i);    %generating array

end

P(j)=sum(band19);    %total power in frequency band and generating SPL array

j=j+1;
%%%%%%%%%%

for i=7066:8896

band20(i)=Prms(i);    %generating array

end

P(j)=sum(band20);    %total power in frequency band and generating SPL array

%%%%%%%%%%

%CALCULATION OF SOUND PRESSURE LEVEL PER ONE-THIRD OCTAVE
BAND

Freq_band=[20 25 31.5 40 50 63 80 100 125 160 200 250 315 400 500 630 800 1000
1250 1600];    %Centers of frequency bands

```

```

SPL=10*log10(P/(4E-10)); %SPL per 1/3 octave band

%plot(Freq_band,SPL) %CALCULATION OF SOUND PRESSURE LEVEL PER
FREQUENCY

Freq=0:0.2:1999.8; %Frequency range, by frequency resolution

dB_per_freq=10*log10(Prms/4E-10); %SPL at each frequency

%CALCULATION OF TOTAL dB

Rel_power=10.^(SPL./10); %Converting dB to relative power to sum dB levels

Sum_Rel_power=sum(Rel_power);

Total_dB=10*log10(Sum_Rel_power); %CALCULATION OF dBA AND TOTAL dBA

%A-weighting correction factors:

A_factor=[50.50 44.70 39.40 34.60 30.20 26.20 22.50 19.10 16.10 13.40 10.90 8.60 6.60
4.80 3.20 1.90 0.80 0.0 -0.60 -1.00];

SPL_dBA=SPL-A_factor; %Sound pressure level in dBA

Rel_power_dBA=10.^(SPL_dBA./10); %Converting dB to relative power to sum dB
levels

Sum_Rel_power_dBA=sum(Rel_power_dBA);

Total_dBA=10*log10(Sum_Rel_power_dBA);

%%%%%%%%%%JET NOISE%%%%%%%%%%

%Determine power per one-third octave frequency band

%%%%%%%%%%

Jj=1;

for Ji=91:113

```

```

bandJ1(Ji)=PrmsJ(Ji);

%generating array %total power in frequency band and generating SPL array

end

PJ(Jj)=sum(bandJ1);

Jj=Jj+1;

%%%%%%%%%%%%%%

for Ji=113:141

bandJ2(Ji)=PrmsJ(Ji); %generating array

end

PJ(Jj)=sum(bandJ2); %total power in frequency band

Jj=Jj+1;

%%%%%%%%%%%%%%

for Ji=141:178

bandJ3(Ji)=PrmsJ(Ji); %generating array

end

PJ(Jj)=sum(bandJ3); %total power in frequency band and generating SPL array

Jj=Jj+1;

%%%%%%%%%%%%%%

for Ji=178:226

bandJ4(Ji)=PrmsJ(Ji); %generating array

end

PJ(Jj)=sum(bandJ4); %total power in frequency band and generating SPL array

Jj=Jj+1;

```

```

%%%%%%%%%%
for Ji=226:281

bandJ5(Ji)=PrmsJ(Ji); %generating array

end

PJ(Jj)=sum(bandJ5); %total power in frequency band and generating SPL array

Jj=Jj+1;

%%%%%%%%%%

for Ji=281:356

bandJ6(Ji)=PrmsJ(Ji); %generating array

end

PJ(Jj)=sum(bandJ6); %total power in frequency band and generating SPL array

Jj=Jj+1;

%%%%%%%%%%

for Ji=356:451

bandJ7(Ji)=PrmsJ(Ji);

end

PJ(Jj)=sum(bandJ7); %generating array

%total power in frequency band and generating SPL array

Jj=Jj+1;

%%%%%%%%%%

for Ji=451:561

bandJ8(Ji)=PrmsJ(Ji); %generating array

end

```

```

PJ(Jj)=sum(bandJ8); %total power in frequency band and generating SPL array
Jj=Jj+1;
%%%%%%%%%%
for Ji=561:701
bandJ9(Ji)=PrmsJ(Ji); %generating array
end
PJ(Jj)=sum(bandJ9); %total power in frequency band and generating SPL array
Jj=Jj+1;
%%%%%%%%%%
for Ji=701:901
bandJ10(Ji)=PrmsJ(Ji);%generating array
end PJ(Jj)=sum(bandJ10); %total power in frequency band and generating SPL array
Jj=Jj+1;
%%%%%%%%%%
for Ji=901:1121
bandJ11(Ji)=PrmsJ(Ji);
end
PJ(Jj)=sum(bandJ11); Jj=Jj+1; %generating array %total power in frequency band
and generating SPL array
%%%%%%%%%%
for Ji=1121:1401
bandJ12(Ji)=PrmsJ(Ji);%generating array
end

```

```

PJ(Jj)=sum(bandJ12); %total power in frequency band and generating SPL array
Jj=Jj+1;
%%%%%%%%%%
for Ji=1401:1776
bandJ13(Ji)=PrmsJ(Ji);    %generating array
end
PJ(Jj)=sum(bandJ13); %total power in frequency band and generating SPL array
Jj=Jj+1;
%%%%%%%%%%
for Ji=1776:2251
bandJ14(Ji)=PrmsJ(Ji);    %generating array
end
PJ(Jj)=sum(bandJ14); %total power in frequency band and generating SPL array
Jj=Jj+1;
%%%%%%%%%%
for Ji=2251:2801
bandJ15(Ji)=PrmsJ(Ji);    %generating array
end
PJ(Jj)=sum(bandJ15); %total power in frequency band and generating SPL array
Jj=Jj+1;
%%%%%%%%%%
for Ji=2801:3551
bandJ16(Ji)=PrmsJ(Ji);    %generating array

```

```

end

PJ(Jj)=sum(bandJ16); %total power in frequency band and generating SPL array

Jj=Jj+1;

%%%%%%%%%%%%

for Ji=3551:4501

bandJ17(Ji)=PrmsJ(Ji);    %generating array

end

PJ(Jj)=sum(bandJ17); %total power in frequency band and generating SPL array

Jj=Jj+1;

%%%%%%%%%%%%

for Ji=4501:5616

bandJ18(Ji)=PrmsJ(Ji);    %generating array

end PJ(Jj)=sum(bandJ18); %total power in frequency band and generating SPL array

Jj=Jj+1;

%%%%%%%%%%%%

for Ji=5616:7066

bandJ19(Ji)=PrmsJ(Ji);    %generating array

end PJ(Jj)=sum(bandJ19); %total power in frequency band and generating SPL array

Jj=Jj+1;

%%%%%%%%%%%%

for Ji=7066:8896

bandJ20(Ji)=PrmsJ(Ji);    %generating array

end

```

```

PJ(Jj)=sum(bandJ20); %total power in frequency band and generating SPL array
%%%%%%%%%%%%%%%%%%%%%%%%%%%%%%%%%%%%%%%%%%%%%%%%%%%%%%%%%%%%%%%%%%%%%%%%

%CALCULATION OF SOUND PRESSURE LEVEL PER ONE-THIRD OCTAVE
BAND

Freq_band_J=[20 25 31.5 40 50 63 80 100 125 160 200 250 315 400 500 630 800 1000
1250 1600]; %Centers of frequency bands

SPL_J=10*log10(PJ/(4E-10)); %SPL per 1/3 octave band

%plot(Freq_band_J,SPL_J) %CALCULATION OF SOUND PRESSURE LEVEL PER
FREQUENCY

Freq_J=0:0.2:1999.8; %%%%%%%%%%%%%%%%%%%%%%%%%%%%%%%%%%%%%%%%%%%%%%%%%%%%%%%%%%%%%%%%%%%%%%%%%

dB_per_freq_J=10*log10(PrmsJ/4E-10);

%CALCULATION OF TOTAL dB Rel_power_J=10.^(SPL_J./10);

%Frequency range, by frequency resolution %SPL at each frequency

%Converting dB to relative power to sum dB levels

Sum_Rel_power_J=sum(Rel_power_J);

Total_dB_J=10*log10(Sum_Rel_power_J);

%CALCULATION OF dBA AND TOTAL dBA

%A-weighting correction factors:

A_factor_J=[50.50 44.70 39.40 34.60 30.20 26.20 22.50 19.10 16.10 13.40 10.90 8.60
6.60 4.80 3.20 1.90 0.80 0.00 -0.60 -1.00];

SPL_dBA_J=SPL_J-A_factor_J; %Sound pressure level in dBA

Rel_power_dBA_J=10.^(SPL_dBA_J./10); dB levels

```

$\text{Sum_Rel_power_dBA_J} = \text{sum}(\text{Rel_power_dBA_J});$

$\text{Total_dBA_J} = 10 * \log_{10}(\text{Sum_Rel_power_dBA_J})$

APPENDIX E

UNCERTAINTY ANALYSIS

A procedure outlined by Coleman and Steel (1999) is used to perform uncertainty analysis for measurements made in this study. Random and Systematic errors are computed for each measured value; both of these errors are then combined to calculate the total uncertainty in the measured value.

The overall uncertainty of the measurement, U_r , is calculated as the square root of the sum of the squares, including systematic and random uncertainties:

$$\mu_r = \sqrt{B_r^2 + P_r^2} \quad (\text{E.1})$$

where P_r is the random uncertainty and B_r is the systematic uncertainty. Each quantity is expressed respectively as:

$$B_r^2 = \sum \left(\frac{\partial r}{\partial X_i} \right)^2 B_{X_i}^2 \quad (\text{E.2})$$

and

$$P_r^2 = \sum \left(\frac{\partial r}{\partial X_i} \right)^2 P_{X_i}^2 \quad (\text{E.3})$$

Systematic uncertainties are provided for each instrument by its manufacturer. Random uncertainties are calculated using a random sample of measured values for variable X_i and are calculated using the equation:

$$P_{x_i} = \frac{tS_x}{\sqrt{N}} \quad (\text{E.4})$$

where t is a tabulated distribution for 95% confidence with $N-1$ degrees of freedom, S_x is the standard deviation of the sample set, and N is the number of samples in the set. The standard deviation is defined as:

$$S_x = \left[\frac{1}{N-1} \sum (X_i - \bar{X})^2 \right]^{1/2} \quad (\text{E.5})$$

where the mean of the sample set is calculated by:

$$\bar{X} = \frac{1}{N} \sum X_i \quad (\text{E.6})$$

Experimental uncertainty is calculated for air flow rates calculated by LFE measurements, fuel flow measured by mass flow controller, and resulting equivalence ratio. Sample calculations are presented for an air flow rate of 400 LPM, a fuel flow rate of ? LPM, and equivalence ratio of 0.75. The bias error for the LFE is specified as 0.72% of measured value, and bias error for the fuel mass flow controller is given as 0.5% of measured value plus 0.1% full scale. Thus, for air flow, $B_A = 2.9$ LPM and for fuel flow, $B_F = ?$. For example, six random samples are taken for each measured variable as shown in Table E.1. With five degrees of freedom and 95% confidence, $t = 2.571$. Equation E.4 is used to calculate random uncertainties of $P_A = 4.9$ LPM and $P_F = 0.4$ LPM. Substituting into Equation E.1 gives $\mu_A = \pm$ and $\mu_F = \pm$. Resulting uncertainties of air and fuel flow rate are used to obtain the overall uncertainties in equivalence ratio.

Table E-1

Random sample measurements of air and fuel flow rates

| N | Air Flow (LPM) | Fuel Flow (LPM) |
|-------------------|----------------|-----------------|
| 1 | 398.5 | 29.5 |
| 2 | 400.8 | 29.7 |
| 3 | 410.2 | 30.4 |
| 4 | 399.4 | 29.6 |
| 5 | 397.3 | 29.4 |
| 6 | 401.6 | 29.7 |
| Mean | 401.3 | 29.7 |
| Stadard Deviation | 4.6 | 0.3 |

For methan-air combustion:

$$\phi = 9.52 \left(\frac{F}{A} \right) \quad (\text{E.7})$$

The uncertainty in the equivalence ratio is obtained from Equations E.1, E.2, and E.3:

$$\mu_{\phi}^2 = \left(\frac{\partial \phi}{\partial A} \right)^2 \mu_A^2 + \left(\frac{\partial \phi}{\partial F} \right)^2 \mu_F^2 \quad (\text{E.8})$$

where

$$\frac{\partial \phi}{\partial A} = -\frac{9.52}{A^2} = 2.64 \times 10^{-5} \quad (\text{E.9})$$

and

$$\frac{\partial \phi}{\partial F} = \frac{9.52}{A} = 1.59 \times 10^{-2} \quad (\text{E.10})$$

Finally, the total uncertainty in equivalence ratio is $\mu_{\phi} = \pm 0.01$.

APPENDIX F

PLOTS OF JET NOISE

Jet noise results are displayed below for experiments conducted with the steel combustor at high pressures.

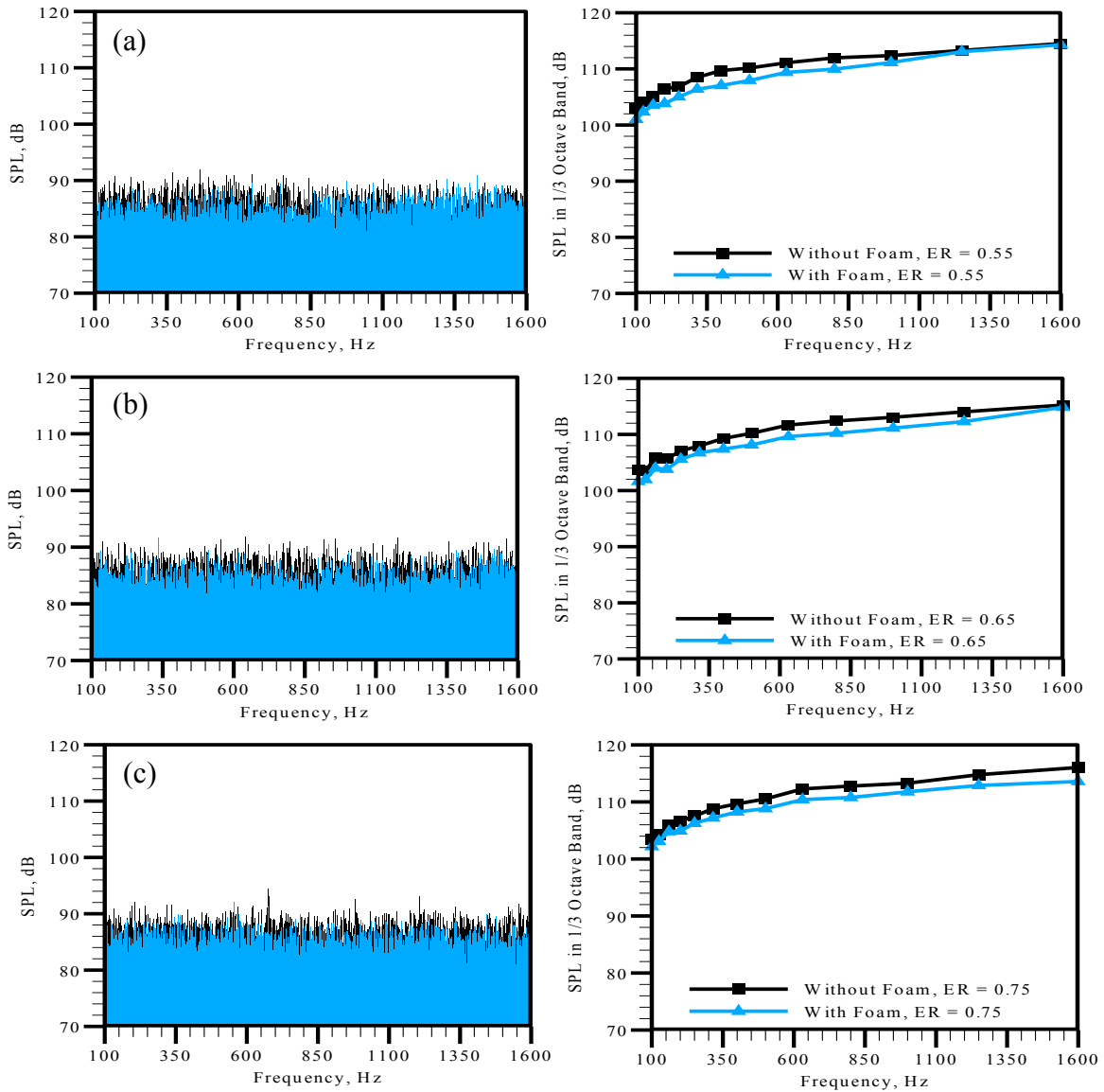


Figure F.1. Acoustic power spectra and SPL in 1/3rd octave band for $P = 0.405$ MPa, $Q = 400$ LPM, (a) $\phi = 0.55$ (case P2-55), (b) $\phi = 0.65$ (case P2-65), and (c) $\phi = 0.75$ (case P2-75)

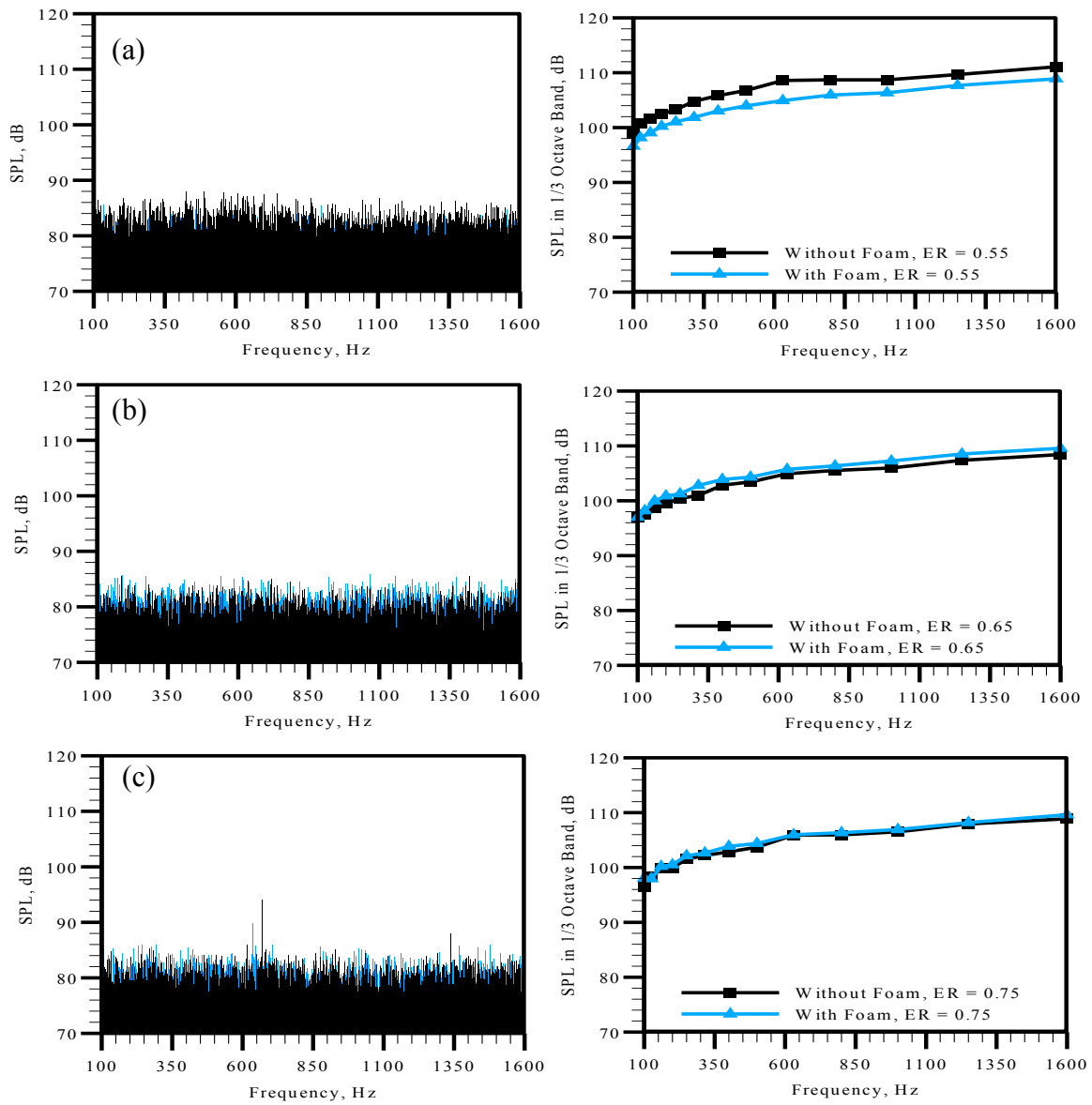


Figure F.2. Acoustic power spectra and SPL in 1/3rd octave band for $P = 0.304$ MPa, $Q = 400$ LPM, (a) $\phi = 0.55$ (case P2-55), (b) $\phi = 0.65$ (case P2-65), and (c) $\phi = 0.75$ (case P2-75)

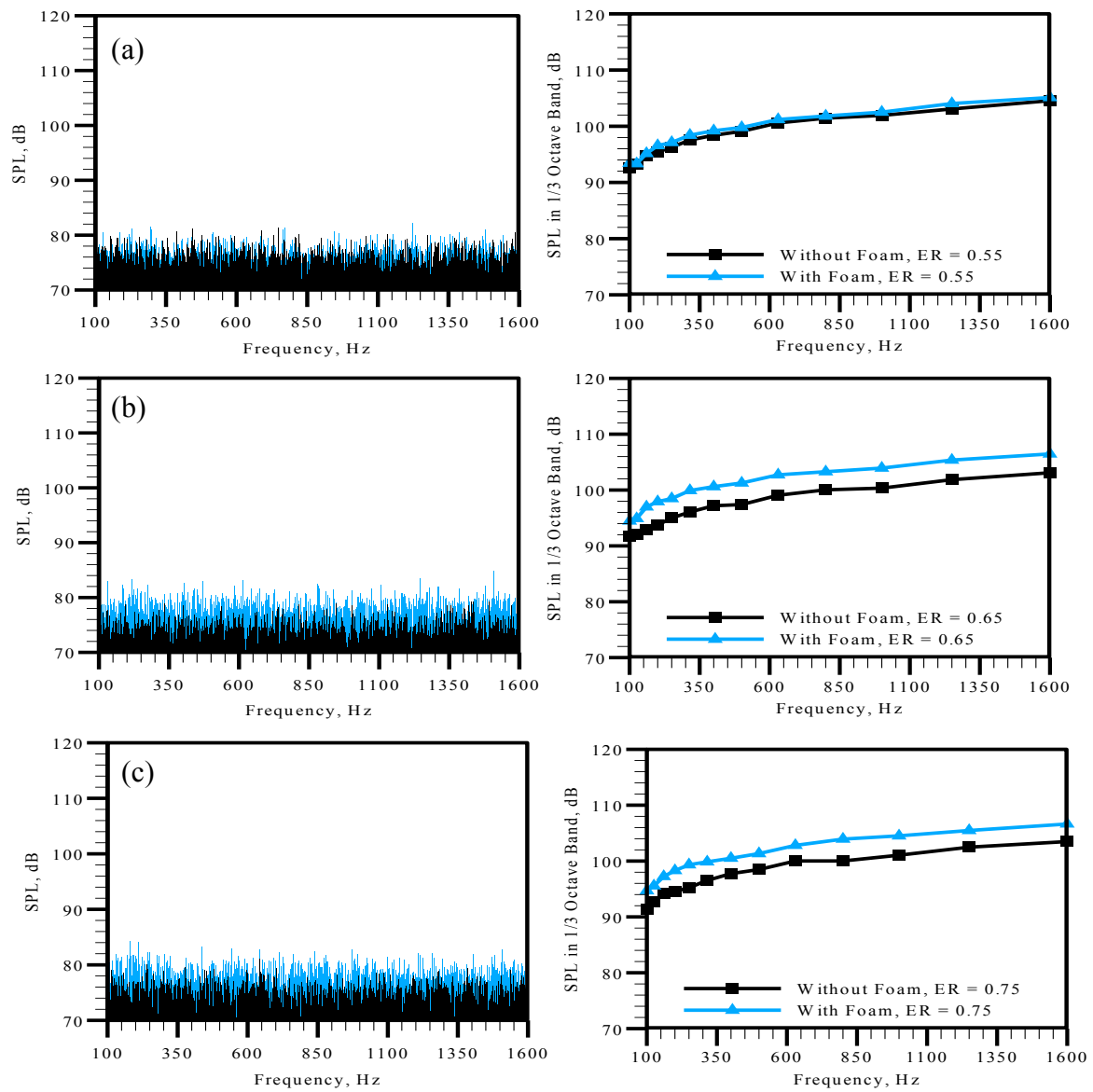


Figure F.3. Acoustic power spectra and SPL in 1/3rd octave band for $P = 0.203$ MPa, $Q = 400$ LPM, (a) $\phi = 0.55$ (case P2-55), (b) $\phi = 0.65$ (case P2-65), and (c) $\phi = 0.75$ (case P2-75)

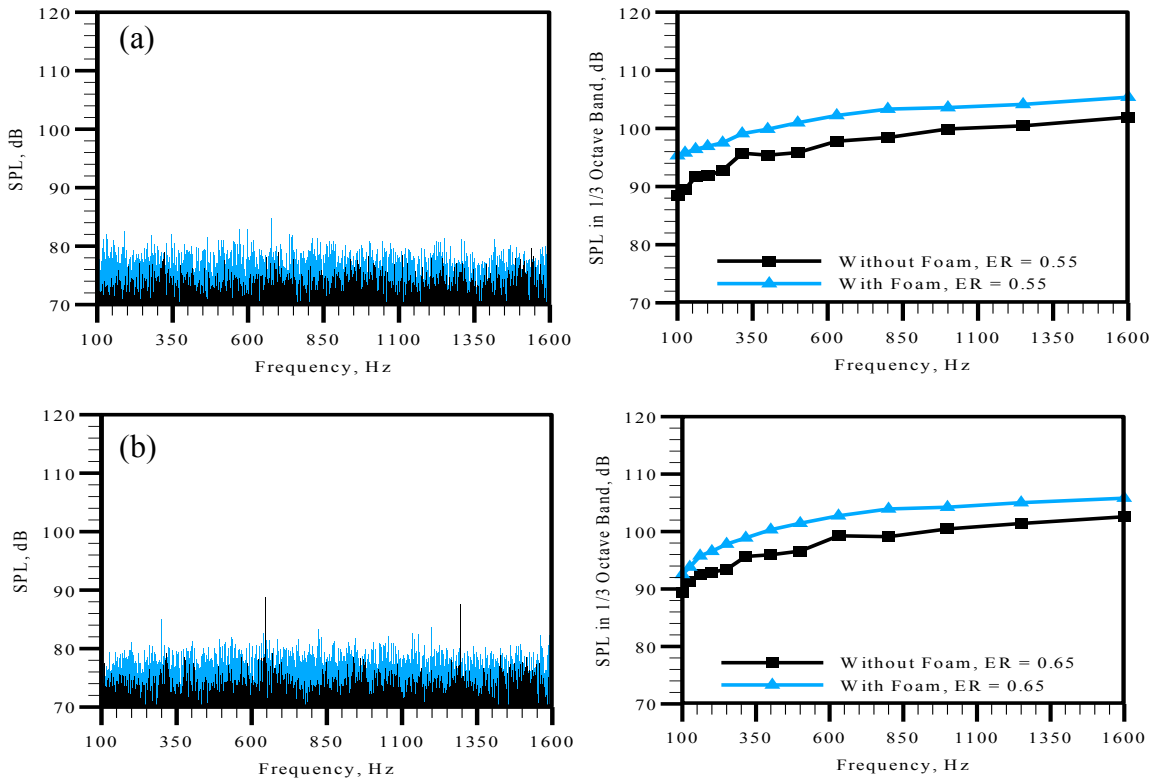


Figure F.4. Acoustic power spectra and SPL in 1/3rd octave band for P = 0.304 MPa, Q = 300 LPM, (a) $\phi = 0.65$ (case P2-65) and (b) $\phi = 0.75$ (case P2-75)

Jet noise results are displayed below for experiments conducted with the custom designed quartz combustor at high pressures. Both full and 1/3 octave band SPL are shown.

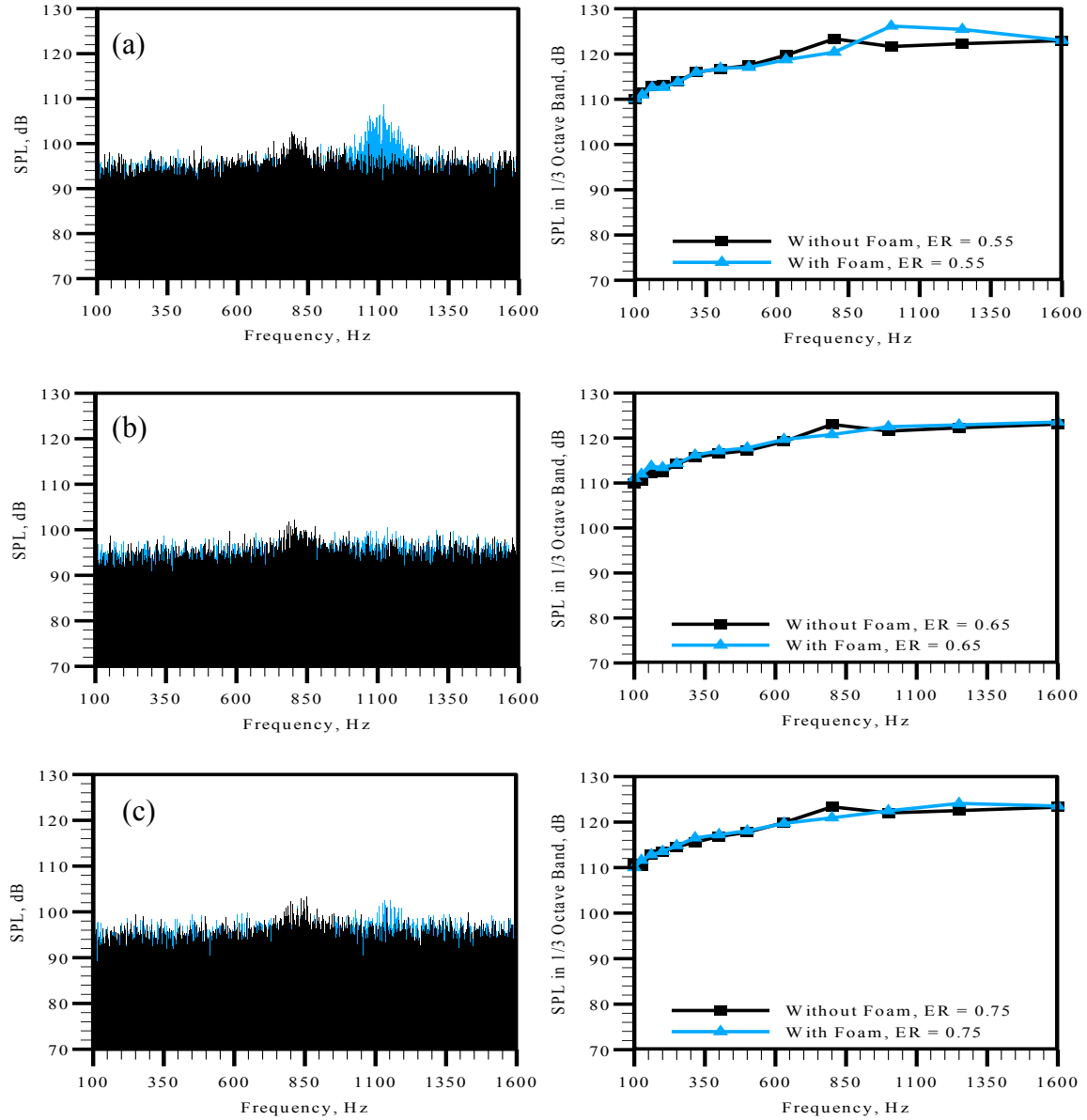


Figure F.5. Acoustic power spectra and SPL in 1/3rd octave band for $P = 0.405$ MPa, $Q = 400$ LPM, (a) $\phi = 0.55$ (case P2-55), (b) $\phi = 0.65$ (case P2-65), and (c) $\phi = 0.75$ (case P2-75)

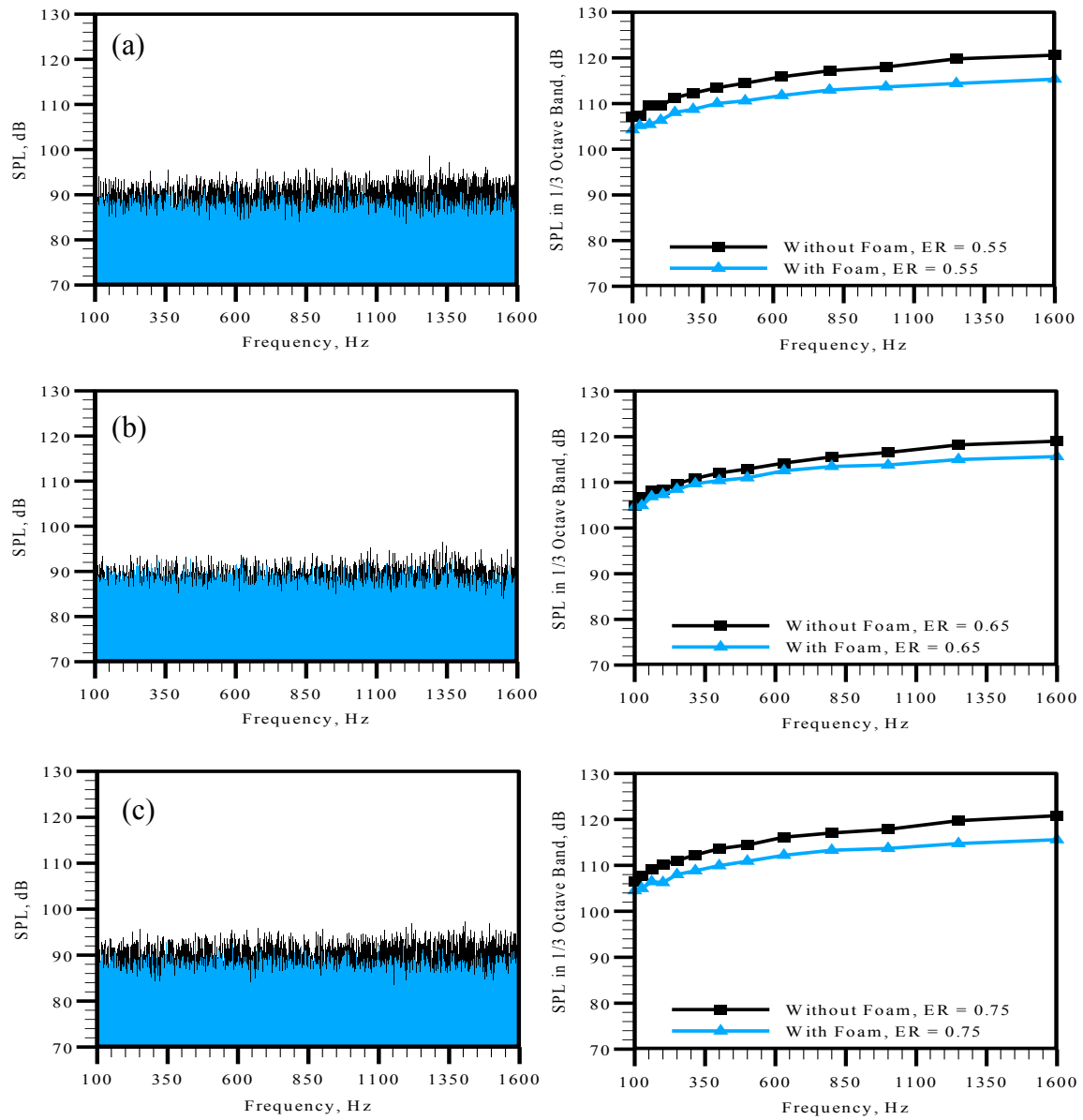


Figure F.6. Acoustic power spectra and SPL in 1/3rd octave band for $P = 0.304$ MPa, $Q = 400$ LPM, (a) $\phi = 0.55$ (case P2-55), (b) $\phi = 0.65$ (case P2-65), and (c) $\phi = 0.75$ (case P2-75)

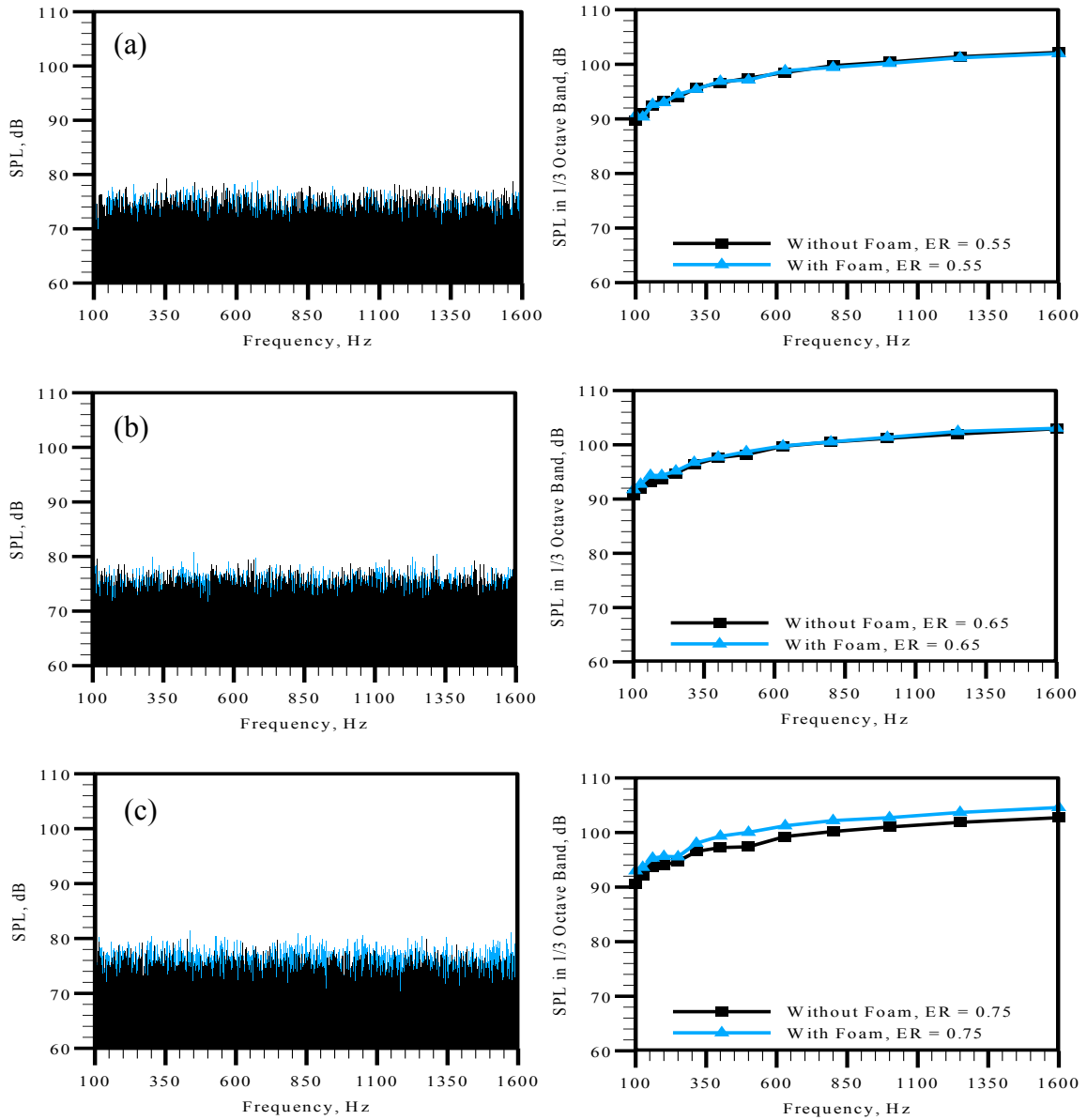


Figure F.7. Acoustic power spectra and SPL in 1/3rd octave band for $P = 0.203$ MPa, $Q = 400$ LPM, (a) $\phi = 0.55$ (case P2-55), (b) $\phi = 0.65$ (case P2-65), and (c) $\phi = 0.75$ (case P2-75)

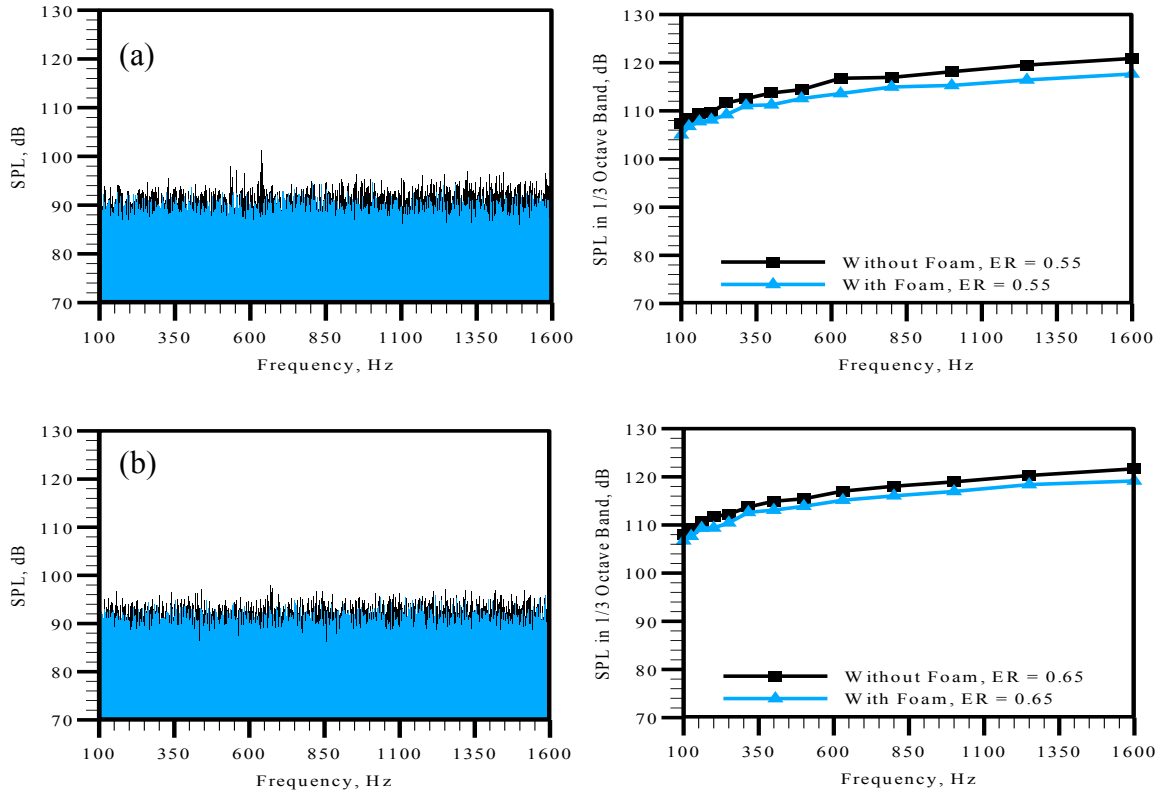


Figure F.8. Acoustic power spectra and SPL in 1/3rd octave band for P = 0.302 MPa, Q = 600 LPM, (a) $\phi = 0.65$ (case P2-65) and (b) $\phi = 0.75$ (case P2-75)

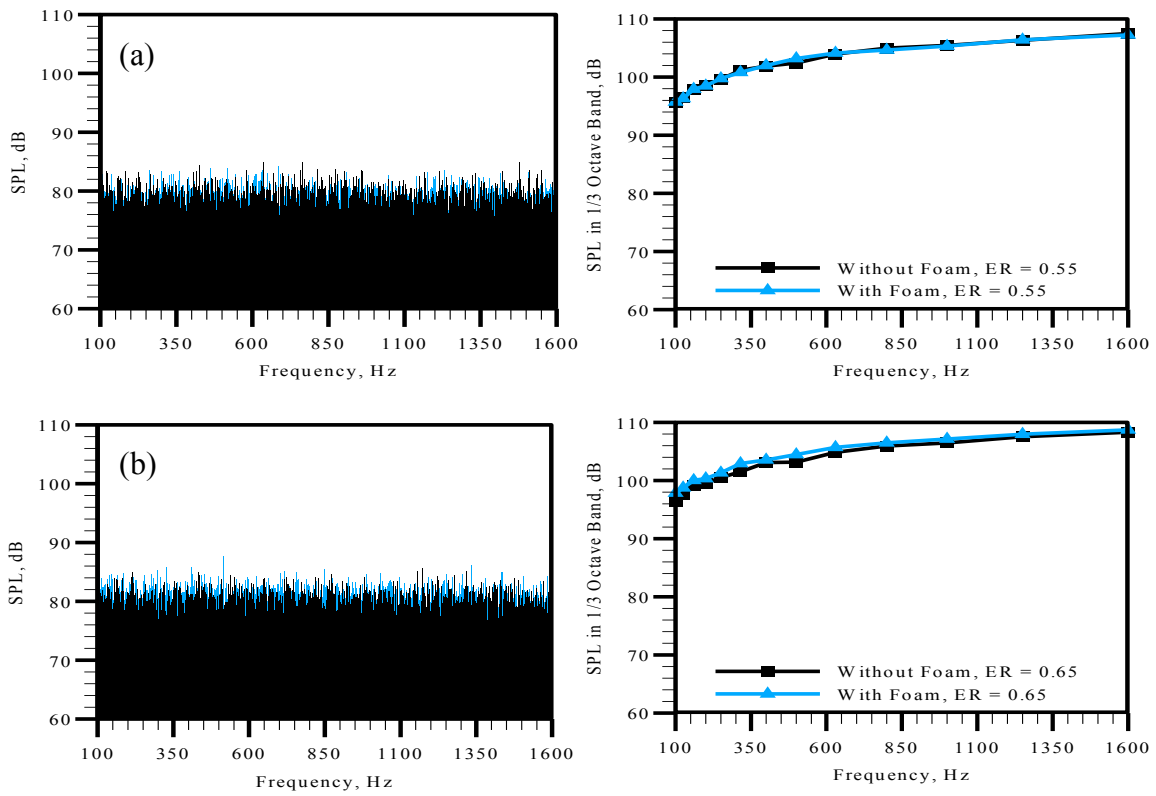


Figure F.9. Acoustic power spectra and SPL in 1/3rd octave band for P = 0.203 MPa, Q = 600 LPM, (a) $\phi = 0.65$ (case P2-65) and (b) $\phi = 0.75$ (case P2-75)